HIGH RESOLUTION SHALLOW SEISMIC SUBSURFACE CHARACTERIZATION

A DISSERTATION

SUBMITTED TO THE DEPARTMENT OF GEOPHYSICS

AND THE COMMITTEE OF GRADUATE STUDIES

OF STANFORD UNIVERSITY

IN PARTIAL FULFILLMENT OF THE REQUIREMENTS

FOR THE DEGREE OF

DOCTOR OF PHILOSOPHY

Ran Bachrach

September 1998.

I certify that I have read this dissertation and that in my opinion it is fully adequate, in scope and quality, as a dissertation for the degree of Doctor of Philosophy.

_____
Amos M. Nur (Principle Advisor)

I certify that I have read this dissertation and that in my opinion it is fully adequate, in scope and quality, as a dissertation for the degree of Doctor of Philosophy.

_____
Gary Mavko (Geophysics)

I certify that I have read this dissertation and that in my opinion it is fully adequate, in scope and quality, as a dissertation for the degree of Doctor of Philosophy.

_____
Keith Loague (Geological and Environmental Science)

I certify that I have read this dissertation and that in my opinion it is fully adequate, in scope and quality, as a dissertation for the degree of Doctor of Philosophy.

_____
Peter K Kitanidis (Civil Engineering)

I certify that I have read this dissertation and that in my opinion it is fully adequate, in scope and quality, as a dissertation for the degree of Doctor of Philosophy.

_____
Jack Dvorkin (Geophysics)

Approved For the University Committee on Graduate Studies

_____

ABSTRACT

Geophysical imaging and characterization methods of the shallow subsurface are underutilized. In many cases this underutilization stems from the difficulty in relating the geophysical image to the environmental problem. To that end, the objective of this research is to integrate surface geophysical imaging techniques to resolve the "characterization" problem, that is, to allow the derivation of the properties of interest (e.g. transport properties, fluid distribution in the near surface, shear strength etc..), from the seismic/electromagnetic measurement. This research mainly focuses on two aspects of this important problem: fluid imaging (i.e. water table, fluid flow, saturation and their spatial distribution), and mechanical properties of near-surface unconsolidated sediment as related to data acquisition. The usage of simple rock physics concepts and theoretical models and their validitaion in high resolution controlled field-scale seismic experiments is presented here. The understanding of the physical properties of near-surface materials is shown to provide important information for acquisition parameterization.

This thesis is made of six chapters. Chapter 2 focuses on the effects of pore fluid on the seismic wave velocities. I study the poroelastic behavior of partially saturated sediments under stress oscillations at different frequencies. I develop a methodology to integrate the acoustic response due to squirt (local) flow in the pore scale with macroscopic flow Biot equations. Chapter 3 describes an experiment which investigates the seismic response of natural systems where fluid flow occurs. This chapter reviews the field results and the basic theory used to model them. The high-resolution experiment provides a valuable link between laboratory data and field scale data. The results demonstrate the effects of fluid substitution insitu as inferred from surface seismics.

Chapter 4 describes the results from the P wave velocity analysis of the data collected in our beach experiments. Chapter 5 is direct continuation of Chapter 4, and present the results from the 3-component seismic experiment which analyze the shear wave and the compressional wave velocity profile in the sand. In chapter 6 I show how rock physics can provide a framework for ultra-shallow seismic data acquisition and that in unconsolidated sediments one can acquire ultra-shallow reflections profiles. In chapter 7 I show that we can obtain water table image with a depth accuracy of centimeters, with seismics and GPR. I also show how high resolution continuos water-table image can be inverted into hydraulic conductivity.

ACKNOWLEDGMENTS

There are many people to whom I wish to thank and who helped me, taught me and encouraged me along the way.

I will start with thanking my advisor, Amos Nur, who brought me into SRB four and a half years ago, and who supported me and directed me ever since. I had a lot of freedom in my work, but whenever I had a problem, Amos was the one to turn to and get a bright and clear advise. Amos was the best advisor I could ever hope for and I thank him for his patience with me. I also thank Dr. Anat Yalin Dror who introduced me to Amos.

I feel privileged to have worked and interact with all of my dissertation reading committee. I thank Gary Mavko for valuable discussions on seismograms and seismic data analysis, Jack Dvorkin for teaching me the clear, bright, and simple ways of mechanics. I thank Peter Kitanidis who tought me how to deal with heterogeneity, and to Keith Loague who tought me that soil and water are more than just mud.

Non of this work (and especially the field work) would have been made possible without Margaret Muir, who made sure that I would have everything I need. I Thank Margaret not only for the support I had but also for the "lessons" I was given in correct administration (which I value as any fundamental physics course), for her patience with me, and for all the help I needed. Thanks Margaret for everything!. I also want to thank all the people that came to work with me in the field, and which were many. Special thanks for the specific experiments and individuals are in the acknowledgements of each chapter. However, once again, thank you all!

My stay here at Stanford was made enjoyable by many people from the department and SRB group. I must acknowledge my office mate, Per Avseth, who beside teaching me (almost) all the geology I know, was a very good friend. I thank Yizhaq Makovsky for the fun we had and for teaching me Promax, and Tapan Mukerji for the valuable discussions on any problem in contemporary Geophysics. I also thank the Department of Geophysics's administrator Linda Farwell and all the staff, as well as all the Geophysics faculty I have interacted with.

I have also interacted with many people during my years here at Stanford. I could not count all of them but I would like to acknowledge the interaction I had with Prof. Don Steeples of the University of Kansas, who's research on shallow seismic provided the base for my field data acquisition and Prof. Rosemary Knight of UBC. I wish also to acknowledge the Dept. of Geophysics of Tel-Aviv University, where I

did my undergraduate work for providing me with an excellent background and love for geophysics.

It is difficult to express my gratitude to my parents, Gad and Hedva Bachrach, for their support and encouragement, and for their trust in me. I was fortunate to grow up in my family and I am grateful for the opportunities they provided me.

Finally, I wish to thank my wife Hagit, for her love and the happiness she brought to me, as well as for her assistance in the field and the office. When no one would come to the field with me, I could always count on Hagit, who probably knows by now quite a lot of geophysics. My life here at Stanford would not have been so full without you Hagit, and I guess the rest of it I'll say in Hebrew.

CONTENTS

LIST OF TABLES

LIST OF FIGURES

CHAPTER 1

INTRODUCTION

1.1   MOTIVATION AND RESEARCH OBJECTIVES

Geophysical imaging and characterization methods in the shallow subsurface are underutilized.   However, the need for cost-effective and accurate shallow imaging/characterization techniques is greater then ever, because of our increasing dependence on resources in the shallow subsurface.

In many cases this underutilization stems from the difficulty in relating the geophysical image to the environmental problem. To that end, the objective of my research was to integrate surface geophysical imaging techniques to resolve the "characterization" problem, that is, to allow the derivation of the properties of interest (e.g. transport properties, fluid distribution in the near surface, shear strength etc..), from the seismic/electromagnetic measurement. The research mainly focused on two aspects of this important problem: fluid imaging (i.e. water table, fluid flow, saturation and distribution), and mechanical properties of near-surface unconsolidated sediment as related to data acquisition.

The first problem—fluid imaging and the affect of fluids on the physical properties of the medium, is an old problem in rock-physics. Many experimental and theoretical studies have been conducted in order to relate the effect of fluid to seismic and electromagnetic velocities (e.g. Biot, 1962, Nur and Seimmons, 1969, Murphy, 1982). However, most of the studies were conducted in the laboratory on samples only a few inches in size; there are practically no field-scale examples of the geophysical signature of fluids from surface seismic. Furthermore, the use of the geophysical information is subject to the accuracy and resolution of the measurements. Hence, to extract the fluid effect on the measurement in real field situations, one must address the fluid imaging problem in the context of noise sources in the experiment.

My approach was to use *in situ* surface measurements, in controlled environments under realistic conditions and constraints, and to try to acquire data that will show the fluid effect in an undisturbed system. Therefore, the results and conclusions of my study will be directly applicable to field data in more complex environments. To do

that, I had to develop techniques for obtaining higher resolution and better quality data, as well as to verify every result. This constraint led me to the second part of my research, the investigation of mechanical properties of the very near subsurface and their effect on seismic data acquisition.

Traditionally, exploration seismology has treated the very near surface velocity as a noise factor, which distorts deep images because of the high heterogeneity of the near surface velocity profile. However, high-resolution, shallow seismic methods target these heterogeneous environments and require an understanding of the relation between the mechanical properties of the subsurface and the pressure and mineralogy.

I address in this dissertation the mechanical properties of unconsolidated sediments, which are commonly encountered in very shallow subsurface. The results of the mechanical modeling are applied to field data acquisition and survey design.

1.2   CHAPTER DESCRIPTIONS

This volume is a sequence of six self contained papers, each formulated to solve a specific problem which is part of the research problem[1].

Chapter 2 focuses on the effects of pore fluid on the seismic wave velocities. I study the poroelastic behavior of partially saturated sediments under stress oscillations at different frequencies. Since fluids are part of the earth's crust and are often the target of the geophysical investigation, modeling the interaction between seismic waves and fluids is fundamental for applying geophysical techniques to subsurface characterization.

The wave-induced dynamics of the fluid-solid interaction in rock at full saturation has been modeled based on two physical mechanisms: Biot's mechanism (e.g., Biot, 1956 and 1962), and the squirt-flow mechanism (e.g., Mavko and Nur, 1979; Dvorkin et al., 1993). In the former model, pore fluid is coupled to the solid frame by viscous friction and inertial coupling. The latter model accounts for the fluid's squirting from thin compliant cracks, deformed by a passing wave, into larger pores. Both models predict that the velocities increase with increasing frequency (an effect called velocity-frequency dispersion).

---

[1] Since parts of each chapter have been or are to be submitted to certain journals, there are few basic relations, which are being repeated. This repetition is done to preserve the self-containment of each chapter.

At partial saturation, the fluid-rock interaction becomes more complex. It depends not only on the properties of the solid, liquid, and gas phases, but also on the arrangement of the fluid in the pore space.

In this chapter, I propose a physical model which integrates the Biot and the squirt-flow mechanism in partially saturated sediments. I do so by calculating the pore pressure distribution at the patch scale as predicted by Biot's theory, and then calculating the averaged squirt response of the medium. The model shows the affect of the viscosity, permeability and the patch size on the seismic wave velocity and can be used for constraining the affect of viscous contaminant on the seismic wave. This work was done in collaboration with Jack Dvorkin.

Chapter 3 describes an experiment which investigates the seismic response of natural systems where fluid flow occurs. To better understand the relation between the hydrological water table and its seismic image, and the seismic response of the subsurface under different wetting and draining situations, I conducted a high-resolution shallow seismic survey on Moss Landing, a sandy beach in Monterey Bay, California, during August 23-25, 1995. Shallow reflection and refraction data were acquired every 20-30 min., while the water table in the sand was changed in response to the nearby ocean tide. Water table change was monitored directly in a shallow well, and *insitu* saturation measurements from the upper 30 cm of the sand were taken as well.

This chapter reviews the field results and the basic theory used to model them. The high- resolution experiment provides a valuable link between laboratory data and field scale data. The results demonstrate the effects of fluid substitution *insitu* as inferred from surface seismics. I show that (1) shallow water table reflections can be imaged from depths as shallow as ~2m; (2) the reflections do not correspond to the water table as defined by the phreatic surface, but rather both the reflections and refractions are influenced by partial saturation and therefore are sensitive to the history of the flow; (3) the wave velocity in porous sand can be directly converted into saturation. These results together are important for the use of shallow seismic for hydraulic monitoring. This chapter was published under the chapter title by Bachrach and Nur, 1998.

Chapter 4 describes the results from the velocity analysis of the data collected in our beach experiments. The surface seismic experiment provided a unique

opportunity to analyze the seismic response of unconsolidated sediment at very low pressures.

In this chapter I try to answer several fundamental questions which arose from the velocity measurements and the seismic interpretation: (1) How slow can velocity in sand be? (2) What is the relation between the overburden (effective stress) and the seismic velocity? (3) What is the best way to relate shallow refraction data (first-layer velocity from refraction measurements) to the velocity calculated from the reflections? (4) How well will the ray-theory approximation work if the velocity gradient is very high?

I found in this study some specific conclusions: (1) The velocity gradient in unconsolidated sand is very high at shallow depths, with velocities that are much lower than the velocity of sound in air. The lowest velocity physically possible for an aggregate of sand and air is ~13 m/s. (2) The Hertz-Mindlin theory (Mindlin, 1949) qualitatively describes the vertical velocity profile in the sand. However, a quantitative description is still needed. I also show that (3) field calibration can be done from the seismic data.

In addition, the results have general implications for shallow seismic data. The low velocity that was measured in the sand, together with the high velocity gradient reflects the complexity of shallow seismic acquisition in low velocity environments. The wavelength, is extremely small when the velocity is very low. The shallow reflections usually contain high frequencies, and are often convolved with the ground roll. Therefore very close geophone spacing is needed to avoid spatial aliasing of the signal (especially the ground roll), which is often mistaken for reflections (Steeples et al, 1997). In our case the ability to image the reflections at 16 ms at such high frequencies was possible only due to the extremely short geophone interval we used (0.2 m). The use of very small geophone interval is extremely important in cases where the target is very shallow and the velocities are low. This work was done with Jack Dvorkin and Amos Nur, and was published under the chapter title by Bachrach et al., 1998.

Chapter 5 is direct continuation of Chapter 4. The P-wave data collected at Moss Landing beach left many questions unresolved. For example, how do the acoustic properties of unconsolidated granular materials relate to their physical characteristics (e.g., effective pressure, mineralogy, and porosity)? What is the shear wave velocity in unconsolidated, loose sands at low pressure? These questions are crucial for interpreting sonic and seismic measurements in sediments widely represented in

many depositional environments. Numerous measurements of elastic-wave velocities in such systems have been conducted in the lab and *insitu*, and theoretical models developed (see overviews in White, 1983; Wang and Nur, 1992). However, I am concerned with the acoustic properties of dry or partially saturated unconsolidated sands at a very low effective pressure (up to 0.1 MPa or 15 psi), which corresponds to either very shallow (several feet) sediments or overpressured reservoirs. Laboratory measurements at such low pressures are hard to conduct because of transducer-sand coupling problems. There are very few existing *insitu* measurements (White, 1983, Hunter, 1998) of shallow systems, and they deal with depth ranges greater than those of our interest.

My approach was to conduct a three-component surface seismic experiment on a beach with closely-spaced (0.3 m apart) geophones. By so doing, I was able to reconstruct the vertical velocity profile at a very shallow depth. My next goal was to find an appropriate theoretical model to match the observations.

I show the following: (1) The Poisson ratio of Moss Landing beach sand is 0.15. This can be modeled by a binary effective aggregate of grains with no tangential contact stiffness and of grains with no slip boundary conditions. (2) The sand shear wave velocities are lower than the velocities predicted from random packing of identical spheres. This discrepancy can be explained by the angularity of the grains. Thus, the difference between the expected velocity and the measured velocity can serve as a measure of the grain angularity. I note that this measure is a mechanical measure and is not directly related to the simple average angularity that is often used in sedimentology for sand classification. (3) The functional dependence of the shear wave velocity is general and does not apply only to Moss Landing beach sand. This dependence is observed in other depositional environments(e.g. glacial sediments). This work was done in collaboration with Jack Dvorkin.

In chapter 6, I introduce the ultra-shallow seismic reflection concept. Shallow seismic reflection is an underdeveloped field (Steeples et al. 1997). Typically high-resolution shallow seismic reflection survey target reflections in the "optimum" window range (Hunter at al, 1984), defined as the zone between the first arrivals and the groundroll. In this zone, the reflections are not contaminated by the groundroll, and can be easily imaged. However, using the optimum window technique does not allow for imaging at very short offsets, and therefore reflections shallower than 35-50ms are difficult to image. Hence, using the optimum window concepts limits the

reflection profile to depth of more than 5-10m. For ultra-shallow imaging (within 5-10m depth), one must image the reflections inside the groundroll.

The attenuation of groundroll is typically done using geophone arrays (e.g. Dobrin, 1988) or frequency filtering (Steeples et al., 1997). Geophone arrays are not very useful in ultra-shallow reflection surveys because the dimensions of such arrays are typically larger than the required station spacing. Therefore, frequency filtering is the only effective tool for attenuating groundroll. The ability to obtain shallow reflections is dependent on the separation of groundroll and reflected energy in the frequency domain. In this chapter I show that in unconsolidated sediments, where velocities are primarily pressure dependent, this separation can be achieved, and actually is theoretically expected.

In chapter 7, I go back to the fluid identification problem. I show that we can obtain water table image with a depth accuracy of centimeters. I present a field example of combining ground-penetrating-radar (GPR) with high-resolution shallow seismic where we detected water table and flow barriers. I also discuss the integration of high-resolution geophysical methods in general hydrological site characterization. The relation between the subsurface water table, saturation, and the hydraulic conductivity is often used for estimating hydraulic conductivity using different inversion methods. I show that the ability to image the water table and the saturation, using surface geophysical methods, together with flow simulations, can significantly improve the characterization of a site. This approach also provides a useful tool for evaluating the performance of seismic methods and GPR in different field conditions.

1.3 REFERENCES

Bachrach, R. and Nur, A.,1998, High resolution shallow seismic experiments in sand part I: Water table, fluid flow and saturation: Geophysics, **63**, in press.

Bachrach, R., Dvorkin, J. and Nur, A., 1998, High resolution shallow seismic experiments in sand part II: Velocities in shallow, unconsolidated sands: Geophysics, **63**, in press.

Biot, M. A.,1956, Theory of propagation of elastic waves in fluid saturated porous solid. I. Low frequency range, II. Higher frequency range: J. Acoust. Soc. Am., **28**,168-191.

Biot, M. A.,1962, Mechanics of deformation and acoustic propagation in porous media: J. Appl. Phys, **33**, 1482-1498.

Dobrin, M. B. and Savit, C. H., 1988, Introduction to geophysical prospecting, New-York: McGRAW-HILL book company.

Dvorkin, J., and Nur A., 1993, Dynamic poroelasticity: A unified model with the squirt and Biot mechanisms: Geophysics, **58**, 524-533.

Hunter, J. A., Pullan, S. E., Burns, R. A., Gagne, R. and Good, R., 1984, Shallow reflection mapping of the overburden bedrock interface with engineering seismograph- Some simple techniques, Geophysics, **49**, 1381-1385.

Hunter, J, 1998, Shear wave measurements for earthquake hazards studies, Faser river delta, British Colombia: Proceedings of the symposium on the application of geophysics to enviromental and engineering problems.

Mavko, G., and Nur, A., 1979, Wave attenuation in partially saturated rocks: Geophysics, **44**, 161-178.

Mindlin, R., D., 1949, Compliance of elastic bodies in contact, J. Appl. Mech., **16**, 259-268.

Murphy, W., F., 1982, Effects of microstructure and pore fluids on the acoustic properties of granular sedimentary materials, Ph.D. Thesis, Stanford University.

Nur, A., and Seimmons, G., 1969, The effect of saturation on velocity in low porosity rocks, Earth Planet. Sci. Lett., **7**, 183-193.

Steeples, D. W., Green, A. G.; McEvilly, T. V., Miller, R. D., Doll, W. E. and Rector, J. W., 1997, A workshop examination of shallow seismic reflection surveying, The leading edge, **16**, 1641-1647.

CHAPTER 2

FLUID DISTRIBUTION AND VELOCITY-FREQUENCY DISPERSION: INTEGRATION OF LOCAL SQUIRT FLOW WITH BIOT POROELASTIC THEORY VIA PORE PRESSURE DISTRIBUTION

2.1   ABSTRACT

We introduce a model to calculate acoustic velocities in rock with two fluid phases. The fluids are not mixed at the pore level. Rather they are arranged in macroscopic patches with regions fully saturated with one phase adjacent to regions fully saturated with the second phase. One realization of such an arrangement is a partially saturated rock with liquid located in fully saturated patches. The model combines the macroscopic squirt-flow mechanism (cross-flow between adjacent patches) and the local squirt-flow mechanism (cross-flow on the pore scale). The local squirt-flow theory is integrated into poroelastic Biot's formalism by accounting for the pore pressure distribution and its affect on the squirt flow mechanism. The elastic moduli as well as porosity and permeability may vary between two adjacent regions in a rock that are saturated with different fluids -- we can model, for example, the viscoelastic parameters of a system where a fully saturated clay lens is surrounded by dry sand. The theory is adequately verified by laboratory data. Potential applications include synthetic modeling for recognizing fluid distribution in rock and soil from seismic analysis, and detecting patches of viscous contaminants in the shallow subsurface.

2.2   INTRODUCTION

The wave-induced dynamics of fluid-solid interaction in rock at full saturation has been modeled based on two physical mechanisms: Biot's mechanism (e.g., Biot, 1956 and 1962), and the squirt-flow mechanism (e.g., Mavko and Nur, 1979; Dvorkin et al., 1993). In the former model, pore fluid is coupled to the solid frame by viscous friction and inertial coupling. The latter model accounts for the fluid's squirting from thin compliant cracks, deformed by a passing wave, into larger pores. Both models predict that the velocities increase with increasing frequency (an effect called

velocity-frequency dispersion). In consolidated rocks, squirt flow usually accounts for much larger viscous losses than the Biot flow. This is why the Biot model, if used separately from the squirt-flow model, underestimates the amount of attenuation and velocity-frequency dispersion.

At partial saturation the fluid-rock interaction becomes more complex. It depends not only on the properties of the solid, liquid, and gas phases, but also on the arrangement of the fluid in the pore space. The effect of pore fluid on acoustic velocities has been experimentally studied at different frequencies and different saturations (e.g., Murphy, 1982; Cadoret, 1993). Data show that at least two scales of saturation heterogeneity may be present in rock: (1) the pore-scale heterogeneity where liquid and gas co-exist in the same pore, and (2) the patch-scale heterogeneity where a fully-saturated patch (orders of magnitude larger than a pore) is surrounded by a dry or undersaturated region. The scale of heterogeneity may depend on the process of saturation (Knight and Nolen-Hoeksema, 1990; Cadoret, 1993). It is clear that where both saturation heterogeneity scales are present, two scales of squirt flow are possible: the macroscopic squirt-flow mechanism (cross-flow between adjacent patches) and the local squirt-flow mechanism (cross-flow on the pore scale).

White (1975) modeled the macroscopic squirt-flow mechanism by examining pore-fluid cross flow between a fully-saturated region and a gas pocket. Dutta and Ode (1979) rigorously addressed the same problem using Biot's dynamic poroelasticity equations.

Mavko and Nolen-Hoeksema (1994) modeled the high-frequency velocity limit for a partially-saturated rock where both saturation heterogeneity scales are present. They found that both global and local squirt-flow mechanisms contribute to the rock's stiffness.

The pore-scale saturation heterogeneity may be responsible for large variations in rock stiffness. Endres and Knight (1991) theoretically modeled this effect by assuming ellipsoidal pores with a range of aspect ratios. The model predicts that at high frequencies, the rock is stiffer when liquid is in the soft, high aspect ratio, pores. The rock is softer when there is gas in the soft pores.

The goal of this paper is to theoretically combine the local squirt-flow mechanism and the macroscopic squirt-flow mechanism in order to estimate acoustic velocities in a rock with patchy saturation at all frequencies. In order to reduce the number of independent variables we assume that each patch is fully-saturated with a single fluid. In other words, we only model the patch-scale (rather than pore-scale) saturation

heterogeneity. Therefore, this work may be considered as a step in developing the White-Dutta-Ode model.

We find that if the liquid has low viscosity (water) the local squirt flow is important only at ultrasonic frequencies. In this case, the macroscopic squirt flow is responsible for velocity-frequency dispersion at practical frequencies of 0.01 - 10 kHz. However, if the liquid has viscosity on the order of hundred cPs, such as a low-API oil or a viscous contaminant (lubricant), the local squirt-flow mechanism has to be accounted for. Therefore, this model may be useful for estimating the effects of patchy saturation in well logging, crosswell tomography, and environmental shallow seismic applications.

The model uses several hard-to-measure parameters, such as, the average radius of a saturated patch. The usefulness of the model is in its forward-modeling power. For example, if a viscous contaminant is expected to be present in patches in the shallow subsurface, a series of synthetic seismic images can be generated at different frequencies (Figure 1). These images can be adjusted to the actual seismic maps obtained at different frequencies. Then an elusive parameter (or, at least, its bounds) can be estimated.
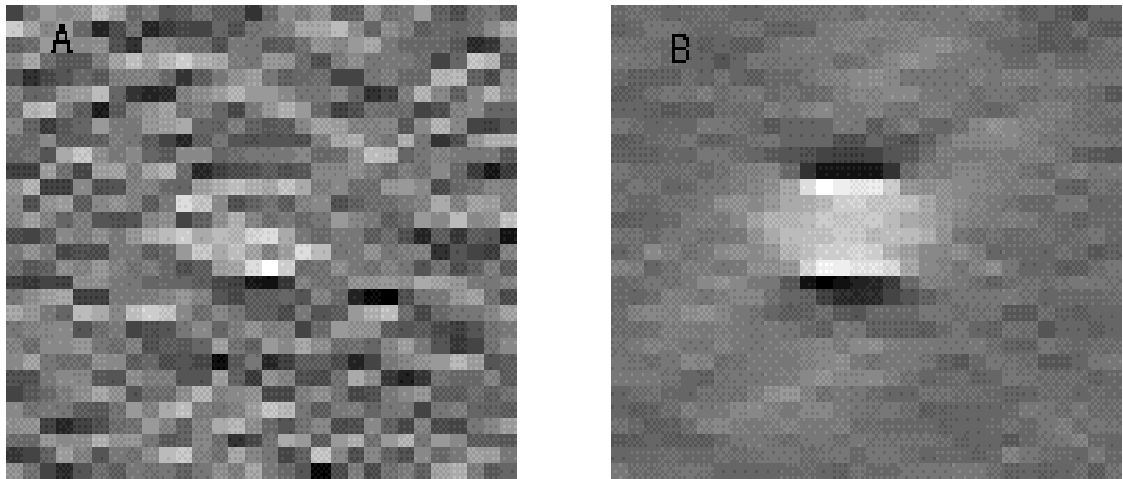
Figure 1. Synthetic seismic image of a region with viscous contaminant present in patches. The background is dry rock with random lithologic noise. a. frequency is 500 Hz, the region is invisible. b. frequency is 3 kHz, the contaminated region becomes visible. The model uses only the macroscopic squirt-flow mechanism. Synthetic imaging was conducted using the Born approximation of diffraction tomography (Wu and Toksoz, 1987) for a surface seismic survey.

2.3   QUALITATIVE MODEL

2.3.1   Macroscopic and microscopic squirt flow

Experimental observations (e.g., Cadoret, 1993) suggest that in many cases pore fluids are not mixed at the pore level. Rather they are arranged in macroscopic patches of a size largely exceeding the pore scale. If at partial saturation a fully saturated patch is surrounded by an undersaturated region (Figure 2a) then a passing seismic wave will result in a pore-fluid cross-flow between the patch and the surrounding rock. We call this cross-flow the macroscopic, or global, squirt flow. At a low frequency, pore pressure in the patch will be at equilibrium with the surrounding gas. Therefore, the patch will deform as an open system with an effective stiffness equal to that of the dry rock. However, if a frequency is very high, the fluid will be unrelaxed with pore pressure different from the surrounding region. The patch will deform as a closed system with the stiffness of the fully saturated rock. A transition between the two limits takes place at intermediate frequencies.

In saturated rock, pore fluid cross-flow takes place not only at the macroscopic but also at the pore scale (Figure 2b). Here fluid is forced to flow from soft, compliant, pores into stiffer pores (e.g., Mavko and Jizba, 1991; Dvorkin et al., 1995). At low frequency, fluid pressure in thin compliant pores is expected to equilibrate with the pressure in the stiff pore space. Then the effective properties of the saturated rock can be calculated from Gassmann's (1951) equation. At a very high frequency the fluid in the thin pores will be unrelaxed (frozen) and will add to the effective stiffness of the rock. As a result, acoustic velocity increases. Again, as in the macroscopic squirt-flow case, one can expect a transition between these two (low-frequency and high-frequency) limits. In both cases (the macroscopic and the microscopic squirt flow) the transition frequency is strongly affected by fluid viscosity, rock permeability, and the characteristic length of fluid flow. This length is the size of a patch for the macroscopic flow and approximately the length of a pore-scale compliant crack for the local flow.
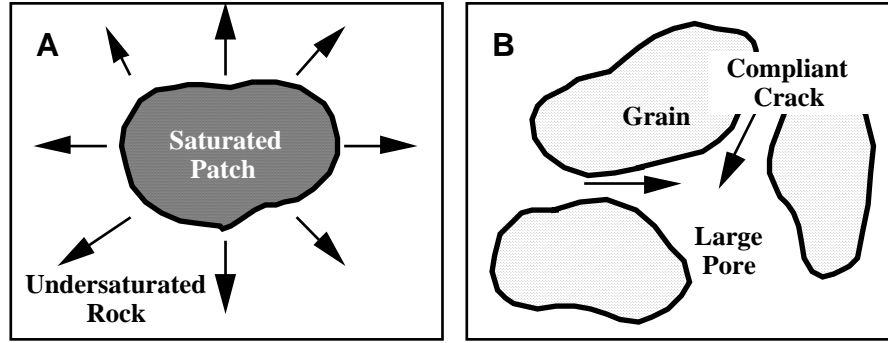
Figure 2. a. Macroscopic squirt flow. b. Local squirt flow.

This macroscopic squirt-flow model was first offered by White (1975), who examined the effective acoustic properties of rock with gas bubbles. Dutta and Ode (1979) extended the model by using the Biot dynamic poroelasticity equations to account for the solid-fluid coupling. We systematically use this model and extend it by taking the local squirt-flow mechanism into consideration.

2.3.2   Integrated model

Both the macroscopic and microscopic squirt flow occur in rock simultaneously. To integrate the two we use the following iterative scheme. First we calculate pore pressure and stress in a saturated patch by considering only the macroscopic squirt-flow mechanism (Biot's poroelasticity equations). Next we average these stress and pressure fields over the patch and use these average values to calculate the microscopic squirt-flow effect (Dvorkin et al., 1995). Because of the stiffening effect of the local flow, the elastic moduli of the rock frame will change. We calculate them and, in the final iteration, substitute the new moduli into the macroscopic squirt-flow equations.

2.4   QUANTITATIVE MODEL

We adopt the formalism of Dutta and Ode (1979) to solve Biot's equations and integrate squirt flow into them. Thus we use spherical coordinates. The problem can be formulated in the Cartesian coordinate system as well (as given in appendix E).

We assume that a fully-saturated patch is a sphere and the problem has spherical symmetry. We also assume that all parameters are harmonically time-dependent. For example, the radial stress in the rock, σ, is

$$\sigma(r,t) = \sigma(r)e^{-i\omega t},$$

where t is time, r is the radial coordinate, and ω is the angular frequency. In all equations below we use only the radially-dependent factor of a parameter.

2.4.1 Macroscopic squirt flow and dynamic poroelasticity

We quantify the effect of the macroscopic squirt flow on acoustic velocities by calculating the effective elastic moduli of a homogeneous, fully-saturated spherical patch of radius R. This patch is surrounded by fully-saturated rock with a different pore fluid (e.g., air). The effective bulk modulus of the patch, K_{eff}, is found by relating the applied radial stress σ_0 on the patch boundary to the resulting fractional volume change $\Delta V / V$ of the patch:

$$K_{eff} = \frac{-\sigma_0}{\Delta V / V} = \frac{-\sigma_0 R}{3u(R)}, \tag{1}$$

where u is the rock-matrix displacement, and V is the volume of the patch. By using equation (1), we assume that the patch is hydrostatically deformed by a passing seismic wave. Of course, this means that the size of the patch is much smaller than the wavelength.

We take the effective shear modulus of the saturated patch equal to that of the dry patch. The rationale for this assumption is that a shear wave does not change the volume of the patch and thus does not result in macroscopic fluid flow.

In order to find displacement u in equation (1) we employ the Biot dynamic poroelasticity equations with spherical symmetry. Their general solution is (Appendix A):

$$
\begin{aligned}
u(r) &= A_1 j_1(\lambda_1 r) + \tilde{A}_1 n_1(\lambda_1 r) + A_2 j_1(\lambda_2 r) + \tilde{A}_2 n_1(\lambda_2 r), \\
w(r) &= B_1 j_1(\lambda_1 r) + \tilde{B}_1 n_1(\lambda_1 r) + B_2 j_1(\lambda_2 r) + \tilde{B}_2 n_1(\lambda_2 r),
\end{aligned}
\tag{2}
$$

where w is the displacement of the pore fluid relative to the matrix; $j_1(Z)$ and $n_1(Z)$ are the spherical Bessel functions; and A_1, $\tilde{A}_1$, A_2, $\tilde{A}_2$, B_1, $\tilde{B}_1$, B_2, and $\tilde{B}_2$ are constants. Only four of these eight constants are independent:

$$A_1 = -C_1 B_1, \, A_2 = -C_2 B_2, \, \tilde{A}_1 = -C_1 \tilde{B}_1, \, \tilde{A}_2 = -C_2 \tilde{B}_2.$$

Parameters C_1, C_2, λ_1, and λ_2 are expressed through the poroelastic constants in Appendix A.

The constants in equation (2) are to be determined from the boundary conditions on the surface of the patch. These conditions depend on the character of the surrounding region. For example, if the patch is surrounded by dry rock, we use the zero-pressure condition at $r = R$. Other cases are discussed below.

2.4.2 Microscopic squirt flow

To describe the microscopic squirt flow in a fully saturated rock we follow the approach of Dvorkin et al. (1995). The modified solid phase of a rock is defined as the mineral phase plus thin compliant cracks and grain contacts. Then the bulk modulus of the modified solid, K_{ms}, is smaller than that of the mineral phase, K_s. Similar to the dry rock frame that corresponds to the mineral phase, the modified dry frame corresponds to the modified solid. The bulk and the shear moduli of the modified frame are K_m and G_m, respectively. These moduli can be found from the following equations:

$$\frac{1}{K_m} = \frac{1}{K_{ms}} + \frac{1}{K_{hp}} - \frac{1}{K_s}, \quad \frac{1}{G_d} - \frac{1}{G_m} = \frac{4}{15}(\frac{1}{K_d} + \frac{1}{K_{md}}), \tag{3}$$

where

$$K_{ms} = \frac{K_{msd} + \alpha_{ms} K_s(1 - f(\xi))}{1 + \alpha_{ms}\frac{\partial P}{\partial \sigma}}, \quad K_{msd} = [\frac{1}{K_s} - \frac{1}{K_{hp}} + \frac{1}{K_d}]^{-1},$$

$$\alpha_{ms} = 1 - \frac{K_{msd}}{K_s}, \quad f(\xi) = \frac{2J_1(\xi)}{\xi J_0(\xi)}, \quad \xi = \sqrt{i\omega}Z, \tag{4}$$

$$\frac{1}{K_{md}} = \frac{1}{\tilde{K}_{ms}} + \frac{1}{K_{hp}} - \frac{1}{K_s}, \quad \tilde{K}_{ms} \approx K_{msd} + \alpha K_s[1 - f(\xi)];$$

$J_1(\xi)$ and $J_0(\xi)$ are the first- and zero-order regular Bessel functions, respectively; Z is an experimental parameter which describes the viscoelastic behavior of the rock, it is proportional to the characteristic length of the microscopic squirt flow; K_d and G_d are the dry-rock bulk and shear moduli, respectively; and K_{hp} is the dry-rock bulk modulus at high pressure.

2.4.3 Integrated model

Equations (A-10) in Appendix A relate the stress and pore pressure to u and w. These quantities depend on the radial coordinate, r. In order to simplify the solution of the problem we assume that the microscopic squirt flow parameters are coordinate-independent within a patch. Then we use the average value of $\partial P / \partial \sigma$ instead of its exact value, the former given by

$$\left\langle \frac{\partial P}{\partial \sigma} \right\rangle = \frac{\int\limits_V P_f dV}{\int\limits_V \sigma dV}. \tag{5}$$

If we consider, for example, a fully-saturated patch with the no-flow boundary condition at its surface, σ and P_f will be uniform throughout the patch. Then $\partial P / \partial \sigma$ given by equation (5) is identical to that found from Gassmann's (1951) equation (Dvorkin et al., 1995):

$$\frac{\bar{\partial} P}{\partial \sigma} = \frac{-1}{\alpha_0 (1 + \dfrac{K_d \phi}{\alpha_0^2 F_0})}, \; \alpha_0 = 1 - \frac{K_d}{K_s}, \; F_0 = [\frac{1}{K_f} + \frac{\alpha_0 - \phi}{\phi K_s}]^{-1}.$$

The algorithm for implementing the integrated model is: (a) use equations (2) and (A-10) with the appropriate boundary conditions to find σ and P_f; (b) use equation (5) to calculate $\langle \bar{\partial} P / \bar{\partial} \sigma \rangle$; (c) by using this derivative, find K_m, K_{ms}, and G_m from equations (3) and (4); (d) use equations (2) with the new, modified, poroelastic parameters; and (e) use equation (1) to calculate the effective bulk modulus of the patch. The shear modulus of the patch will be the modified-frame shear modulus as given by equation (3). In other words, we use a single-iteration procedure. The step-by-step implementation of this algorithm is given in Appendix B.

2.5   ANALYSIS: THE SINGLE-PATCH CASE

First, we solve the case of a single spherical saturated patch surrounded by dry rock. We can use the zero-pressure boundary condition on the sphere's surface. In this case the constants $\tilde{A}_1$, $\tilde{A}_2$, $\tilde{B}_1$, and $\tilde{B}_2$ in equation (2) should vanish since the

function $n_1(Z)$ approaches infinity as its argument approaches zero. The other constants are (Appendix C):

$$A_1 = \sigma_0 / \{(H + 2\lambda_E)[j_1(\lambda_1 R) - Tj_1(\lambda_2 R)] / R - H[\lambda_1 j_2(\lambda_1 R) - T\lambda_2 j_2(\lambda_2 R)] +$$
$$+ 2\alpha D(-C_1[3j_1(\lambda_1 R) / R - \lambda_1 j_2(\lambda_1 R)] + TC_2[3j_1(\lambda_2 R) / R - \lambda_2 j_2(\lambda_2 R)]\},$$
$$A_2 = TA_1; \tag{6}$$
$$T = -\frac{(\alpha - C_1)}{(\alpha - C_2)} \frac{[3j_1(\lambda_1 R) / R - \lambda_1 j_2(\lambda_1 R)]}{3j_1(\lambda_2 R) / R - \lambda_2 j_2(\lambda_2 R)}.$$

2.5.1 Relative effects of macroscopic and microscopic squirt flow

In this example we assume that the dry-rock elastic constants and porosity are those of Massillon sandstone (Murphy, 1982). The calculation parameters are given in Table 1. The radius of the patch is 0.02 m. Permeability in this example is assumed to be 1 mD, fluid viscosity is 1 cPs. The modeling results are presented in Figure 3.

When the frequency of a passing wave is low, the pressure in the sphere has enough time to reach equilibrium with the outside (zero) pressure. Similar equilibrium is reached at the pore scale. The patch deforms as an open system and the effective bulk and shear moduli of the patch become those of the dry rock

Table 1: Rock properties for the numerical model. The sandstone data are from Murphy (1982) and the limestone data are from Cadoret (1993). The elastic moduli are in GPa, density in g/cm^3, permeability in mD, and length in cm.

Rock	K_d	G_d	ρ_s	ϕ	K_{hp}	K_s	k	Z	b
Massillon Sandstone	9.64	7.25	2.61	0.23	21	32.2	760	0.01	0.3
Fort-Union Sandstone	12.66	15.75	2.55	0.085	23.9	31	0.075	0.05	0.2
S3 Limestone	6.6	7.32	2.71	0.235	9.86	53.2	7.47	0.004	0.2
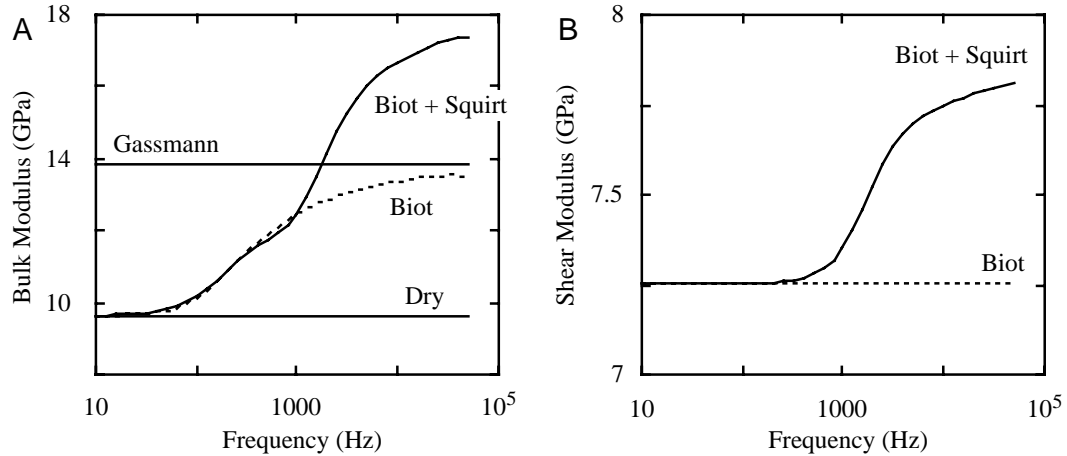
Figure 3. Bulk (a) and shear (b) moduli of a single spherical patch. Dotted lines are from the macroscopic squirt-flow model without the microscopic squirt-flow effect ("Biot"). Solid curves are from the integrated model ("Biot + Squirt"). The straight lines show the bulk modulus of the dry rock ("Dry"), and the low-frequency bulk modulus of the saturated rock ("Gassmann").
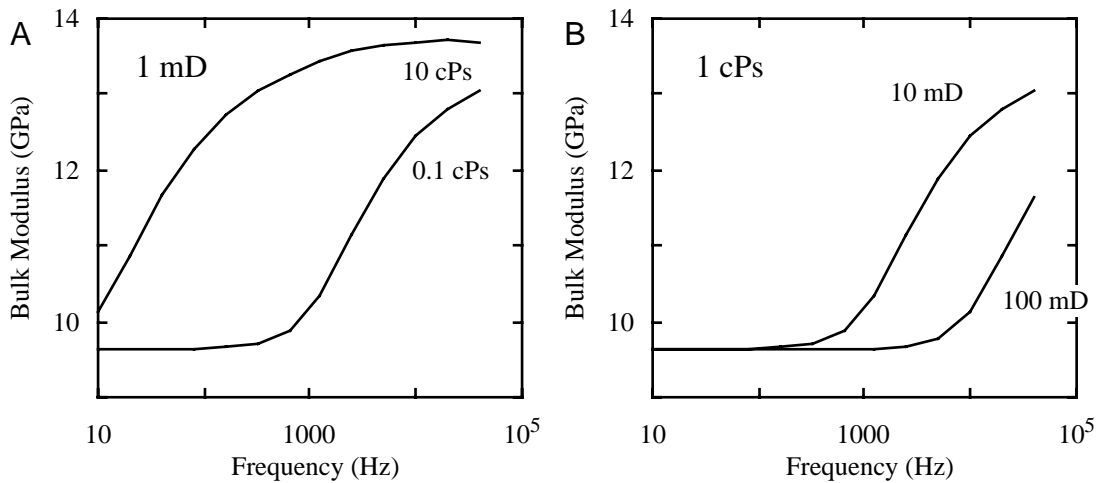
Figure 4. The effective bulk modulus of a saturated patch versus frequency. a. The effect of viscosity. b. The effect of permeability.

When frequency increases, fluid pressure inside the patch cannot equilibrate with the outside pressure. If we take into account only the macroscopic squirt-flow effect, the high-frequency limit of the effective bulk modulus is that obtained from Gassmann's (1951) equation. The local flow effect acts to further stiffen the frame of the rock, resulting in increased effective bulk and shear moduli of the patch.

2.5.2   Effects of viscosity and permeability

We illustrate the influence of viscosity and permeability on the effective bulk modulus of the patch by using only the macroscopic squirt-flow mechanism. The additional effect of the microscopic squirt flow is qualitatively similar, it is discussed in Dvorkin et al. (1995). The elastic dry-rock properties of the patch and its size are the same as in the previous example. First we fix the permeability at 1 mD and change the viscosity of the fluid from 0.1 to 10 cPs (Figure 4a). As a result, the transition from the low- to high-frequency behavior shifts towards higher frequencies. The result of increasing the permeability of rock is similar to that of decreasing fluid viscosity (Figure 4b). In the latter example the fluid viscosity was fixed at 1 cPs.

2.5.3   Effect of patch size

An important parameter that influences the effective bulk modulus of a patch is its radius R. This is the length of the macroscopic squirt flow. The larger R the longer it takes for the pore pressure inside the patch to equilibrate with the outside pressure. If R is large, pore pressure will be high in the patch even at a low frequency thus adding to the stiffness of the rock. If R is small, the fluid pressure can quickly equilibrate and the rock will appear relatively soft even at a high frequency (Figure 5). In this example the dry-rock elastic constants and porosity are those of Fort Union sandstone (Murphy, 1982). Their values are given in Table 1.
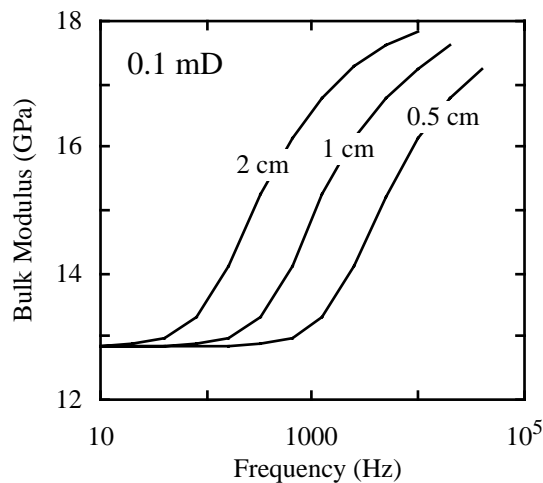
Figure 5. The effective bulk modulus of a saturated patch versus frequency for different patch radii (shown in the figure).

2.6 PARTIALLY SATURATED ROCK

2.6.1 Model

Consider a rock at saturation S. Following White (1975), we calculate the effective elastic moduli of the rock as those of a spherical patch that has two domains: an inner sphere, and a spherical shell around it (Figure 6). If S is between 0 and 0.64 then the inner sphere is fully-saturated, and the outer shell is dry (the water bubble configuration). If S is between 0.36 and 1 then the inner sphere is dry, and the outer shell is fully-saturated (the gas bubble configuration). These saturation boundaries are consistent with the topology of placing spherical patches within a rock -- the porosity of a random pack of identical spheres is about 0.36 (Figure 7). Of course, the two saturation domains overlap. The results of using both geometrical arrangements in the overlap region are approximately the same (Figure 8).
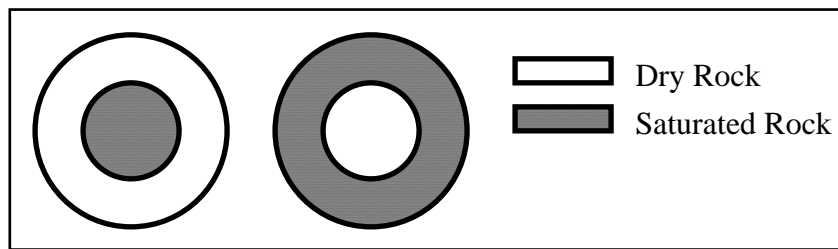
Figure 6. Left: a saturated sphere inside a dry shell; right: a dry sphere inside a saturated shell.
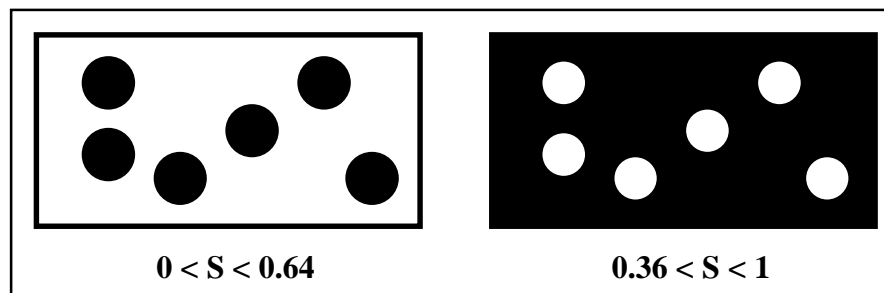
Figure 7. The two domains of partial saturation.
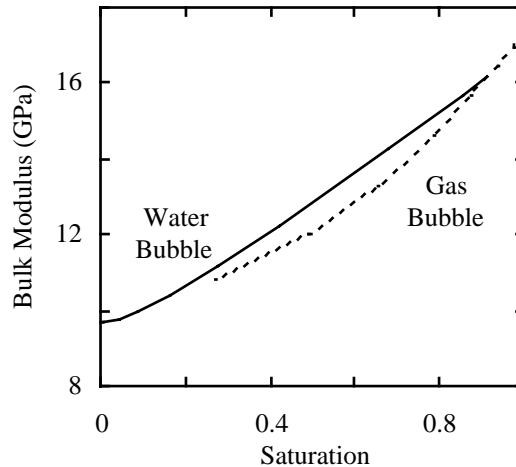
Figure 8. The two domains of partial saturation. The solid line is for the water-saturated sphere surrounded by a gas-saturated shell ("Water Bubble"); the broken line is for a gas-saturated sphere surrounded by a water-saturated shell ("Gas Bubble"). The rock is Massillon sandstone (see Table 1).

The effective bulk modulus of a two-domain patch is calculated from equation (1). Here we have to solve the poroelasticity equations in both domains of the patch. The method of solution is similar to that described in the previous sections. The derivations are given in Appendix D. The effective shear modulus of the two-domain patch is found as the average of the shear moduli of the domains using either the upper or the lower Hashin-Shtrikman bound (Hashin and Strikman, 1963). In the problems under consideration, these bounds are very close because the material properties in the two domains are very similar.

2.6.2 Sandstone example

We use the model to simulate the elastic response of partially-saturated Massillon sandstone and Fort-Union sandstone samples (Murphy, 1982). The properties of the samples are summarized in Table 1. The resonant-bar (low-frequency) measurements were conducted without confining pressure applied. In the ultrasonic experiments, a small (0.5 MPa) axial pressure was applied to ensure adequate transducer coupling. The theoretical elastic-wave velocities are calculated from the modeled effective moduli and the average density of a two-domain patch.

The macroscopic squirt flow model, which does not include the microscopic squirt-flow mechanism, clearly underestimates the P-wave velocity-frequency

dispersion (Figure 9). The integrated model allows us to increase the prediction accuracy. For shear waves both models give practically the same results.

The low-frequency velocities in these rocks were measured in resonant-bar experiments. In this case, the dry-rock velocities were smaller than those in the ultrasonic experiments. This effect might be due to the applied pressure in the ultrasonic experiments, and also to the variation of sample properties between the two experiments. Still, we use the rock properties given in Table 1. In order to compare our predictions to the experimental low-frequency data, we normalize all velocities at partial saturation by their values at zero saturation.

The results are given in Figure 9. Both model predictions (without the microscopic squirt-flow effect, and with it) are very close. They cannot mimic the Fort Union sandstone data, but are accurate for the Massillon sandstone. Note that in both cases the theoretical values do not match the experimental ones at full saturation. The reason is that our model is intended to be used at partial saturation. Thus we do not connect our partial-saturation model with the full-saturation model (e.g., Dvorkin et al., 1995).
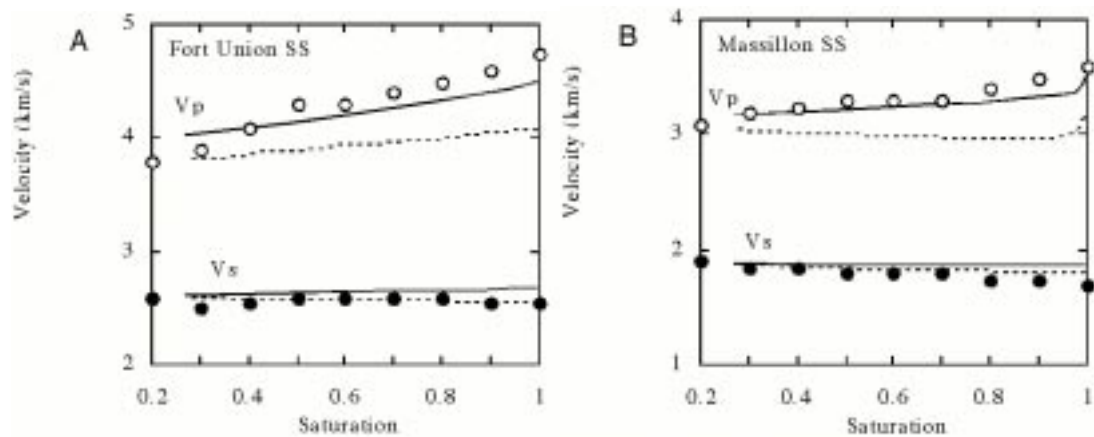
Figure 9. Velocities for Fort-Union (a) and Massillon (b) sandstones at 200 kHz versus saturation. The circles are the data points as measured by Murphy (1982). The dotted lines are the model prediction accounting only for the macroscopic squirt-flow; the solid lines are the model prediction based on the integrated model. Open symbols are for P-waves, and filled ones are for S-waves.
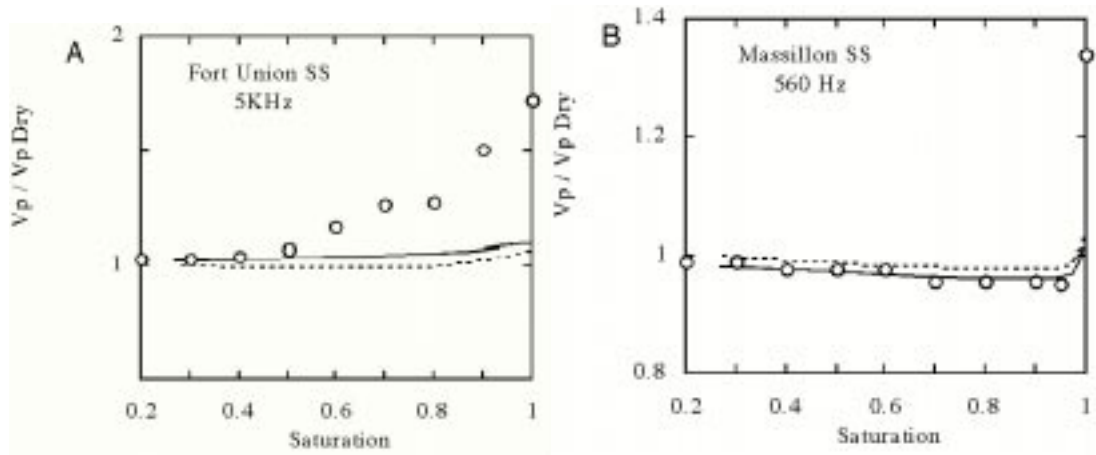
Figure 10. Normalized P-wave velocity versus saturation for Fort Union (a) and Massillon (b) sandstones. The symbols are data from Murphy (1982). The dotted lines are the model prediction accounting only for the macroscopic squirt-flow; the solid lines are the model prediction based on the integrated model.

2.6.3 Limestone example

The rock properties for limestone are summarized in Table 1. Both the resonant-bar (low-frequency) and ultrasonic measurements were conducted at 2.5 MPa confining pressure (Figure 11). Note that for this limestone sample the high-pressure bulk modulus is only about 1.5 its dry-frame value at the measurement pressure (for the above sandstone samples this ratio is about 2). This is why the microscopic squirt-flow contribution is smaller in this case than for the sandstone samples. In both cases the theoretical values do not match the experimental ones at full saturation. See the discussion in the previous section.

Note also that at ultrasonic frequency, the integrated model overpredicts the velocity values, whereas the purely macroscopic squirt model fits the data perfectly. An apparent reason is that the limestone sample under examination does not have thin compliant micro-cracks (Cadoret, 1993), which are responsible for the microscopic squirt flow. The observed velocity-pressure dependence is mostly due to the deformation of round pores. In such a case, using the microscopic squirt-flow correction is not appropriate.
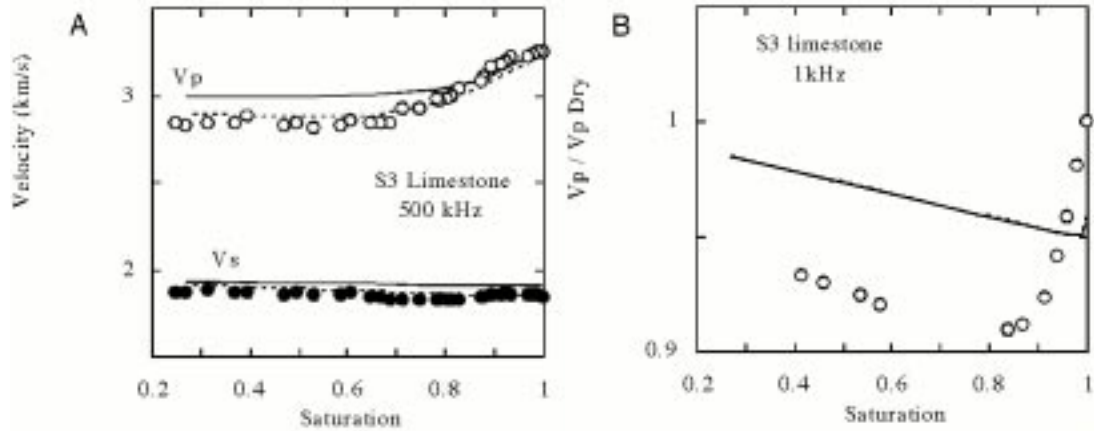
Figure 11. Velocities for S3 limestone at 500 kHz and 1 kHz.. The circles are the data points as measured by Cadoret (1993). The broken line is the model prediction accounting only for the macroscopic squirt flow; the solid line is the model prediction based on the integrated model. Open symbols are for P-waves, and filled ones are for S-waves.
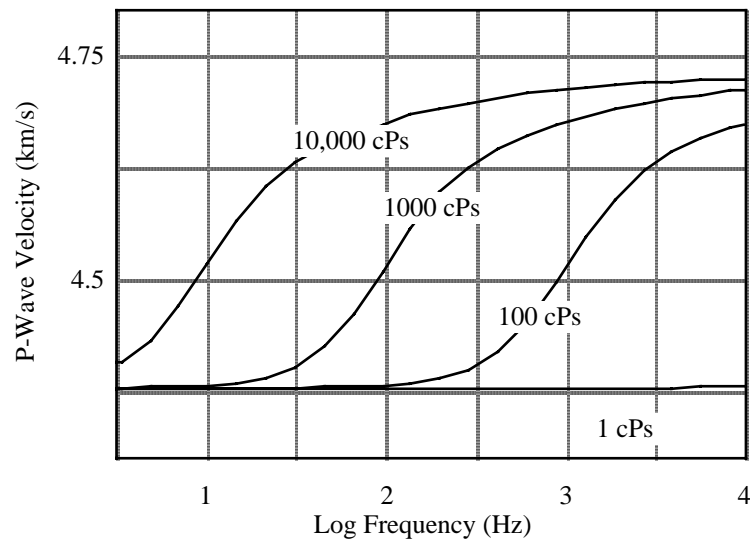
Figure 12. Velocity-frequency changes in Navajo sandstone with different saturants. The numbers indicate pore-fluid viscosity. The transition from low-frequency behavior to high-frequency behavior occurs, for a moderately viscous contaminant, at the frequency of 1 kHz. Based on Dvorkin and Nur (1993), and Dvorkin et al. (1994, 1995).

2.7 SUMMARY AND CONCLUSIONS

We present here a model which links stress oscillations to velocity dispersion in partially saturated rock by *physically* linking pore-scale hydrodynamics to fluid flow in porous media (given by Darcy's Law, which is integrated in Biot's formulation). This model is consistent with observations and makes the following predictions:

- At partial saturation at least two solid-fluid interaction mechanisms contribute to the effective elastic properties of rock: the macroscopic (global) squirt flow, and the microscopic (local) squirt flow.
- If the elastic-wave velocities in a rock are weakly pressure-dependent, the macroscopic squirt-flow mechanism dominates, and the microscopic squirt flow can be neglected.
- At low frequencies (below 10 kHz), and for low-viscosity pore fluids, the microscopic squirt-flow mechanism can be neglected.
- However, if the pore fluid is viscous (heavy oil, viscous contaminants), the microscopic squirt-flow mechanism may have a significant effect on wave velocities at sonic (1 - 10 kHz) frequencies.

The model presented can be useful in forward modeling of the seismic response of rock systems with heterogeneous saturation. It can be applied, for example, to detecting fluid distribution in rock and soil from seismic, and identifying patches of viscous contaminants in the shallow subsurface.

2.8 ACKNOWLEDGMENT

2.9 REFERENCES

Abramowitz, M. and Stegun, I., 1964, Handbook of mathematical functions with formulas, graphs and mathematical tables: U.S. Dept. of Commerce.

Berryman, J. G., 1980, Confirmation of Biot's theory: Appl. Phys. Lett., **37**, 382-384.

Biot, M. A.,1956, Theory of propagation of elastic waves in fluid saturated porous solid. I. Low frequency range, II. Higher frequency range: J. Acoust. Soc. Am., **28**,168-191.

Biot, M.A., 1961, Generalized theory of acoustic propagation in porous dissipative media: J. Acoust. Soc. Am., **34**, 1254-1264.

Biot, M. A.,1962, Mechanics of deformation and acoustic propagation in porous media: J. Appl. Phys., **33**, 1482-1498.

Cadoret, T., 1993, Effet de la saturation eau/gaz sur les propriétés acoustiques des roches: Ph.D. thesis, University of Paris.

Dutta, N. C., and Ode, H., 1979, Attenuation and dispersion of compressional waves in fluid filled rock with partial gas saturation (White model)- Part I: Biot theory: Geophysics, **44**, 1777-1788.

Dutta, N. C., and Ode, H., 1979, Attenuation and dispersion of compressional waves in fluid filled rock with partial gas saturation (White model) - Part II: Results: Geophysics, **44**, 1777-1788.

Dvorkin, J., and Nur A., 1993, Dynamic poroelasticity: A unified model with the squirt and Biot mechanisms: Geophysics, **58**, 524-533.

Dvorkin, J., Yin, H., and Knight, R., 1994, Seismic detection of residual contaminants: SEG expanded abstracts, Los Angeles, 1994, 594-586.

Dvorkin, J., Mavko, G, and Nur A., 1995, Squirt flow in fully saturated rocks: Geophysics, **60**, 97-107.

Endres, A. L., and Knight, R., 1989, The effect of microscopic fluid distribution on elastic wave velocities: The Log Analyst, 437-444.

Gassmann, F., 1951, Uber die elastizitat poroser medien: Vier. der Natur Gesellschaft, **69**, 1-23.

Hashin, Z., and Shtrikman, S., 1963, A variational approach to the elastic behavior of multiphase material: J. Mech. Phys. Solids, **11**, 127-140.

Knight, R., and Nolen-Hoksema, R., 1990, A laboratory study of the dependence of elastic wave velocities on pore scale fluid distribution, Geophysical Research Letters ,**17**, 1529-1532.

Mavko, G., and Nur, A., 1979, Wave attenuation in partially saturated rocks: Geophysics, **44**, 161-178.

Mavko, G. and Nolen-Hoeksema, R., 1994, Estimating seismic velocities at ultrasonic frequencies in partially saturated rocks, Geophysics, **59**, 252-258.

Mavko, G., and Jizba, D., 1991, Estimating grain-scale fluid effects on velocity dispersion in rocks: Geophysics, **56**,1940-1949.

Murphy, W. F., 1982, Effect of microstructure and pore fluids on the acoustic properties of granular sedimentary material: Ph.D.. thesis, Stanford University.

White, J. E., 1975, Computed seismic speeds and attenuation in rocks with partial gas saturation: Geophysics, **40**, 224-232.

Wu, R. S., and Toksoz, M. N., 1987, Diffraction tomography and multisource holography applied to seismic imaging: Geophysics, **52**, 11-25.

APPENDIX A

BIOT'S EQUATIONS IN SPHERICAL COORDINATES

Biot (1962) offers the following dynamic equations to describe the deformation of rock with fluid (also see Dutta and Ode, 1979):

$$\rho_b \frac{\partial^2 \vec{u}}{\partial t^2} + \rho_f \frac{\partial^2 \vec{w}}{\partial t^2} = H\nabla(\nabla \cdot \vec{u}) + 2\alpha D\nabla(\nabla \cdot \vec{w}),$$

$$\rho_f \frac{\partial^2 \vec{u}}{\partial t^2} + m\frac{\partial^2 \vec{w}}{\partial t^2} = 2\alpha D\nabla(\nabla \cdot \vec{u}) + 2D\nabla(\nabla \cdot \vec{w}) - \frac{\eta}{k}\frac{\partial \vec{w}}{\partial t},$$

(A-1)

where $\vec{u}$ is the displacement vector of the rock matrix, $\vec{w}$ is the displacement vector of the pore fluid relative to the matrix, ρ_b and ρ_f are the densities of the fully saturated rock and the pore fluid, respectively, m is the dynamic coupling coefficient, η is pore-fluid viscosity, k is permeability. H is parameter calculated as follows:

$$H = K_d + 2\alpha^2 D + \frac{4}{3}G_d, \quad \alpha = 1 - \frac{K_d}{K_s}, \quad D = \frac{K_s}{2}[\alpha + \frac{\phi}{K_f}(K_s - K_f)]^{-1},$$

$$m = (\phi\rho_f + \rho_a) / \phi^2,$$

where ϕ is porosity, K_d and G_d are the dry-rock (dry-frame) bulk and shear moduli, respectively, K_s and K_f are the bulk moduli of the solid (grain) and the fluid phase, respectively, and ρ_a is the dynamic coupling density.

The latter parameter can be calculated as follows:

$$\rho_a = \phi\rho_f(a-1),$$

where $a \geq 1$ is the dynamic tortuosity. For example, for the case of solid spherical particles in fluid (Berryman, 1980) $a = 0.5(1 + \phi^{-1})$.

For the spherical-symmetry case equations (A-1) transform into the following system:

$$\rho_b \frac{\partial^2 u}{\partial t^2} + \rho_f \frac{\partial^2 w}{\partial t^2} = H(\frac{\partial^2 u}{\partial r^2} + \frac{2}{r}\frac{\partial u}{\partial r} - \frac{2u}{r^2}) + 2\alpha D(\frac{\partial^2 w}{\partial r^2} + \frac{2}{r}\frac{\partial w}{\partial r} - \frac{2w}{r^2}),$$

$$\rho_f \frac{\partial^2 u}{\partial t^2} + m\frac{\partial^2 w}{\partial t^2} = 2\alpha D(\frac{\partial^2 u}{\partial r^2} + \frac{2}{r}\frac{\partial u}{\partial r} - \frac{2u}{r^2}) + 2D(\frac{\partial^2 w}{\partial r^2} + \frac{2}{r}\frac{\partial w}{\partial r} - \frac{2w}{r^2}) - \frac{\eta}{k}\frac{\partial w}{\partial t}. \tag{A-2}$$

We are looking for a solution of equations (A-2) in the time-harmonic form

$$u = u(r)e^{-i\omega t}, \; w = w(r)e^{-i\omega t}. \tag{A-3}$$

By substituting expressions (A-3) into equations (A-2) we arrive at the following system of two equations:

$$H(\frac{\partial^2 u}{\partial r^2} + \frac{2}{r}\frac{\partial u}{\partial r} - \frac{2u}{r^2} + \frac{\omega^2 \rho_b u}{H}) + 2\alpha D(\frac{\partial^2 w}{\partial r^2} + \frac{2}{r}\frac{\partial w}{\partial r} - \frac{2w}{r^2} + \frac{\omega^2 \rho_f w}{2\alpha D}) = 0, \tag{A-4}$$

$$2\alpha(\frac{\partial^2 u}{\partial r^2} + \frac{2}{r}\frac{\partial u}{\partial r} - \frac{2u}{r^2} + \frac{\omega^2 \rho_f u}{2\alpha D}) + 2(\frac{\partial^2 w}{\partial r^2} + \frac{2}{r}\frac{\partial w}{\partial r} - \frac{2w}{r^2} + \frac{(\omega^2 mk + i\omega\eta)w}{2Dk}) = 0.$$

The general solution of equations (A-4) is:

$$u(r) = Aj_1(\lambda r) + \tilde{A}n_1(\lambda r),$$
$$w(r) = Bj_1(\lambda r) + \tilde{B}n_1(\lambda r); \tag{A-5}$$

where A, B, $\tilde{A}$, and $\tilde{B}$ are constants, and $j_1(Z)$ and $n_1(Z)$ are the spherical Bessel functions. These functions satisfy the following ordinary differential equation (Abramowitz and Stegun, 1964):

$$\frac{\partial^2 F(Z)}{\partial Z^2} + \frac{2}{Z}\frac{\partial F(Z)}{\partial Z} + (1 - \frac{2}{Z^2})F(Z) = 0.$$

It follows from the last equation that the function $F(\lambda r)$ satisfies the following equation:

$$\frac{\partial^2 F}{\partial r^2} + \frac{2}{r}\frac{\partial F}{\partial r} - \frac{2}{r^2}F = -\lambda^2 F \tag{A-6}$$

Next we substitute expressions (A-5) into equations (A-4) and use equation (A-6) to arrive at the following system of linear equations:

$$[AH(-\lambda^2 + \frac{\omega^2 \rho_b}{H}) + B2\alpha D(-\lambda^2 + \frac{\omega^2 \rho_f}{2\alpha D})]j_1(\lambda r) +$$

$$[\tilde{A}H(-\lambda^2 + \frac{\omega^2 \rho_b}{H}) + \tilde{B}2\alpha D(-\lambda^2 + \frac{\omega^2 \rho_f}{2\alpha D})]n_1(\lambda r) = 0,$$

$$[A\alpha(-\lambda^2 + \frac{\omega^2 \rho_f}{2\alpha D}) + B(-\lambda^2 + \frac{\omega^2 km + i\omega\eta}{2kD})]j_1(\lambda r) +$$

$$[\tilde{A}\alpha(-\lambda^2 + \frac{\omega^2 \rho_f}{2\alpha D}) + \tilde{B}(-\lambda^2 + \frac{\omega^2 km + i\omega\eta}{2kD})]n_1(\lambda r) = 0.$$

In order for a solution of these equations to exist, the coefficients in front of functions $n_1(Z)$ and $j_1(Z)$ must vanish:

$$[AH(-\lambda^2 + \frac{\omega^2 \rho_b}{H}) + B2\alpha D(-\lambda^2 + \frac{\omega^2 \rho_f}{2\alpha D})] = 0,$$

$$[A\alpha(-\lambda^2 + \frac{\omega^2 \rho_f}{2\alpha D}) + B(-\lambda^2 + \frac{\omega^2 km + i\omega\eta}{2kD})] = 0,$$

$$[\tilde{A}H(-\lambda^2 + \frac{\omega^2 \rho_b}{H}) + \tilde{B}2\alpha D(-\lambda^2 + \frac{\omega^2 \rho_f}{2\alpha D})] = 0,$$

$$[\tilde{A}\alpha(-\lambda^2 + \frac{\omega^2 \rho_f}{2\alpha D}) + \tilde{B}(-\lambda^2 + \frac{\omega^2 km + i\omega\eta}{2kD})] = 0.$$

(A-7)

Only two of the four equations (A-7) are linearly independent. By choosing the first two equations, solving them for A and B, and requiring that the determinant of this system vanish, we obtain:

$$H(-\lambda^2 + \frac{\omega^2 \rho_b}{H})(-\lambda^2 + \frac{\omega^2 km + i\omega\eta}{2kD}) - 2\alpha^2 D(-\lambda^2 + \frac{\omega^2 \rho_f}{2\alpha D})^2 = 0.$$

This equation, if solved for parameter λ, has four roots:

$$\lambda_1^2 = (-b + \sqrt{b^2 - 4ac})/2a, \quad \lambda_2^2 = (-b - \sqrt{b^2 - 4ac})/2a, \tag{A-8}$$

where

$$a = H - 2\alpha^2 D, \qquad b = -H(\frac{\omega^2 \rho_b}{H} + \frac{\omega^2 km + i\omega\eta}{2kD}) + 2\omega^2 \alpha \rho_f,$$

$$c = \omega^2 \rho_b (\frac{\omega^2 km + i\omega\eta}{2kD}) - \frac{\omega^4 \rho_f}{2D}.$$

Since functions $n_1(Z)$ and $j_1(Z)$ are odd, we need to use only two of four roots given by equation (A-8). Thus the general solution of equations (A-2) is

$$u(r) = A_1 j_1(\lambda_1 r) + \tilde{A}_1 n_1(\lambda_1 r) + A_2 j_1(\lambda_2 r) + \tilde{A}_2 n_1(\lambda_2 r),$$
$$w(r) = B_1 j_1(\lambda_1 r) + \tilde{B}_1 n_1(\lambda_1 r) + B_2 j_1(\lambda_2 r) + \tilde{B}_2 n_1(\lambda_2 r);$$

(A-9)

where A_1, $\tilde{A}_1$, A_2, $\tilde{A}_2$, B_1, $\tilde{B}_1$, B_2, and $\tilde{B}_2$ are constants. Only four of these eight constants are independent. Indeed, by substituting expressions (A-9) into equations (A-4) we find that

$$A_1 = -C_1 B_1, \; A_2 = -C_2 B_2, \; \tilde{A}_1 = -C_1 \tilde{B}_1, \; \tilde{A}_2 = -C_2 \tilde{B}_2,$$

where

$$C_1 = \frac{2\alpha D(-\lambda_1^2 + \frac{\omega^2 \rho_f}{2\alpha D})}{H(-\lambda_1^2 + \frac{\omega^2 \rho_b}{H})}, \quad C_2 = \frac{2\alpha D(-\lambda_2^2 + \frac{\omega^2 \rho_f}{2\alpha D})}{H(-\lambda_2^2 + \frac{\omega^2 \rho_b}{H})}.$$

Once the displacements are calculated, the radial stress component in the rock, σ, and the pore pressure, P_f, can be found as follows (Biot, 1962; and Dutta and Ode, 1979):

$$\sigma = H\frac{\partial u}{\partial r} + 2(K_d + 2\alpha^2 D - \frac{2G_d}{3})\frac{u}{r} + 2\alpha D(\frac{\partial w}{\partial r} + \frac{2w}{r}),$$
$$P_f = -2\alpha D(\frac{\partial u}{\partial r} + \frac{2u}{r}) - 2D(\frac{\partial w}{\partial r} + \frac{2w}{r}).$$

(A-10)

APPENDIX B

ALGORITHM FOR IMPLEMENTING THE INTEGRATED MODEL

a. Find displacements u and w from equations (A-9) with the appropriate boundary conditions.

b. Calculate σ and P_f from equation (A-10).

c. Calculate $\langle \partial P / \partial \sigma \rangle$ from equation (5).

d. Find K_m, K_{ms}, and G_m from equations (3) and (4) by using $\langle \partial P / \partial \sigma \rangle$ instead of $\partial P / \partial \sigma$.

e. Find corrected displacements u and w from equations (A-9) where

$$\lambda_1^2 = (-\bar{b} + \sqrt{\bar{b}^2 - 4\overline{ac}})/2\bar{a}, \lambda_2^2 = (-\bar{b} - \sqrt{\bar{b}^2 - 4\overline{ac}})/2\bar{a},$$

$$\bar{a} = \overline{H} - 2\overline{\alpha}^2\overline{D}, \quad \bar{b} = -\overline{H}(\frac{\omega^2\rho_b}{\overline{H}} + \frac{\omega^2 km + i\omega\eta}{2k\overline{D}}) + 2\omega^2\overline{\alpha}\rho_f,$$

$$\bar{c} = \omega^2\rho_b(\frac{\omega^2 km + i\omega\eta}{2k\overline{D}}) - \frac{\omega^4\rho_f}{2\overline{D}},$$

$$\overline{H} = \overline{K} + \frac{4}{3}G_m, \overline{D} = -\frac{\overline{K}}{2\overline{\alpha}}\left\langle\frac{dP}{d\sigma}\right\rangle, \overline{\alpha} = 1 - \frac{K_m}{K_{ms}},$$

$$\overline{K} = K_m / (1 + \overline{\alpha}\left\langle\frac{dP}{d\sigma}\right\rangle), G_m = \left[\frac{1}{G_d} - \frac{4}{15}(\frac{1}{K_d} - \frac{1}{K_{md}})\right],$$

$$\frac{1}{K_{md}} = \frac{1}{\tilde{K}_{ms}} + \frac{1}{K_{hp}} - \frac{1}{K_s}, \tilde{K}_{ms} = K_{msd} + \overline{\alpha}\left[1 - f(\xi)\right].$$

APPENDIX C

THE SINGLE-PATCH MODEL: MACROSCOPIC SQUIRT FLOW

The constants in equation (A-9) must be found from the zero-pressure boundary condition at the patch surface:

$$P_f = 0 \quad \text{at} \quad r = R. \tag{C-1}$$

we assume that the amplitude of the stress at $r = R$ is

$$\sigma = \sigma_0 \quad \text{at} \quad r = R. \tag{C-2}$$

The constants $\tilde{A}_1$, $\tilde{A}_2$, $\tilde{B}_1$, and $\tilde{B}_2$ in equation (2) should vanish since the function $n_1(Z)$ approaches infinity as its argument approaches zero. The stress and the fluid pressure in the sphere are related to displacements u and w through equations (A-10).

we use conditions (C-1) and (C-2) in equations (A-10) where u and w are expressed using equation (A-4). To find the derivative of the $j_1(z)$ function we use the following:

$$\frac{dj_1(z)}{dz} = \frac{j_1(z)}{z} - j_2(z).$$

Finally we arrive at the following equations for constants A_1 and A_2:

$$A_1 = \sigma_0 / \{(H + 2\lambda_E)[j_1(\lambda_1 R) - Tj_1(\lambda_2 R)] / R - H[\lambda_1 j_2(\lambda_1 R) - T\lambda_2 j_2(\lambda_2 R)]$$
$$+ 2\alpha D(-C_1[3j_1(\lambda_1 R) / R - \lambda_1 j_2(\lambda_1 R)] + TC_2[3j_1(\lambda_2 R) / R - \lambda_2 j_2(\lambda_2 R)]\},$$
$$A_2 = TA_1,$$

where
$$T = -\frac{(\alpha - C_1)}{(\alpha - C_2)} \frac{[3j_1(\lambda_1 R) / R - \lambda_1 j_2(\lambda_1 R)]}{3j_1(\lambda_2 R) / R - \lambda_2 j_2(\lambda_2 R)}.$$

APPENDIX D

TWO-DOMAIN PATCH MODEL

We assume that the inner sphere is dry and the outer shell is fully-saturated (Figure 6). The radii of the inner sphere and the outer shell are a and b, respectively. All parameters related to the inner sphere have subscripts "1", whereas all parameters related to the outer shell have subscripts "2".

The boundary conditions are (1) continuity of rock and fluid displacement at $r = a$:

$$u_1 = u_2, \quad w_1 = w_2, \quad \text{at} \quad r = a,$$

(2) continuity of stress and fluid pressure at $r = a$:

$$\sigma_1 = \sigma_2, \quad P_{f1} = P_{f2}, \quad \text{at} \quad r = a;$$

and (3) zero fluid flux across the shell boundary at $r = b$:

$$w_2 = 0 \quad \text{at} \quad r = b;$$

Also, we take the amplitude of the external stress as σ_0 at $r = b$:

$$\sigma_2(b) = \sigma_0.$$

The displacements in the inner sphere are:

$$u_1(r) = A_{11} j_1(\lambda_1 r) + A_{21} j_1(\lambda_2 r), \tag{D-1}$$

and the displacements in the outer shell are:

$$u_2(r) = A_{12} j_1(\lambda_1 r) + \tilde{A}_{12} n_1(\lambda_1 r) + A_{22} j_1(\lambda_2 r) + \tilde{A}_{22} n_1(\lambda_2 r). \tag{D-2}$$

Notice that in the inner sphere, constants $\tilde{A}_1$, $\tilde{A}_2$, $\tilde{B}_1$, and $\tilde{B}_2$ vanish (Appendix C).

We substitute equations (D-1) and (D-2) into the above six boundary conditions. As a result we obtain a linear system of six equations with six unknowns

$$\underline{\underline{A}}\,\underline{X} = \underline{F}, \tag{D-3}$$

where vectors $\underline{F}$ and $\underline{X}$ are:

$$\underline{F} = [0, 0, 0, 0, -\sigma_0, 0]^T, \quad \underline{X} = [A_{11}, A_{21}, A_{12}, \tilde{A}_{12}, A_{22}, \tilde{A}_{22}]^T;$$

System (D-3) must be solved for $\underline{X}$. After finding $\underline{X}$, we use equation (D-2) to calculate the displacement. Finally, the effective bulk modulus of the two-patch system is calculated from the following equation:

$$K_{eff} = \frac{-\sigma_0 b}{3u_2(b)}.$$

APPENDIX E

SOLUTION FOR BIOT EQUATIONS IN 1D MEDIUM.

In many cases, a one-dimensional solution is more important than a solution in spherical geometry (e.g. in the case of a normal incidence seismic wave). Therefore, we provide here the basis for the solution of Biot's equation in a 1-D medium (Figure 13).

Equation 1. Can be written in a Cartesian coordinate system with dependence only on the Z axis as follows:

$$\rho_b \frac{\partial^2 \vec{u}}{\partial t^2} + \rho_f \frac{\partial^2 \vec{w}}{\partial t^2} = H\nabla(\nabla \cdot \vec{u}) + 2\alpha D\nabla(\nabla \cdot \vec{w}),$$

$$\rho_f \frac{\partial^2 \vec{u}}{\partial t^2} + m \frac{\partial^2 \vec{w}}{\partial t^2} = 2\alpha D\nabla(\nabla \cdot \vec{u}) + 2D\nabla(\nabla \cdot \vec{w}) - \frac{\eta}{k}\frac{\partial \vec{w}}{\partial t}. \tag{E-1}$$

We are looking for a trial solution of the form:

$$u = u(z)e^{i\omega t},$$

$$w = w(z)e^{i\omega t}. \tag{E-2}$$

Thus equation E-1 can be written as follows:

$$\rho_b \frac{\partial^2 \vec{u}}{\partial t^2} + \rho_f \frac{\partial^2 \vec{w}}{\partial t^2} = H\nabla(\nabla \cdot \vec{u}) + 2\alpha D\nabla(\nabla \cdot \vec{w}),$$

$$\rho_f \frac{\partial^2 \vec{u}}{\partial t^2} + m \frac{\partial^2 \vec{w}}{\partial t^2} = 2\alpha D\nabla(\nabla \cdot \vec{u}) + 2D\nabla(\nabla \cdot \vec{w}) - \frac{\eta}{k}\frac{\partial \vec{w}}{\partial t}. \tag{E-3}$$

The general solution to equation E-2 is as follows:

$$u(z) = A_1 e^{-i\lambda z} + A_2 e^{i\lambda z},$$

$$w(z) = B_1 e^{-i\lambda z} + B_2 e^{i\lambda z}. \tag{E-4}$$

Substituting E-3 in E-2 and arranging terms we get the following coupled system of equations:

$$\left\{\left[\omega^2 \rho_b - \lambda^2 H\right]A_1 + \left[\omega^2 \rho_f - \lambda^2 2\alpha D\right]B_1\right\}e^{-i\lambda z} +$$

$$\left\{\left[\omega^2 \rho_b - \lambda^2 H\right]A_2 + \left[\omega^2 \rho_f - \lambda^2 2\alpha D\right]B_2\right\}e^{i\lambda z} = 0$$

$$\left\{\left[\omega^2 \rho_f - \lambda^2 2\alpha D\right]A_1 + \left[\omega^2 m - \lambda^2 2D - i\omega\frac{\eta}{k}\right]B_1\right\}e^{-i\lambda z} + \qquad\text{(E-5)}$$

$$\left\{\left[\omega^2 \rho_f - \lambda^2 2\alpha D\right]A_2 + \left[\omega^2 m - \lambda^2 2D - i\omega\frac{\eta}{k}\right]B_2\right\}e^{i\lambda z} = 0$$

The system G-4 will have a solution if

$$\left\{\left[\omega^2 \rho_b - \lambda^2 H\right]A_i + \left[\omega^2 \rho_f - \lambda^2 2\alpha D\right]B_i\right\} = 0,$$

$$\left\{\left[\omega^2 \rho_f - \lambda^2 2\alpha D\right]A_i + \left[\omega^2 m - \lambda^2 2D - i\omega\frac{\eta}{k}\right]B_i\right\} = 0, \quad i = 1,2 . \qquad\text{(E-6)}$$

To have a solution the determinant of system E-5 must vanish:

$$\left[\omega^2 \rho_b - \lambda^2 H\right]\left[\omega^2 m - \lambda^2 2D - i\omega\frac{\eta}{k}\right] - \left[\omega^2 \rho_f - \lambda^2 2\alpha D\right]^2 = 0 . \qquad\text{(E-7)}$$

Equation E-6 gives two roots for λ^2. Thus the general solution (E-4) is now:

$$u(z) = A_1 e^{-i\lambda_1 z} + A_2 e^{i\lambda_1 z} + \hat{A}_1 e^{-i\lambda_2 z} + \hat{A}_2 e^{-i\lambda_2 z},$$

$$w(z) = B_1 e^{-i\lambda_1 z} + B_2 e^{i\lambda_1 z} + \hat{B}_1 e^{-i\lambda_2 z} + \hat{B}_2 e^{-i\lambda_2 z} . \qquad\text{(E-8)}$$

Also, from G-6 there is a linear relation between A_i and B_i:

$$B_i = C_1 A_i, \quad \hat{B}_i = C_2 \hat{A}_i, \quad C_j = -\frac{\left[\omega^2 \rho_b - \lambda^2_{\ j} H\right]}{\left[\omega^2 \rho_f - \lambda^2_{\ j} 2\alpha D\right]}, \ j = 1,2 . \qquad\text{(E-9)}$$

The constants A_i and B_i can be determined from specific boundary conditions. For example, the equivalent solution for a single patch can be obtaned by using the folowing boundary conditions:

The constants in equation (E-4) have to be found from the zero-pressure boundary condition at the patch surface:

$$P_f = 0 \quad \text{at} \quad z = L,$$

$$w = 0 \quad \text{at} \quad z = 0. \qquad\text{(E-10)}$$

We assume that the amplitude of the stress at the boundaries is as follows:

$$\sigma = \sigma_0 \quad \text{at} \quad z = L,$$
$$\sigma = \sigma_0 \quad \text{at} \quad z = 0. \tag{E-11}$$

The relation between the pressure and the stress is given by (Biot, 1962):

$$\sigma(z) = (\lambda_c + 2\mu)\frac{\partial u(z)}{\partial z} + \alpha 2D\frac{\partial w(z)}{\partial z},$$

$$P_f(z) = -\alpha 2D\frac{\partial u(z)}{\partial z} - 2D\frac{\partial w(z)}{\partial z}. \tag{E-12}$$

Using E-4, and E-11 one can obtain a linear system of equation and solve for A_1, A_2, $\hat{A}_1$ and $\hat{A}_2$.

Z

Z=L

Z=0
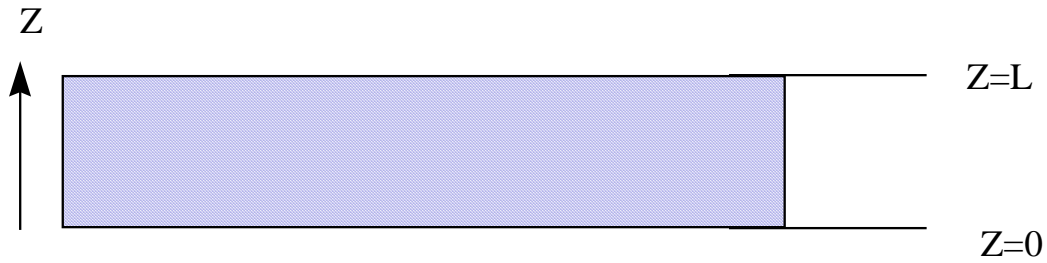
Figure 13, 1-D geometry for Biot's equation.

NOTATIONS

c_0	-- fluid acoustic velocity,
G	-- shear modulus dry rock;
G_m	-- shear modulus of modified frame;
K	-- bulk modulus of dry rock;
K_s	-- bulk modulus of the mineral phase;
K_r	-- bulk modulus of saturated rock;
K_{ms}	-- bulk modulus of modified solid;
K_{msd}	-- bulk modulus of dry modified solid;
K_m	-- bulk modulus of modified frame;
K_{hP}	-- bulk modulus of dry rock at high pressure;
K_f	-- pore fluid bulk modulus;
k	-- permeability of soft pore space;
P	-- pore pressure;
R	-- characteristic squirt-flow length;
μ	-- pore fluid viscosity;
σ	-- hydrostatic confining stress;
ρ	-- rock density;
ρ_f	-- pore fluid density;
ϕ	-- total porosity;
ϕ_{so}	-- soft porosity;
ϕ_{st}	-- stiff porosity;
ϕ_s	-- $\phi_{so} / (1 - \phi_{st})$.

CHAPTER 3

HIGH RESOLUTION SHALLOW SEISMIC EXPERIMENTS IN SAND:
1). WATER TABLE, FLUID-FLOW AND SATURATION

3.1   ABSTRACT

A high resolution, very shallow seismic reflection and refraction experiment was conducted to investigate the seismic response of ground water level changes in beach sand in situ. A fixed 10 meter long receiver array was used for repeated seismic profiling. Direct measurements of water level in a monitoring well and moisture content in the sand were taken as well. The water table in the well changed by about 1m in slightly delayed response to the nearby ocean tides. In contrast, inversion of the seismic data yielded a totally different picture. The reflection from the water table at high tide appeared at a later time than the reflection at low tide. This unexpected discrepancy can be reconciled using Gassmann's equation: a low velocity layer must exist between the near surface dry sand and the deeper and much faster fully saturated sand. This low velocity layer coincides with the newly saturated zone and is caused by a combination of the sand's high density (close to that of fully saturated sand), and its high compressibility (close to that of dry sand). This low velocity zone causes a velocity pull down for the high frequency reflections, and causes a high tide reflection to appear later in time than low tide reflection.

The calculated velocities in the dry layer show changes with time that correlate with sand dryness, as predicted by the temporal changes of the sand's density due to changing water/air ratio. The results show that near-surface velocities in sand are sensitive to partial saturation in the transition zone between dry and saturated sand. We were able to extract the saturation of the first layer and the depth to the water table from the seismic velocities. The high-resolution reflections monitored the flow

process that occurred in the sand during the tides, and provided a real-time image of the hydrological process.

3.2   INTRODUCTION

The use of geophysical methods in ground water studies is increasing as the water management problems society faces become more complicated. The water table is one of the hydrological features geophysicists are often asked to locate, and high-resolution seismics is thought to be one of the most promising methods for imaging the shallow subsurface. Seismic refraction and reflection methods have been used successfully for mapping water table in aquifers (Haeni, 1986). However, the water table is not a simple seismic boundary: it is defined by the phreatic surface as the point where the pore water pressure is equal to the atmospheric pressure, and its location may vary in a relatively short length of time. But the seismic response of the water table is not defined by the pore pressure directly. Rather, it is defined through the pore fluid properties (such as compressibility, density and viscosity) and the degree of saturation.

The effect of saturation and pore fluids on the seismic velocity is an old problem in rock physics, and a subject of many theoretical (Gassmann, 1951, Biot, 1956, 1962) and experimental (Nur and Simmons, 1969; Murphy, 1984; Cadoret, 1993) investigations.   The majority of the experimental results were derived under laboratory conditions, and there is a degree of uncertainty in upscaling the results to the field.

To better understand the relation between the hydrological water table and its seismic image, and the seismic response of the subsurface under different wetting and draining situations, we conducted a high-resolution shallow seismic survey on a sandy beach in Monterey Bay, California during Aug. 23-25, 1995.   Shallow reflection and refraction data were acquired every 20-30 min., while the water table in

the sand was changing due to the nearby ocean tide, monitored directly in a shallow well. In situ saturation measurements from the upper 30 cm the sand were taken as well.

This paper reviews the field results and basic theory used to model them. The high- resolution experiment provides a valuable link between laboratory data and field scale data. The results of this experiment demonstrate the effects of fluid substitution in situ as inferred from surface seismics. In this paper (paper 1), we show the results of the modeling of the seismic response in shallow, unconsolidated sand. The analysis of the velocities is presented in the following paper 'High resolution shallow seismic experiments in sand: 2). Velocities in shallow, unconsolidated sand' (to be referred as Paper 2.).

3.3 THEORY REVIEW: SEISMIC RESPONSE AND WATER TABLE HYDROLOGY.

3.3.1 Seismic response and pore fluids: Biot-Gassmann theory.

The seismic velocity in rock or sediment is a function of the effective elastic constants of the material

$$V_p = \sqrt{\frac{\overline{K} + \frac{4}{3}\overline{G}}{\overline{\rho}}}, \quad V_s = \sqrt{\frac{\overline{G}}{\overline{\rho}}} \qquad (1)$$

where $\overline{K}$ and $\overline{G}$ are the effective material bulk and shear moduli respectively, and $\overline{\rho}$ is its bulk density.

Theoretical and laboratory data have shown that seismic velocity is sensitive to the presence of fluid in the pore space. The general linear stress - strain relations for a

porous elastic solid with fluids were derived by Biot (1956; 1962). At its low frequency limit, Biot's theory relates saturated elastic constants to the material properties as given by Gassmann equation (1951)

$$\frac{K_{sat}}{K_0 - K_{sat}} = \frac{K_{dry}}{K_0 - K_{dry}} + \frac{K_{fl}}{\phi(K_0 - K_{fl})}, \quad G_{sat} = G_{dry} \tag{2}$$

where ϕ is the porosity, G_{dry} and K_{dry} are the dry framework shear and bulk modulus, K_0 is the mineral bulk modulus, K_{fl} is the pore fluid bulk modulus, G_{sat} and K_{sat} are the saturated effective bulk moduli. For partially saturated rocks at low frequencies the effective modulus of the pore fluid as the harmonic average of the air bulk modulus K_{air} and the water bulk modulus K_{water} :

$$\frac{1}{K_{fl}} = \frac{S_w}{K_{water}} + \frac{1 - S_w}{K_{air}} \tag{3}$$

where S_w is water saturation of the pore space.

The density of the material is:

$$\rho = \phi\left(S_w \rho_{water} + (1 - S_W)\rho_{air}\right) + (1 - \phi)\rho_0 \tag{4}$$

where ρ_{air} and ρ_{water} are the gas and the liquid densities respectively, and ρ_0 is the density of the mineral.

The validity of the Biot-Gassmann theory was verified in low-frequency laboratory tests (Murphy, 1984; Cadoret, 1993). Figure 1 shows the seismic velocity predicted by the Biot-Gassmann equation for a beach sand (with dry P-velocity of 200 m/sec and S-velocity of 100 m/sec) also at low frequency. In high-porosity

unconsolidated sand, the partially saturated sand has a lower velocity then the dry sand due to the density effect. Only at 100% saturation is the stiffness of the pore fluid high enough to increase the velocity.

a Velocity from Gassman's equation 0-100% saturation

b Velocity from Gassman's equation 0-99% saturation
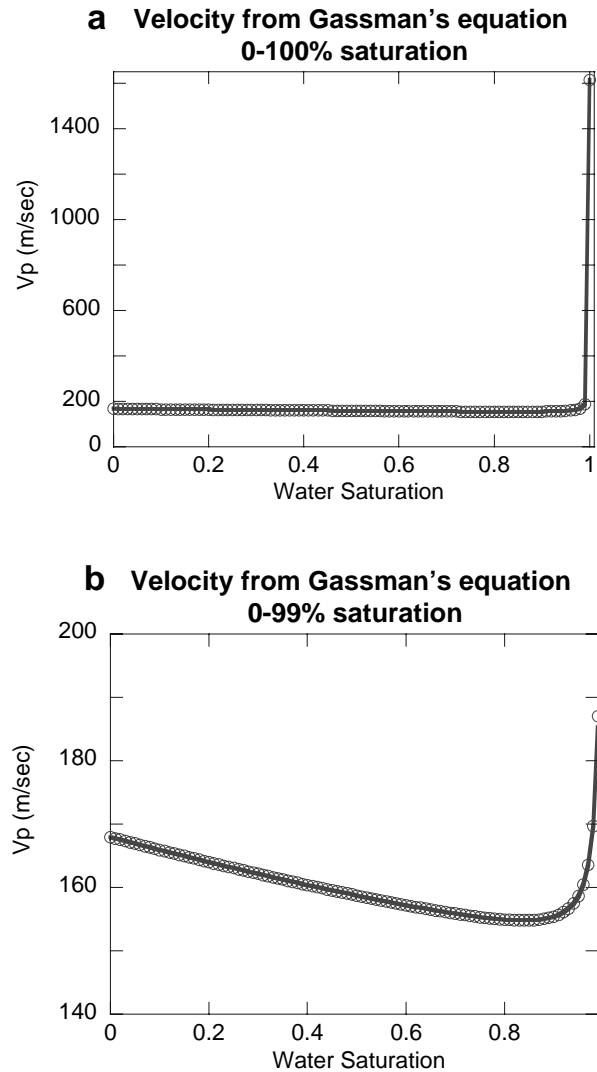
Figure 1: Velocity as a function of water saturation based on the Biot-Gassmann prediction for low velocity sand. (a), 0-100% saturation, (b). 0-99% saturation. The velocities are based on Moss Landing beach sand with dry P wave velocity of 167 m/sec, and dry S wave velocity of 100 m/sec.
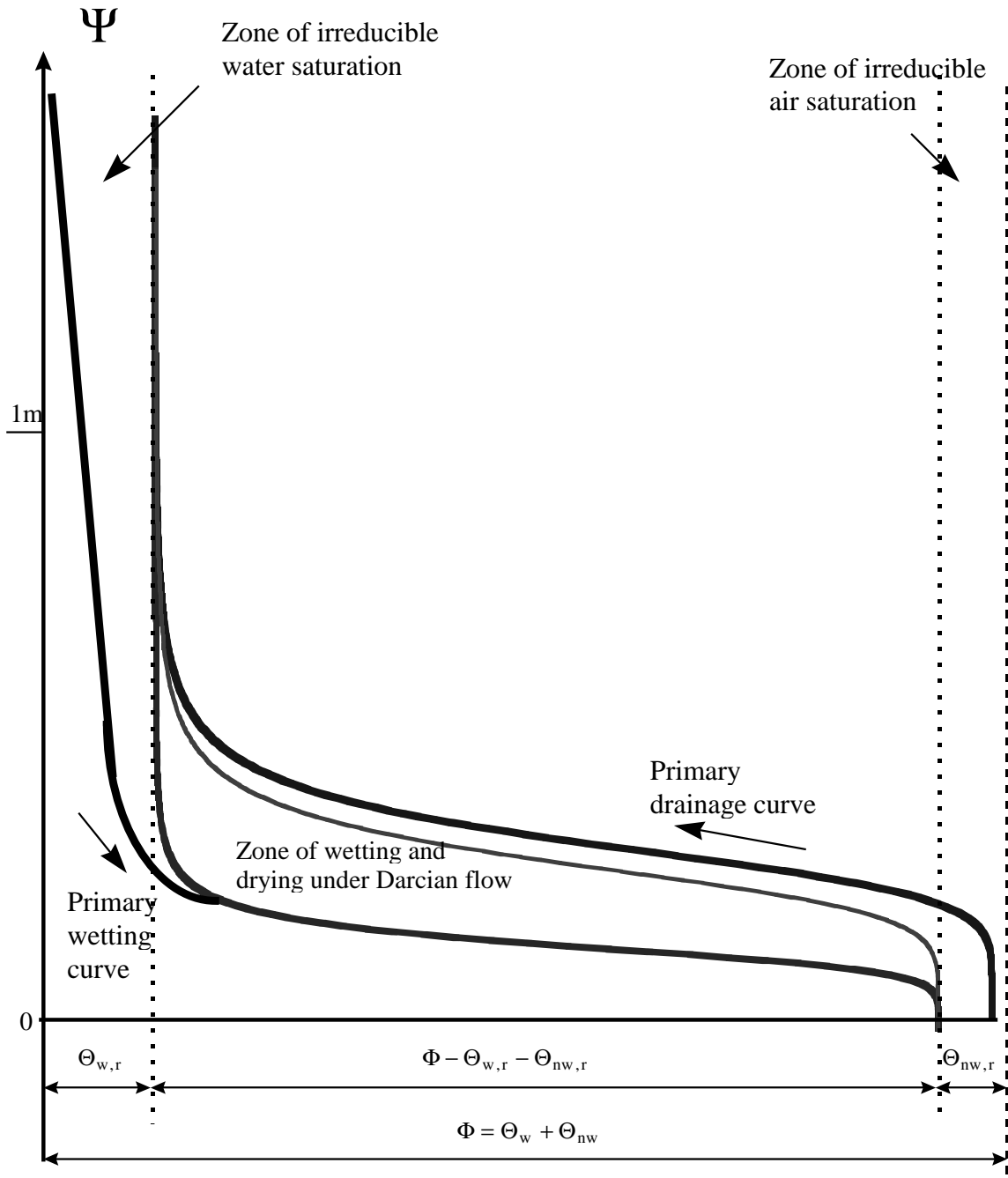
Figure 2:   Water pressure head (ψ) curve for different flow processes as a function of volumetric water content. Primary drainage is drainage from 100% saturation. Primary wetting is wetting from 0% saturation (totally dry sand). The main drainage and wetting curves correspond to repeated wetting and drying (such as in water table fluctuation). The residual air saturation $\theta_{nw,r}$, can still be present at pore pressure that are higher then the atmospheric pressure (for example below rising water table).

3.3.2 The hydrologic response of sand to wetting and draining

Shallow sand and soil in general, can be regarded as a combination of a solid phase (grains) and two fluid phases (water and air), with respective volumes $\theta_i = V_i / V$ $i = 1, 2, 3$ where V is the total volume and θ_i is the volumetric fraction of the phase i. The saturation is $S_i = \theta_i / \phi$ for i=1,2 (gas and liquid) where ϕ is the porosity.

Sand saturation and hydraulic permeability ($\mathbf{K_i}$) can be characterized by their volume phase content only on a macroscopic scale. It is also on this scale that Darcy's law is presumed to be valid.

However, on a grain or pore scale, immiscible phases become discontinuously distributed and bulk averaging is not appropriate.

On this scale, non-wetting fluid phase (air) becomes disconnected and immobile when its content θ_{nw} becomes less than some limiting value $\theta_{nw,r}$. and its relative hydraulic conductivity $\mathbf{K_{nw}} = 0$. In contrast, when the wetting fluid film is thin, the wetting fluid becomes immobile under bulk hydraulic gradients. Flow of the wetting fluid then becomes negligible compared to its advective diffusive transport as a dispersed phase in the non-wetting fluid. The wetting fluid becomes the immobile phase with $\mathbf{K_w} = 0$ when $\theta_w < \theta_{w,r}$.

The two residual fluid contents $\theta_{w,r}$ and $\theta_{nw,r}$ characterize the two transitions from coherent to incoherent fluid distributions. These two residual saturations are important parameters that affect fluid flow in the subsurface, specifically the drainage and wetting processes that occur in the beach sand.

At very low water saturation (when $\theta_w < \theta_{w,r}$), the volumetric water content of the wetting fluids can change mostly through evaporation and condensation (some have proposed a very slow film flow process to occur at this low saturation too). Otherwise ($\theta_w > \theta_{w,r}$), water is mobile as a connected phase, and its flow is governed

by Darcy's law. Similarly, when air content is low ($\theta_{nw} < \theta_{nw,r}$), its content can change only by dissolution or degassing. Otherwise ($\theta_{nw} > \theta_{nw,r}$),the air is mobile in a connected gaseous phase which is transported again by a Darcy-type law.

The two parameters $\theta_{w,r}$ and $\theta_{nw,r}$ are related by: $\theta_{w,r} \approx 2\theta_{nw,r}$ Luckner et al, 1989. Therefore for a beach sand with about 8% irreducible water saturation after drainage we expect about 4% of irreducible air saturation after imbibition. A schematic of the hysteretic fluid phase retention curve for the two-phase immiscible flow system is presented in figure 2. The primary wetting curve represents the process of water displacing air from totally dry sand. The primary drying curve represents similarly the process of air displacing water from totally saturated sand. The main wetting curve and main drying curve represent the phase distribution above the water table if the initial starting point was not of 100% saturation of air or water.

3.4   EXPERIMENTAL DESCRIPTION

3.4.1   Geologic setting and field techniques.

Our experimental site was at Moss-Landing beach in sandy Monterey Bay. The beach sand on there is coarse (0.22mm mean grain diameter), and its permeability is high (~4 Darcy, as measured by air permeameter in the lab). Our experiment was conducted during the period Aug. 23-25, 1995. During this time, the ocean tidal variation was about 1.65m. A monitoring well placed 1.5m from our geophone line, provided water table measurements every 30 min. The water table variation measured in the monitoring well was about 1m (Figure 4). A seismic line of 40 Hz geophones and a 48 channel 24 bit seismic acquisition system were placed on the beach sand parallel to the sea, @ 50 cm below high tide (figure 3). Measurements were taken until the tide covered the seismic line, and continued as soon as the water withdrew.

The seismic source was a 0.25 Kg hammer hitting a flat lying 5x5 cm steel plate. Geophone spacing was 0.2 m. We stacked 6-9 blows of the hammer on the plate at five different shot locations at 2 m, 0.5 m from first geophone, at the middle of the line, and 0.5m and 2m from the last geophone. One set of these shots took about 5-8 min. Each set of shots was analyzed as if it was taken at the same time, and the time difference between the seismic measurements represents the time difference between the beginning of each series.

The average water content in the upper 15 cm and 30 cm was determined with a Time Domain Reflectometer (TDR) taken every 20-30 min. throughout the experiment (fig. 4). The TDR provides the apparent dielectric constant (Ka), which is then converted to volumetric water content using the Top et al (1980) regression curve. Although salinity somewhat affects the apparent dielectric constant due to conductivity increase, using the Topp et al regression curve , yields error of less then 3% for the range of volumetric water content between 5% to 18% with conductivity of 1s/m (Dalton, 1992). In figure 4 each apparent dielectric constant and water point represent the spatial average of 3 measurements. Note that water content in the upper 15 cm is almost constant with time after the high tide, whereas the drainage of the sand is detected only in the 30 cm measurements. The reason is the high air humidity on the beach and the night fog on the beach.

The data presented here were collected between Aug. 24, 16:30pm local time and Aug. 25 2:50am. - a partial cycle of 10 hr from low tide to high tide and back. The measurements between 16:30-20:20 were done on a dry sand, and the measurements between 23:51-02:45 were conducted as the sand was drying, after the tide receded.

Figure 3: Tide at Moss-Landing beach. The seismic line was placed just below the high tide line, so at maximum tide the wave will wash the sand. The monitoring well (tube on the left) was placed 1.5m from the first geophone. The geophones were buried under the sand to reduce wave and wind noise. The geophone spacing was 20cm. At low tide the water table was 2m below the first geophone.

a

Depth to water table from monitoring well

b   **Apparent Dielectric Constant for 15cm and 30cm TDR wave guides**

c   **Averaged water content for 15cm and 30cm from Ka**
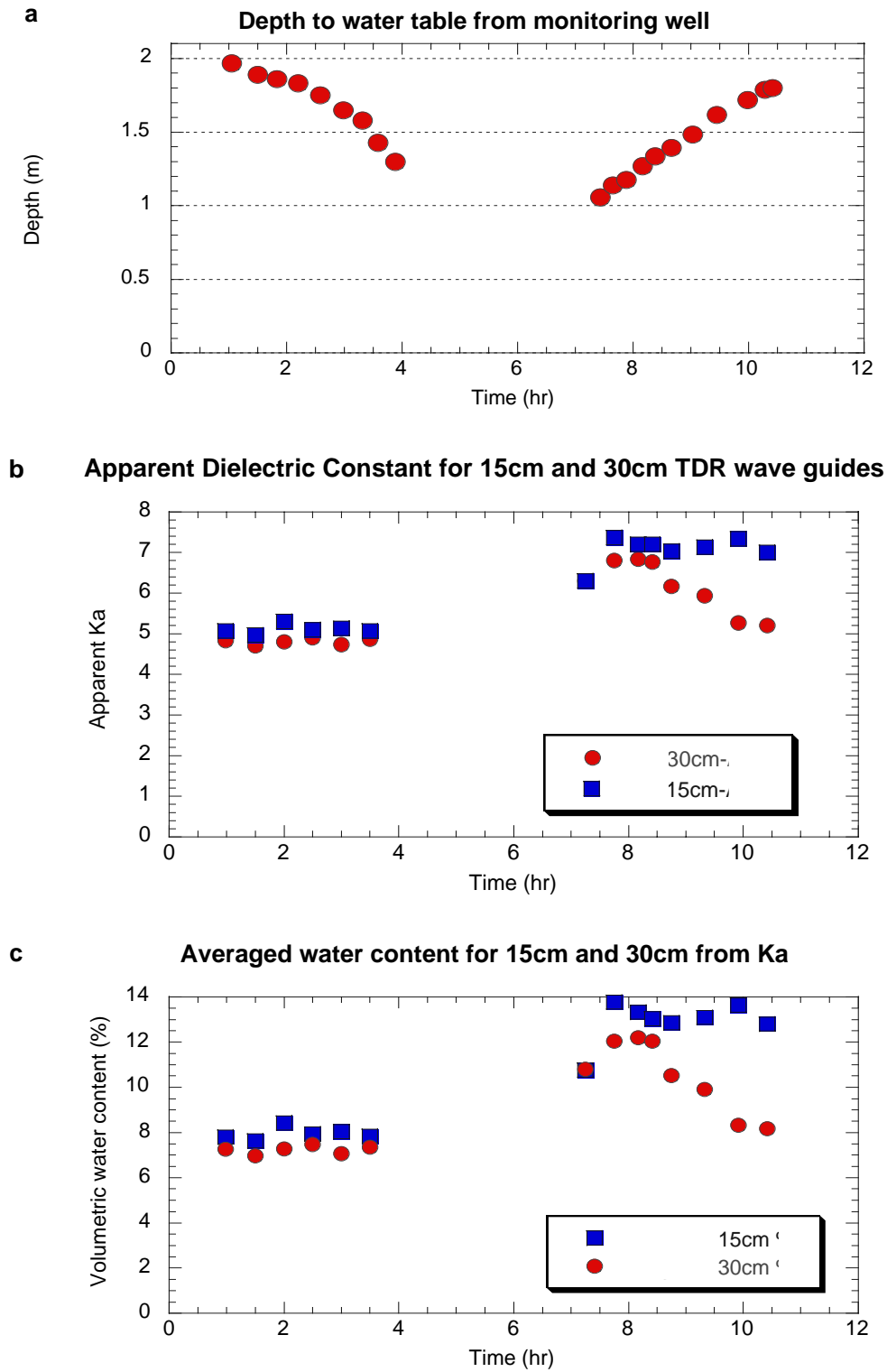
Figure 4:   (a).   Depth of the water table, as measured from the monitoring well in the time period between Aug. 24 16:30pm and Aug. 25 2:50am. t=0 is at 16:30.   (b).   Apparent dielectric constant in the first 15cm and 30cm, as measured by the TDR. (c). Average water content of the first 15cm and 30cm, as calculated from the dielectric constant.

3.4.2   Measurements Results

Both refraction and reflection data were collected and analyzed in this experiment. The refraction analysis was based on a two-layer model: a low velocity unsaturated sand overlying a high velocity fully saturated sand. We assumed a continuous velocity increase with depth (induced by the sand's overburden pressure), and calculated the apparent depth of the water table from the first arrivals (a detailed discussion of the velocity interpretation is given in paper 2, 'Velocities in unconsolidated sands'). The average velocity from the slope of the first arrivals was used to estimate the effect of the moisture content in the upper 30 cm (Figure 6). Figures 5a and 5b show shot records at low and high tide. The averaged velocity as calculated from the first arrivals was 159 m/sec to 167 m/sec when the sand was dry, and increased from 152 m/sec to 160 m/sec when the sand was wet. (Figure 6). The apparent depth to the water table as calculated from the refraction data alone is presented in figure 7.

The reflection from the shallow water table was masked by ground roll. A severe low cut filter was used to filter out the ground roll and image the reflection from the water table (Figure 5c). The NMO velocity was 240±5 m/sec for the shots between 16:30-20:20 local time.   The NMO velocity between 23:50-02:45 local time was 230±5 m/sec. Figure 9 presents the water table reflector image as a function of time after NMO correction, filtering and deconvolution. We present here the single fold data, which is actually the center split shots that were measured every 20-40 min during the tidal cycle.   The frequency content of the recorded signal contained energies above 800 Hz. The water table reflection in figure 5c is the reflection after low cut filtering of 800 Hz. Note that the ground roll in the reflection is spatially aliased but the water table reflection is quite strong. The frequency content of the filtered shot gather is presented in figure 10.

a). Low Tide Refraction
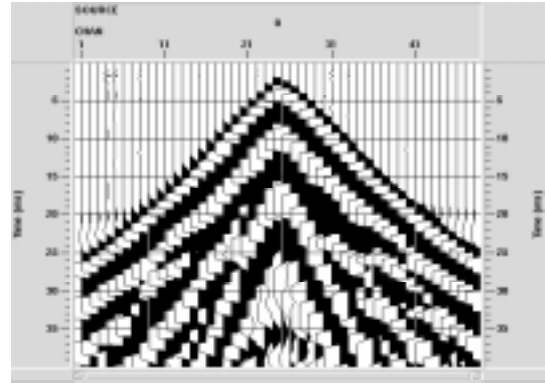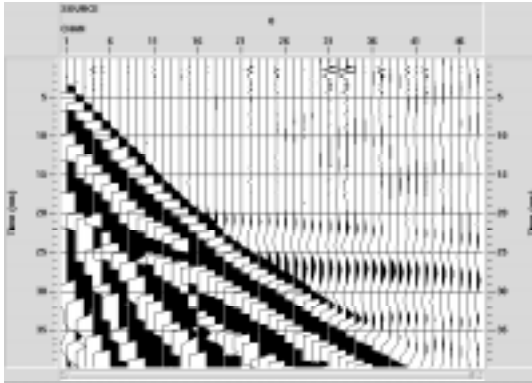
b). High Tide Refraction
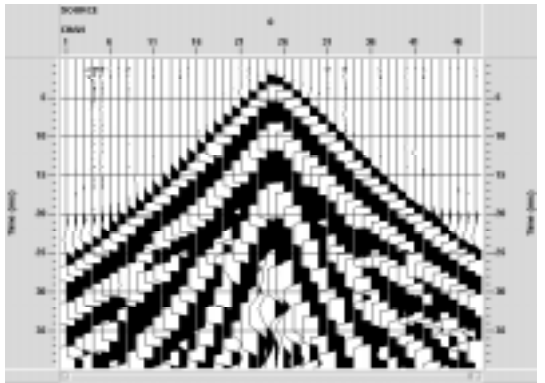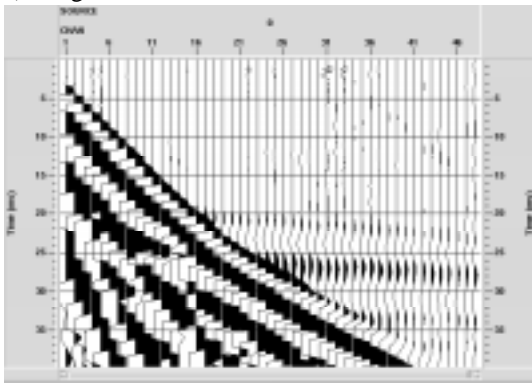
c). Reflection From water table after filtering
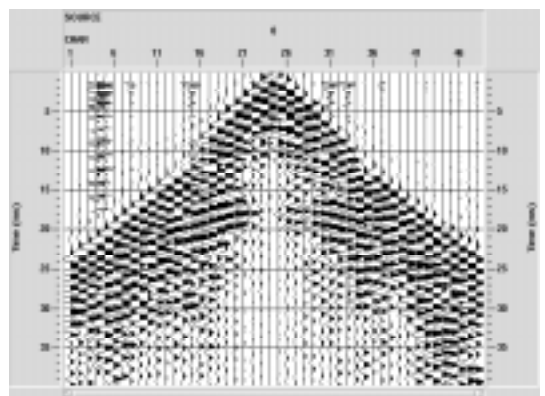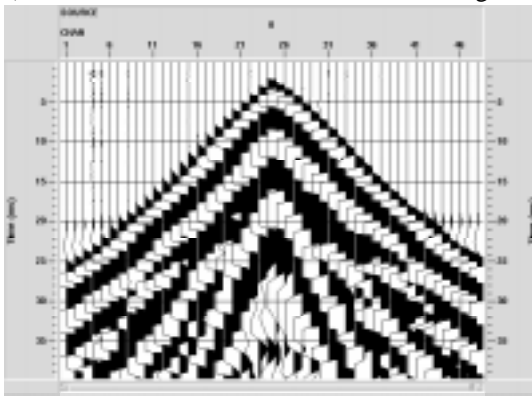
Figure 5: Refraction wave field recorded in the beach. First arrival and the water table refraction are clearly seen. (a). Low tide. (b). High Tide. (c). Shot gather before filtering (left), and after filtering (right). The reflection from the water table is the hyperbola in the middle of the sections

First Layer Average Velocity
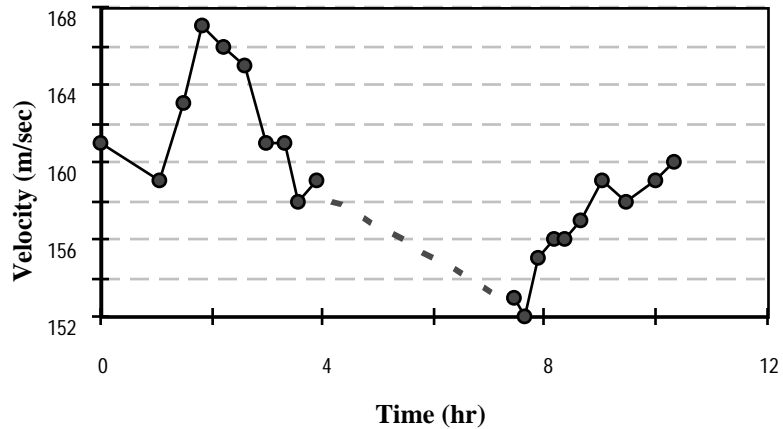
Figure 6: The first layer average velocity from the refraction data vs time. The velocity here was calculated by linear regression to the first layer velocities (circles). This velocity reflects the near surface conditions.

Depth to Seismic Refractor

(refraction interpretation with corrected velocity)
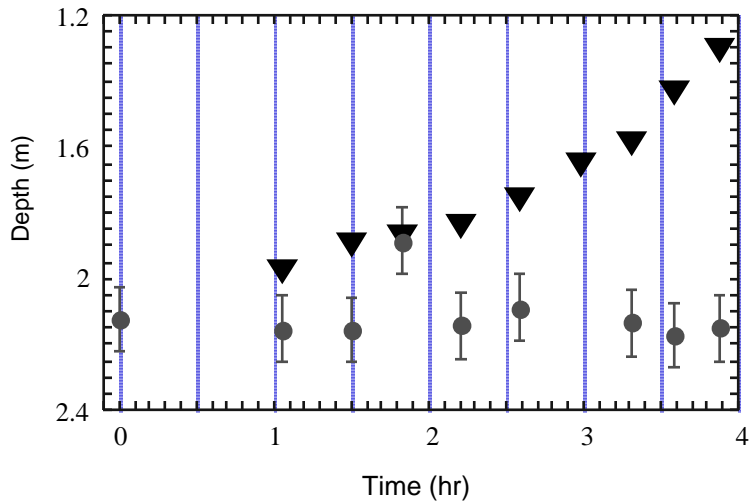
Figure 7: Seismic derived depth to the water table between Low tide and high tide (starting @ 16:30pm). The depth are calculated assuming a model with continuos velocity in the first layer. The triangles are the direct water table measurements from the monitoring well. (details on the velocity model used for the refraction interpretation are given in paper 2 (Bachrach et al), Velocities in Shallow unconsolidated sand)

3.5   DISCUSSION

3.5.1   Water table and Saturation

While the water table in the monitoring well rose and fell by about one meter, the seismic refractor remained essentially unchanged with time at the same depth of 2.15m ±0.1m below the geophone array. This was the actual depth of the water table at low tide (Figure 7). The high frequency reflection image of the water table at high tide was later (deeper) in time than the water table reflection at low tide (Figure 9). This seemingly wrong pattern can be simply explained however if we consider the low velocity caused by the density of less then fully saturated sand, as predicted by Gassman's equation.

The effect of the saturation on the velocity is clearly seen as the first layer velocity decreases after high tide and increases slowly as the sand drains (figure 6).

The averaged velocity of the first arrivals can be used to calculate the average saturation of the upper layer from the P-wave velocity using the fluid substitution equation of Mavko et al. (1995)

$$\frac{M_{ps}}{M_0 - M_{ps}} = \frac{M_{dry}}{M_0 - M_{dry}} + \frac{M_{fluid}}{\phi(M_0 - M_{fluid})} \tag{5}$$

$$V_{ps} = \sqrt{\frac{M_{ps}}{\rho_{eff}}} \tag{6}$$

where M_{fluid}, M_{dry}, M_{ps} are the elastic P-wave modulus ($M = \rho V_p^2$) of the fluid and dry and partially saturated sand respectively, and M_0 is the mineral (quartz in this case) modulus. Since the pore fluid stiffness doesn't change much with saturation for $S_w < 0.9$ we assume $M_{ps} \approx$ const. This assumption is based on the

fact that $M_{ps} = K_{ps} + \dfrac{4}{3} G_{ps}$, and according to Biot-Gassman's theory the partially saturated shear modulus, G_{ps}, is constant and the partially saturated bulk modulus, K_{ps}, is almost constant for saturation less then 99%. For $M_{ps} \approx \rho V_p^2 \approx$ const. the density variation can be extracted from the velocity. If the residual water saturation at dry conditions can be estimated and averaged density ρ_1 can be calculated, then the density change (due to saturation change) $\Delta\rho$ can be extracted using:

$$\rho_1 V_{p1}^2 \approx (\rho_1 + \Delta\rho) V_{p2}^2 \qquad\qquad (7)$$

where ρ_1 and V_{p1} are the density and the velocity of the unsaturated sand and V_{p2} is the velocity of the saturated sand. Figure 8 presents the saturation inferred from near surface velocity from first arrivals, using equations (7), and the saturation derived from the TDR measurements at 30 cm. Note that the saturation derived from the velocity data is somewhat lower then the TDR results for t=0-4hrs, and that the saturation from the velocity data is higher than the TDR results at the second part (t=7-11hr). Because velocity increases with depth (Paper 2), the ray path is curved, and the seismic wave actually samples deeper parts of the sand. Therefore, in the first part of the experiment, between 16:30 and 20:00 hours, the velocities infer slightly dryer sand below the near surface sand (which is probably affected by the humidity in the beach). In the second part (7-11hr) the velocity indicates that the sand is more saturated than the upper 30 cm. The effect of density is clear in the NMO velocity as well. We observe NMO velocity change of ~10 m/sec between the low tide dry sand @ 18:00 hr and the high @ .00:02hr local time (figure 11). By using equation (7), and the fact that the NMO velocity is RMS velocity for a layered medium with small spread approximation, (Yilmaz, 1987), it can be easily shown that $\dfrac{V_{nmo1}^2}{V_{nmo2}^2} \approx 1 + \dfrac{\overline{\Delta\rho}}{\overline{\rho_1}}$

where $\overline{\Delta\rho}$ is an averaged density change integrated along a verical column of sand.

If we take $V_{nmo1} = 240 m / sec$ and $V_{nmo2} = 230 m / sec$ then $\dfrac{\overline{\Delta \rho}}{\overline{\rho_1}} \approx 0.089$, which

gives an integrated saturation change of about 35%.

3.6 SUMMARY AND CONCLUSIONS

We show that (a). shallow water table reflections can be imaged from depths of ~2m, (b). the reflections do not correspond to the water table as defined by the phreatic surface, but that both the reflections and refractions are influenced by partial saturation and therefore are sensitive to the history of the flow. (c). The wave velocity in porous sand can be directly inverted into saturation. These results together are important for the use of shallow seismic for hydraulic monitoring. For example, if we wish to monitor water table changes during pumping, the seismic response will be controlled by the saturation profile and not the water table itself. These is in agreement with results of a high-resolution seismic monitoring of water table during pumping test done by Birkelo et al (1987). Their seismic image of the water table corresponded to a perched water table system and to the top of the saturation zone, rather than the water table itself. Our results imply also that when monitoring water table recovery after pumping, the reflection will not follow the phreatic surface.

The ability to image saturation can serve as an important tool for locating heterogeneity in the subsurface. We were able to calculate the pore water content as a function of time. This calculation can be used in calibration of the transport properties in the subsurface.

3.7 ACKNOWLEDGMENTS

Barbara Mavko for keeping our spirits high and to anonymous reviewers for valuable comments.
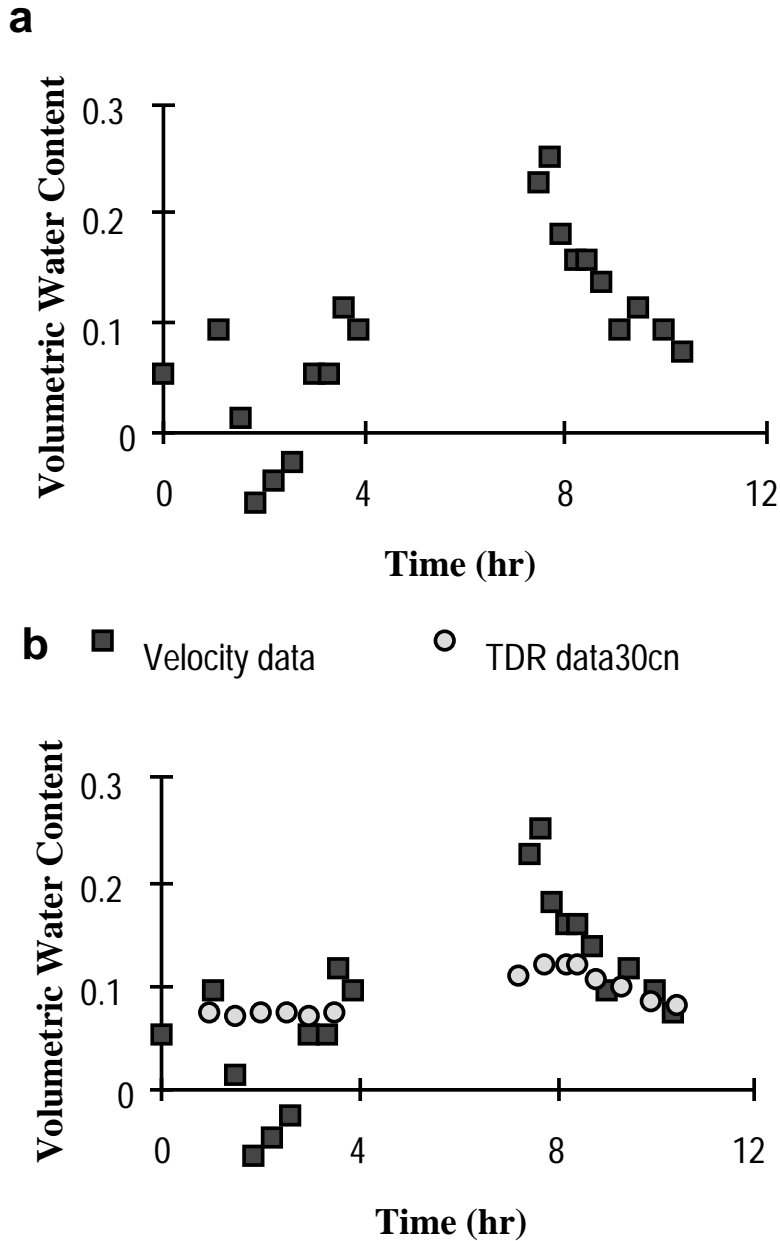
Figure 8:   (a) Volumetric water content in the first layer as calculated from the first layer velocity (direct arrivals) (b) Volumetric water content in the first layer as calculated from the first layer refraction together with the measurements from the TDR for the saturation at a depth of 30cm. The velocity indicate higher saturation than the one measured at the first 30cm. This is expected considering the fact that the seismic wave penetrated deeper then 30cm, and the water table is expected to be high especially after the high tide (t=7-8hr)
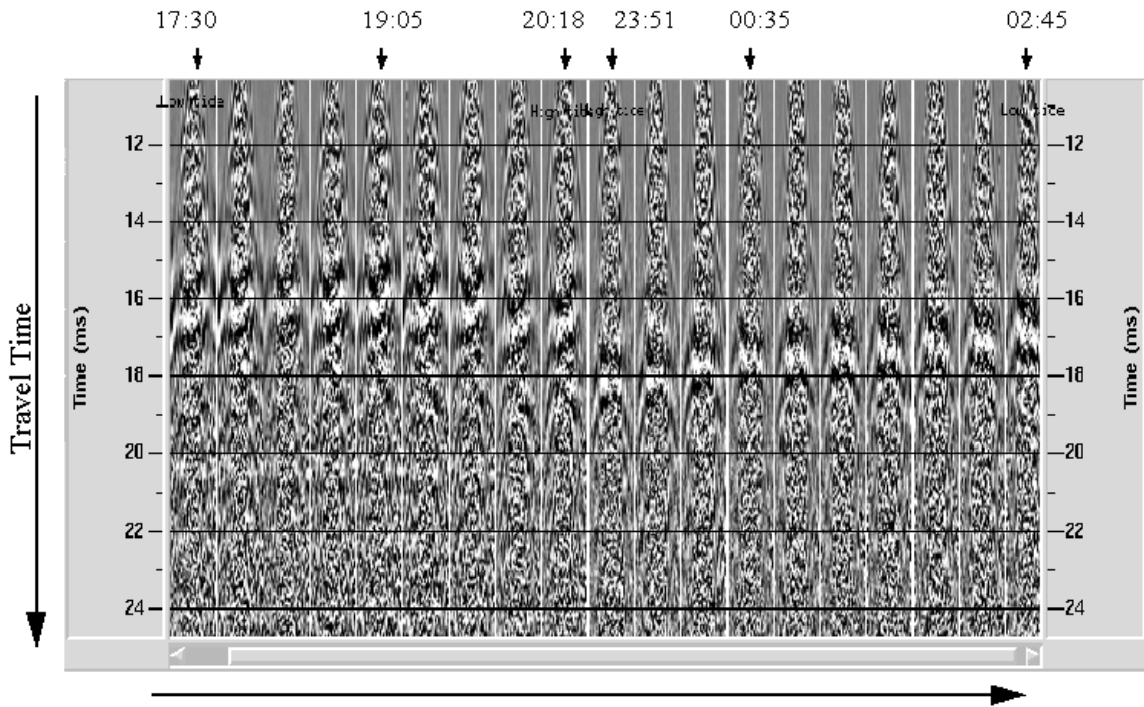
Monitoring Time

Figure 9: Water table reflector image. The left image is the reflection at low tide (@17:33pm). As time goes on the water table reflection appears later. The last image before the wave washed the line (@20:20pm) is the ninth from the left. After the beach was washed the velocity pull down is clearly visible. At maximum tide (tenth image from the left @ 23:50pm) the water table appears 1ms later then at low tide (first image to the right @ 2:45am).
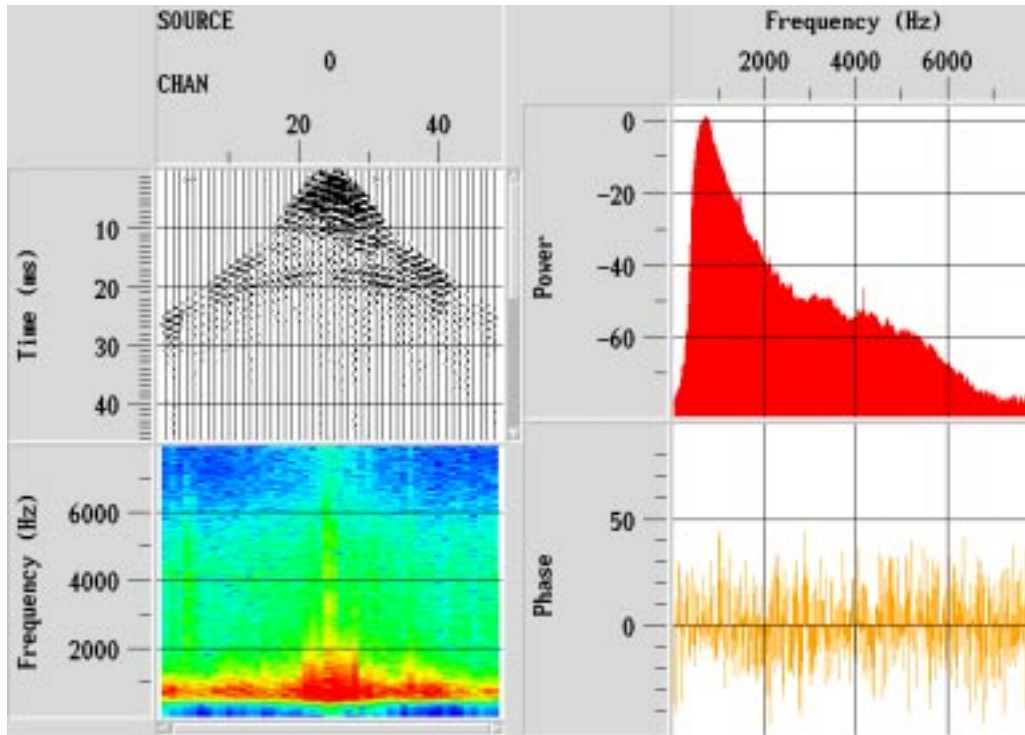
Figure 10:   Frequency content of a reflection shot gather. The shot was filtered with zero phase filter of 400-800-20000-40000 Hz.
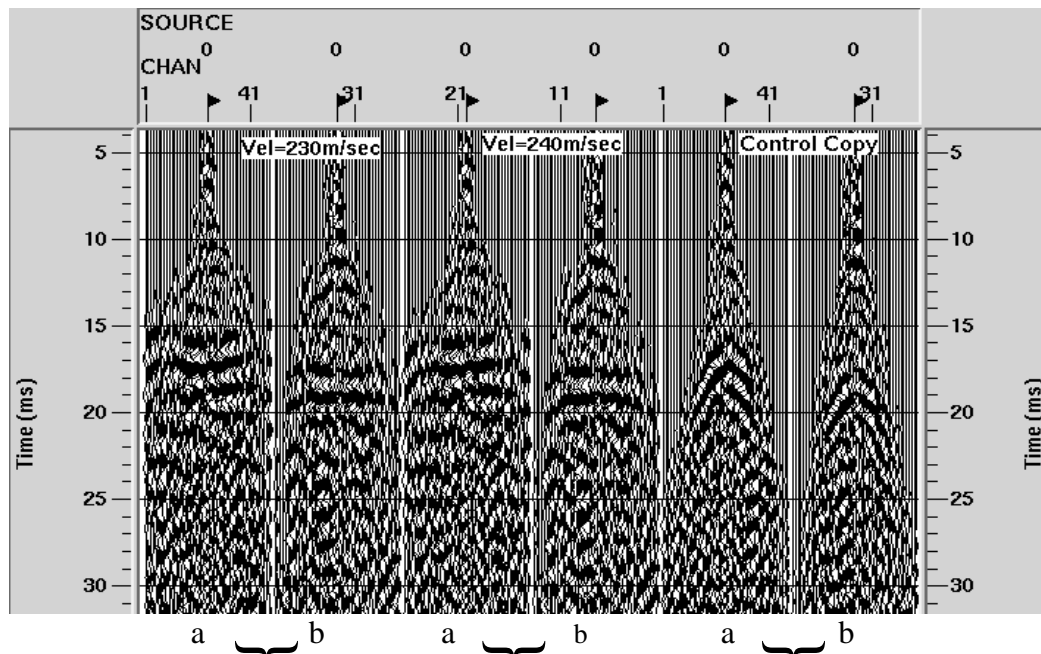
Figure 11:   NMO velocity change due to water content change: Reflector (a) is the water table reflection @ 18:00hr local time, and reflector (b) is the water table reflection at 00:02hr local time. Left: reflections corrected with NMO velocity of 230 m/sec. Middle: reflection corrected with NMO velocity of 240. Right: Control panel. Reflections are filtered with 800Hz low cut filter. Note that the @ high tide the NMO velocity is lower by 10 m/sec, which is observed on top of the velocity pull-down.

3.8   REFERENCES

Biot, M. A., 1956, Theory of propagation of elastic waves in fluid saturated porous solid. I low frequency range, II. Higher frequency range, J. Acoust. Soc. Am., **28**, 168-191.

Biot, M. A., 1962, Mechanics of deformation and acoustic propagation in porous media, J. Apll. Phys., **33**, 1482-1498.

Birkelo, B. A., Steeples, D. W., Miller, R., D., Sophocleous, M. A., 1987, Seismic reflection study of a shallow aquifer during a pumping test.,Ground Water, **25**, 703-709.

Cadoret, T., 1993, Effect de la saturation eau/gaz sur le proprietes acoustiques des roches, Ph.D thesis, University of Paris.

Dalton, F. N., 1992, Development of Time Domain Reflectometry for measuring soil water content and bulk soil conductivity, in Advances in measurements of soil physical properties: Bringing theory into practice., SSSA Special Publication ; **30**, 143-167.

Gardner, W. R., 1960, Soil water relation in arid and semi arid conditions, UNESCO, **15,** 37-61.

Gassmann, F., 1951, Uber die elastizitat poroser median, Vier. der natur Gesellschaft, **96,** 1-23.

Haeni, F., P., Grantham, D., G., and Ellefsen, K., 1987, Microcomputer-based version of SIPT-A program for the interpretation of seismic-refraction data, U. S. Geological Survey Open File reports: **87-103-A**.

Haeni, F. P., 1986, Application of seismic-refraction techniques to hydrologic studies. U. S. Geological Survey Open File reports: **84-0746**.

Jakosky,, J., J., 1940, Exploration geophysics, California: Trija Pub.

Luckner, L., Van Genuchten, M., T., & Nieslen, A., 1989, A consistent set of parametric models for the flow of two immiscible fluids in the subsurface, Water Res. research, **25**, 2187-2193.

Mavko, G., Chan, C., Mukerji, T., 1995, Fluid substitution; estimating change in Vp without knowing Vs., Geophysics, **60**, 1750-1755.

Murphy,W. F., III., 1984, Acoustic measures of partial gas saturation in tight sandstones. J.G.R, **89**, 549-559.

Nur, A. and Simmons, G., 1969, The effect of saturation on velocity in low porosity rocks, Earth Plan. Sci. Lett., **7**, 183-193.

CHAPTER 4

HIGH RESOLUTION SHALLOW SEISMIC EXPERIMENTS IN SAND: 2). VELOCITIES IN SHALLOW UNCONSOLIDATED SAND

4.1 ABSTRACT

We conducted a shallow high-resolution seismic reflection and refraction experiment on a sandy beach. The depth of investigation was about 2 m. We interpret the data using the Hertz-Mindlin contact theory combined with Gassmann's equation. These were used to obtain the vertical velocity profile. Then the profile was computed from seismic data using the turning-rays approximation. The NMO velocity at the depth of 2 m matches the velocity profile. As a result, we developed a method to invert measured velocity from first arrivals, i.e., velocity vs. distance into velocity vs. depth using only one adjustable parameter. This parameter contains all the information about the internal structure and elasticity of the sand. The lowest velocity observed was about 40 m/s. It is noteworthy that the theoretical lower bound for velocity in dry sand with air is as low as 13 m/s. We find that modeling sand as a quartz sphere pack does not quantitatively agree with the measured data. However, the theoretical functional form proves to be useful for the inversion.

4.2 INTRODUCTION

The measurement of velocity in unconsolidated materials is very difficult. In the laboratory, it is difficult to prepare samples from unconsolidated material without disturbing the material itself. Ultrasonic measurements in sand, for example, are very sensitive to the packing of the grains, and usually only high-pressure data are available. However, in many cases low pressure velocities are important, especially in near-surface problems, including static corrections. A shallow seismic experiment

can provide information concerning the velocity profile at very low effective pressures in the natural environment.

While analyzing the data from a shallow seismic experiment conducted on a sandy beach 'High resolution shallow seismic experiments in sand: 1). Water table, fluid flow and saturation', which will be referred as paper 1, several fundamental questions arose from the velocity measurements and the seismic interpretation, such as:

1) How slow can velocity in sand be?

2) What is the relation between the overburden (effective stress) and the seismic velocity?

3) What is the best way to relate shallow refraction data (first-layer velocity from refraction measurements) to the velocity as calculated from the reflections?

4) How well will the ray theory approximation work if the velocity gradient is very high?

In this paper we address these fundamental questions. The study is based on the Moss Landing beach experiment described in detail in Paper 1.

4.3   VELOCITIES IN UNCONSOLIDATED SAND

Figure 1 presents seismic shot gather that was collected on the Moss Landing beach on Aug 24, 1995 at 17:33 PM. Figure 2 shows the walls of a nearby pit. The water table at this time was at the depth of 1.97±0.02 m below the seismic line. In Figure 1 the first arrivals slope (calculated by a linear regression) corresponds to an average velocity of 160±10 m/s. The high velocity layers slope (at ~20 ms) is interpreted to be the water table refraction, with an average velocity of 2200±200 m/s. Figure 3 shows the average velocity of the first and second layers as calculated by regular refraction analysis program (SIPT1 of Haeni et al., 1987). By converting the seismic refraction into depth based on the above velocities (a two-layer model), we found the depth of the water table to be 1.4±0.15 m (Figure 4). This value <u>does not</u> match the measured depth of 1.97 m.
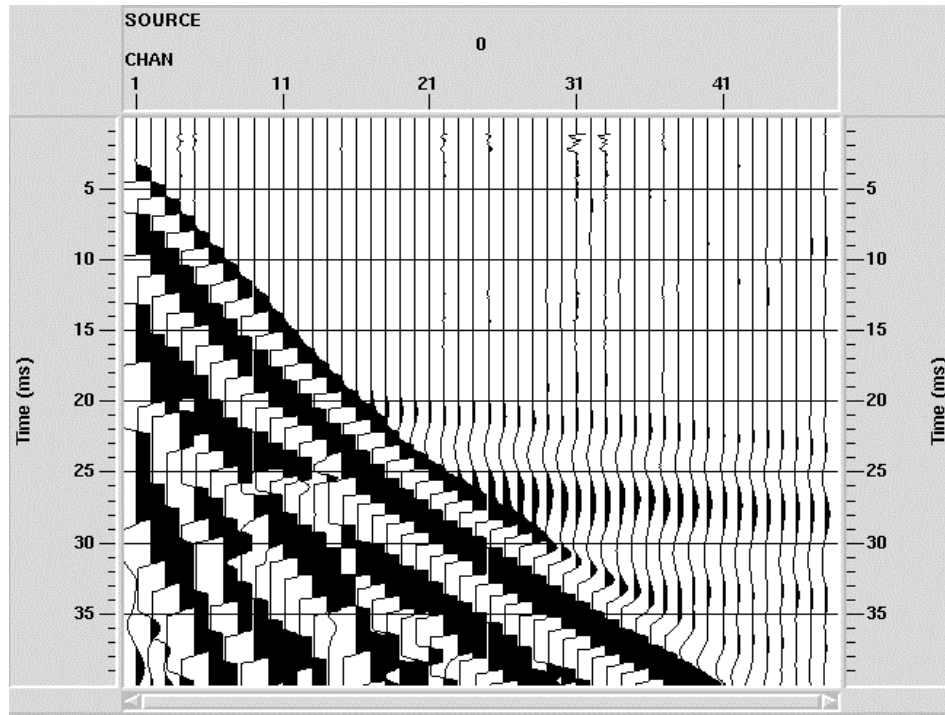
Figure 1: Shot gather from Moss Landing beach collected at Aug. 16, 1995, 17:33pm. The slope of the first layer is 159 m/sec.
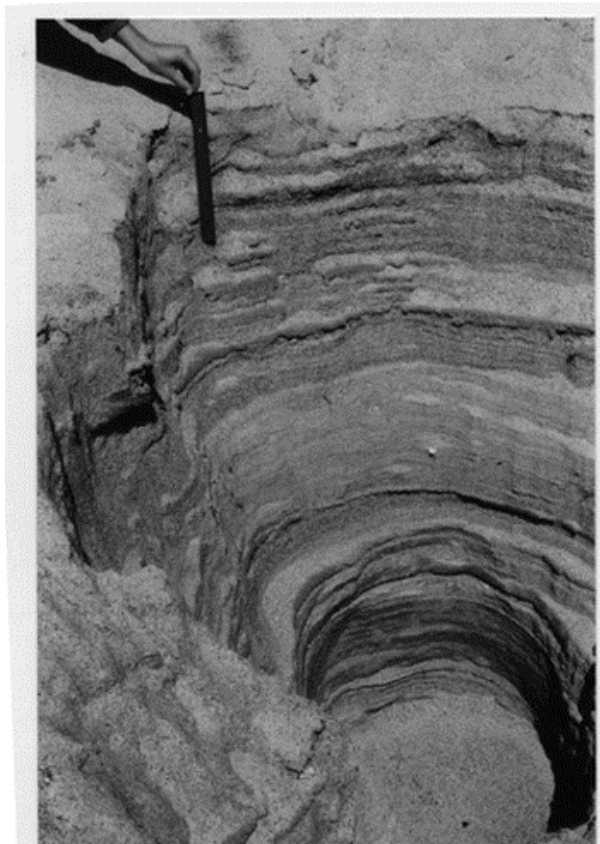
Figure 2: The sand profile in Moss Landing beach, from a pit to the depth of 2m.

First layer Velocity

second layer Avg. Velocity
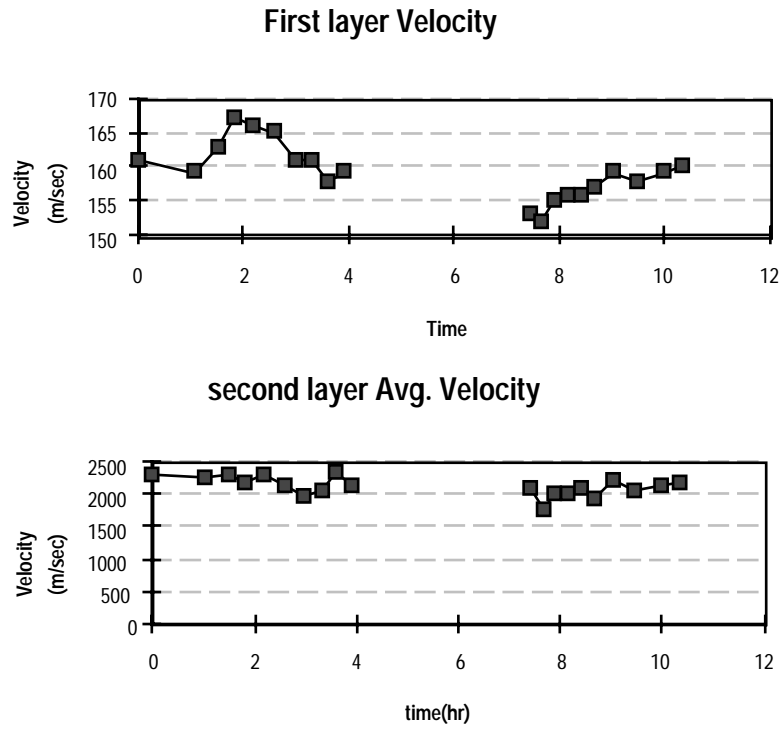
Figure 3:   First and second layer average velocities as calculated by regular refraction interpretation software, SIPT1 (Haeni et al, 1987)

**Depth to Seismic Refractor
(regular interpretation)**
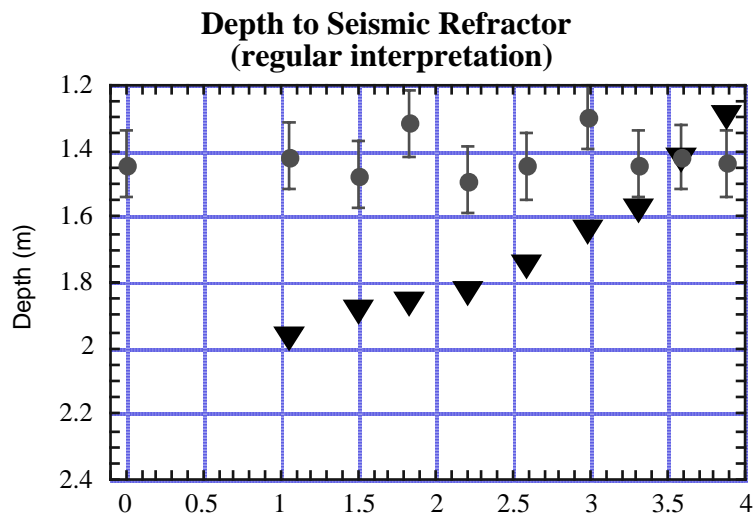
Figure 4:   Depth of the water table from the regular refraction interpretation (circles with error bars), and as measured from the monitoring well (triangles). Time is zero at 4:30 PM.

The fact that there is no physical reflector at the depth of 1.415 m, and that the high-resolution survey should have been able to detect depth with accuracy of at least 0.2 m, reveals some of the problems that are associated with assigning velocities to unconsolidated sand. Therefore, a more careful approach must be used when interpreting this kind of seismic data.

The seismic profile interpretation was conducted as the water table rose, and was compared with the water table depth, as measured in the monitoring well (Figure 4). A discussion of the effects of the transient water table on the seismic image is given in paper 1. Careful examination of the travel-time curve shows that the velocity of the first layer varies with the position of the receiver. The velocity, derived by dividing the distance between the shot and the receiver by the corresponding travel time, increases with the increasing distance between the shot and the geophone. The fact that the first layer velocity is much smaller than the second layer velocity makes the travel time curve seem almost linear (Figure 1). However, plotting the velocity as a function of distance shows nonlinear (Figure 5). We note here that the minimum measured velocity was 50±10 m/s, for a distance of 0.1 m between the shot and the receiver.

4.4 LOW VELOCITY BOUND FOR UNCONSOLIDATED SAND

The very top few centimeters of the beach sand can be viewed as a suspension of sand in air. The porosity of this suspension is the critical porosity of @40 % (Paper 1), where the grains barely touch each other. Therefore, a low velocity bound for sand can be calculated as the velocity in a suspension of sand in air. Taking the air bulk moduli K_{air} at 0.1 Mpa (1 bar), and assuming that sand grains are quartz with the bulk modulus K_{quartz} of 36.6 GPa and the shear modulus G_{quartz} of 45 Gpa, the effective elastic modulus of the mixture is the Reuss average of the phases:

$$\frac{1}{M_{eff}} = \frac{\phi}{M_{air}} + \frac{1-\phi}{M_{quartz}}, \tag{1}$$

where $M = K + \frac{4}{3}G$ and ϕ is the porosity of the mixture. Then the velocity is:

$$V_p = \sqrt{\frac{M_{eff}}{\rho_{eff}}} \quad \rho_{eff} = (1-\phi)\rho_q + \phi\rho_{air} \tag{2}$$

where ρ_q is the quartz density and ρ_{air} is the air density. This gives a lower bound for the velocity in sand at ~ 13 m/sec. This minimum value is lower than the lowest velocity measured in the experiment (~ 50 m/sec, Figure 5).

4.5   VELOCITY VARIATION WITH DEPTH

The fact that the measured velocity increases with the distance between the shot and the receiver means that the velocity increases with depth (in agreement with the Fermat principle, the waves travel to minimize the travel time).

Because the porosity in our beach measured at about 40%±5%, (as inferred by volumetric water content at full saturation) does not noticeably change within depth, the observed velocity increase with depth is governed by increasing the overburden pressure.

4.5.1   Using the Hertz-Mindlin Theory for Velocity Interpretation

The contact Hertz-Mindlin theory (Mindlin, 1949) gives the following relations between the effective bulk and shear moduli and the pressure for the dry, dense, random pack of identical spherical grains subject to hydrostatic pressure P (Dvorkin and Nur, 1995):

Vp(x) @ 17:30-18:00pm.

Vp(X) @ 20:00-20:20pm
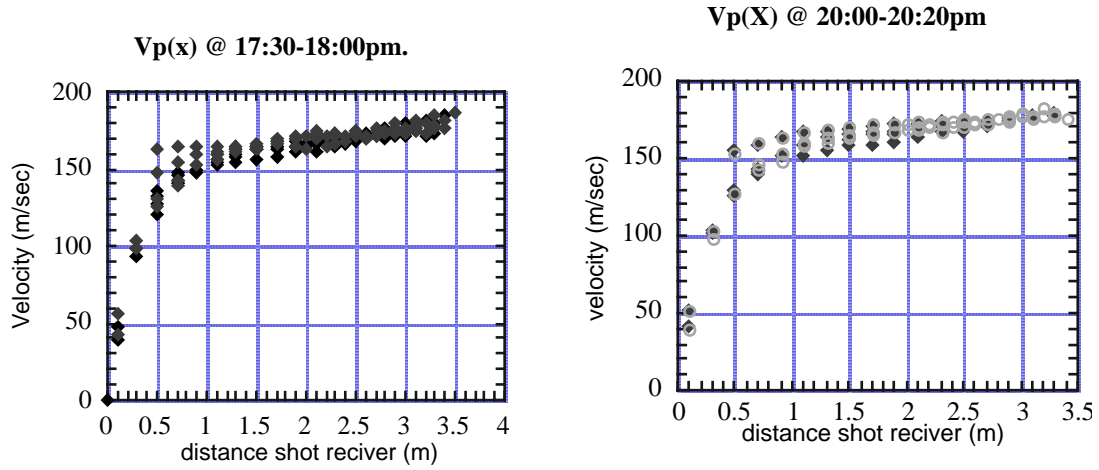
Figure 5: Velocity versus the shot-receiver distance. 10 different shot points have been used (two sets of shots with time interval of ~20 min). The water table can be assumed to be constant during the time of the shooting. (a) Shots between 17:30 and 18:00; (b) shots between 20:00 and 20:20.

Velocity (1/p) as a function of distance for spherical quartz grain (Hertz Mindlin prediction)
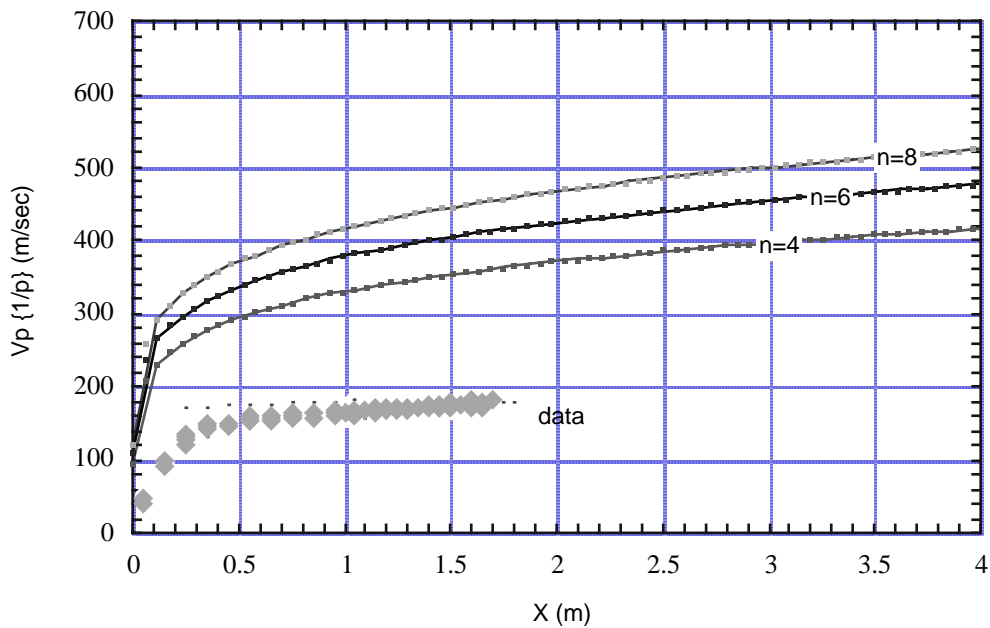
Figure 6: A comparison between the theoretic prediction of Hertz Mindlin theory (for quartz spheres) for different contact numbers, and the field data as collected in the experiment during 16:30-18:00

$$K_{HM} = [\frac{n^2(1-\phi_0)G^2}{18\pi^2(1-v)^2}P]^{\frac{1}{3}},$$

$$G_{HM} = \frac{5-4v}{5(2-v)}[\frac{3n^2(1-\phi_0)G^2}{2\pi^2(1-v)^2}P]^{\frac{1}{3}}$$

$$(3)$$

where v is Poisson's ratio and G is the shear modulus of the grains, ϕ_0 is the porosity of the pack of spheres, and n is the coordination number.

In general, P is the effective stress, defined as $P_{eff} = P_{total} - \alpha_b P_{pore}$ (Jaeger and Cook, 1969), where P_{total} is the total overburden pressure α_b is the Biot coefficient, and P_{pore} is the pore fluid pressure. We note that these quantities are defined macroscopically and usually for fully saturated sediments. In unsaturated sand above the water table, the air is connected to the surface, hence its pressure is zero. The water on the other hand has a negative pressure due to surface tension (Bear, 1972), and is concentrated around the grain contacts. The negative water pressure will result in the stiffening of the grain contact, and will in turn cause the total stress to be somewhat larger then the effective stress. However, for coarse-grained sand we do not expect very high capillary forces, and will first assume that the effective stress is equal to the overburden pressure, and will later see whether the capillary forces are negligible.

Assuming that hydrostatic pressure equals the overburden, we have $P = \rho g Z$ where $\rho = (1-\phi_0)\rho_s + \theta_w\rho_w$, ρ_s is the sand grain density, ρ_w is the water density and θ_w is the volumetric water content in the sand, Z is the depth, and g is the gravitational acceleration. Then the P wave velocity V_p is

$$V_p = \sqrt{\frac{K_{HM} + \frac{4}{3}G_{HM}}{\rho}}$$

$$(4)$$

When the pressure is zero, according to the Hertz-Mindlin theory, the effective stiffness of the aggregate is zero. However, the beach sand is not in vacuum. Thus there is finite velocity in the sand even when the confining pressure is zero, due to the air present (the sand and air can be viewed as suspension of grains in air). The effective stiffness of this material is calculated by Gassmann's equation (1951). The bulk modulus is:

$$\frac{K_{eff}}{K_0 - K_{eff}} = \frac{K_{HM}}{K_0 - K_{HM}} + \frac{K_{air}}{\phi_0(K_0 - K_{air})}, \quad G_{eff} = G_{HM}. \tag{5}$$

This gives the above-mentioned value of the lower velocity bound at zero overburden of 13 m/s.

A useful approximation for the Gassmann equation is (Mavko et al., 1995):

$$\frac{M_{eff}}{M_0 - M_{eff}} \cong \frac{M_{HM}}{M_0 - M_{HM}} + \frac{M_{air}}{\phi_0(M_0 - M_{air})} \tag{6}$$

where $M_i = K_i + \frac{4}{3}G_i$. Now M_{HM} can be expressed from equation as

$$M_{HM} = \alpha^2 Z^{\frac{1}{3}} \tag{7}$$

where α is:

$$\alpha^2 = \left(\frac{n^2(1-\phi_0)G^2}{\pi^2(1-\nu)^2}\rho g\right)^{\frac{1}{3}}\left(\left(\frac{(5-4\nu)4}{5(2-\nu)3}\right)\left[\frac{3}{2}\right]^{\frac{1}{3}} + \left[\frac{1}{18}\right]^{\frac{1}{3}}\right) \tag{8}$$

The velocity of the material is:

$$V_p = V_p(\alpha, Z) \cong \sqrt{\frac{M_{eff}}{\rho}} \tag{9}$$

We note that in general the parameter α is depth dependent through the water content (since θ_w is depth dependent, therefore the density ρ is depth dependent). This dependence can be easily incorporated given $\theta_w(Z)$. In our study we assumed a sharp transition zone above the water table and hence took θ_w to be constant at the residual water content.

4.5.2   Ray theory approximation

As mentioned before, the fact that velocity increases with distance between shot and receiver indicates that the velocity must also increase with depth. We use our theoretical model to calculate the velocity from the turning rays approximation.

The frequency content of the first arrivals was very wide (more than 2 KHz, Paper 1). For a dominant frequency of 500 Hz, the corresponding wavelength λ (for a layer with velocity 200 m/sec) is 0.4 m. The depth of the water table is 1-2 m, which contains several wavelengths. This justifies the use of the ray theory at this depth. The ray theory should be also applicable at shorter distances between the source and the receiver. Indeed, a smaller horizontal distance means a smaller depth, a smaller depth means a smaller overburden, and a smaller overburden means a lower velocity. Then, the wavelength is small as well (at a constant frequency content). Therefore, ray theory should provide approximation at all distances and depths of investigation.

The travel distance X and travel time T of the first arrival can be expressed as functions of the ray parameter p and the velocity $V = V(Z)$ as (Jakosky, 1950):

$$X = 2 \int_0^{H_{max}} \frac{pVdZ}{\sqrt{1 - p^2 V^2(Z)}}, \quad T = 2 \int_0^{H_{max}} \frac{dZ}{V\sqrt{1 - p^2 V^2(Z)}} \quad (10)$$

where H_{max} is the maximum penetration depth of the ray. The ray parameter p is kept constant during the travel time of the seismic wave and it can be expressed as:

$$p = \frac{1}{V(H_{max})} = \frac{\sin(i_0)}{V(Z = 0)}. \quad (11)$$

It can be shown that (Jakosky, 1950)

$$\frac{dT}{dX} = p. \quad (12)$$

By taking the velocity change with depth from equation (9), we can calculate the travel distance X by integrating equation (10).

Taking the material properties parameter α to be constant for each shot, we can plot a curve of the travel distance versus the velocity, as calculated from the travel time curve. In Figure 6 we give the relation between the velocity $V = \frac{1}{p}$, and the travel distance X calculated (by numerical integration) from equation (10) for different coordination numbers (n).

In Figure 6 we present our data as the velocity $V(H_{max}) = \frac{1}{p}$ versus distance X.

Since the ray parameter is the derivative of the travel time curve, as given by equation (12), the velocity in Figure 6 is plotted as a function of X/2. Note that we approximate the derivative of the travel time curve as the

$$\frac{dX}{dT} \approx V(\frac{X}{2}) \qquad\qquad . \qquad\qquad\qquad (13)$$

We find that the best fit to the data is for α =8600. We present the velocity profile with depth for the beach sand together with the Hertz-Mindlin predictions (with α = 8600) in Figure 7.

4.6   DISCUSSION

The results of comparing the field data to the theoretical model shows a good qualitative (but poor quantitative) agreement with the original Hertz-Mindlin theory for spherical quartz grains. The theoretical values overestimate the actual velocity by more than 100%. One reason for this overestimation may be that the grains are not purely quartz - some clay is present in the sand, which together with the water can lower the mineral moduli significantly. As we discussed before, the water films will increase the contact stiffness since they will push the grains toward each other, however we did not discussed the role of the thin water film on the contact area itself, which may result a lower stiffness. Finally, the lithostatic pressure taken as the effective stress may not be correct for calculating velocities in the horizontal direction -- significant difference may exist between the vertical and the horizontal stresses.

However, the functional form given by the Hertz-Mindlin theory is fairly universal (e.g., Murphy, 1982; Mindlin, 1949; Walton, 1987). This is why we adopt this functional form where the stiffness is proportional to the effective stress to the power of 1/3. In our seismic interpretation, we use this functional form and adjust parameter α empirically.

In order to correctly determine the depth of the water, we must use a different velocity than that calculated from the first arrivals. Figure 8 shows the correct velocity as a function of depth. It is clear that the velocity used by the regular

refraction interpretation scheme was not correct. The use of our depth-dependent velocity function placed the water table refraction at 17:30 pm local time to be at depth of 2.15m, which is the depth of the water table at low tide. The corrected depth to the water table as a function of time can be seen in paper 1.

4.6.1   Reflection Verification

An independent way to check the validity of our model was to use the reflection data. After a severe low-cut filter was applied to the data, the reflection from the water table was imaged (paper 1). Velocity analysis applied to the reflection yielded the NMO velocity of 240 m/sec (Figure 9). Since NMO velocity is approximately the root mean square (RMS) velocity of the layer, we can verify our model using the reflection data. The relation between the interval velocity, the stacking velocity, and the RMS velocity is given by (Dobrin and Savit, 1988):

$$V_{stacking} \geq V_{RMS} = \sqrt{\frac{1}{\tau} \sum_i V_{int}^2 \Delta\tau} \qquad (14)$$

and

$$\tau = \sum_i \Delta\tau, \quad \Delta\tau = \frac{\Delta Z}{V(Z)} \qquad (15)$$

We use this relation and find that the velocity function derived by our model with $\alpha=8600$ predicts RMS. velocity of 220m/sec. The NMO velocity is 240 m/sec (Figure 9). Therefore, we conclude that the velocity profile we obtained from the refraction inversion matches the reflection data with the error of 20 m/sec.

4.7   CONCLUSIONS

We found in this study some specific conclusions:

1) The velocity gradient in unconsolidated sand is very high at shallow depths, with values that are much lower than the velocity of sound in air. The lowest velocity physically possible for an aggregate of sand and air is ~13 m/s.

2) The Hertz-Mindlin theory qualitatively describes the vertical velocity profile in the sand. However, a quantitative description is still needed.

3) Field calibration can be done from the seismic data. In the case of the Moss Landing experiment, the velocity profile in the sand is the one presented in Figure 5.

In addition, the results have a general implication for shallow seismic data. The low velocity that was measured in the sand, together with the high velocity gradient reflects the complexity of shallow seismic acquisition in low velocity environments. The wavelength, as already discussed, is extremely small when the velocity is very low.   The shallow reflections usually contain high frequencies, and are often convolved with the ground roll. Therefore very small geophone spacing is needed to avoid spetial aliasing of the signal (especially the ground roll), which is often mistaken for reflections (Steeples and Miller, 1998). In our case the ability to image the reflections at 16 ms at such high frequencies was possible only due to the extremely short geophone interval we used (0.2 m). The use of very small geophone interval is extremely important in cases where the target is very shallow and the velocities are low.

4.8   ACKNOWLEDGEMENTS

discussions, and the students and staff of the Rock Physics Laboratory who helped to

carry out the experiment.

Velocity (1/p) as a function of distance: best fit alfa=8600
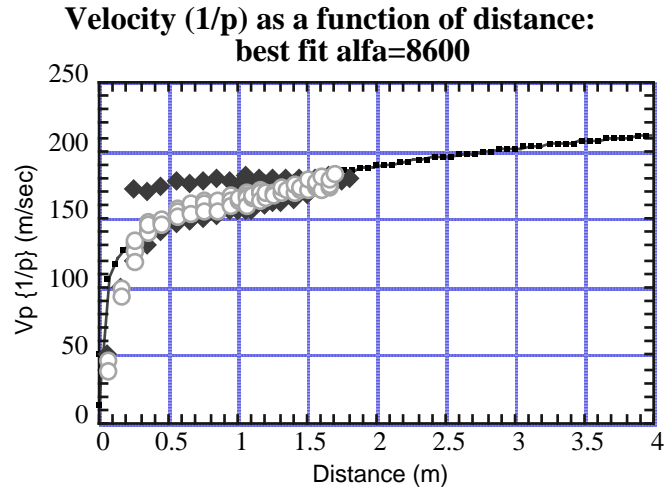
Figure 7:   A good fit to the data assuming a velocity profile of   is achieved with α of 8600

Velocity as a function of depth for Moss Landing Beach sand
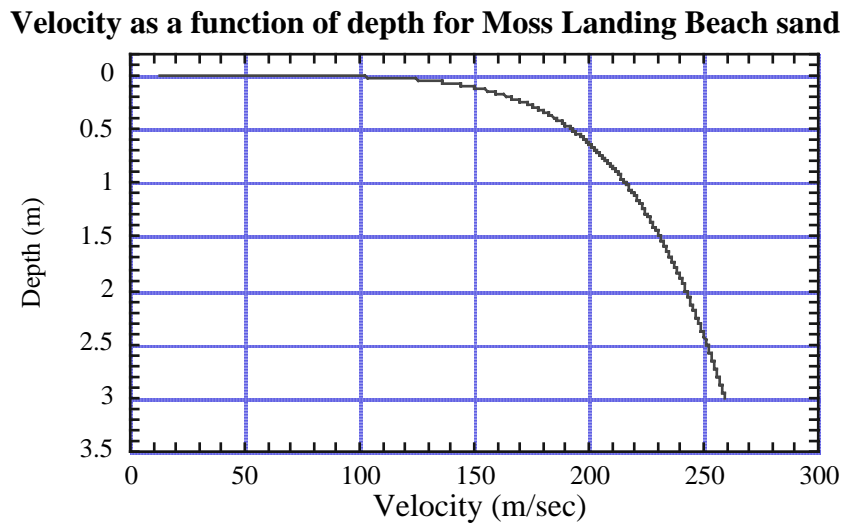
Figure 8:   Velocity as a function of depth for α =8600.
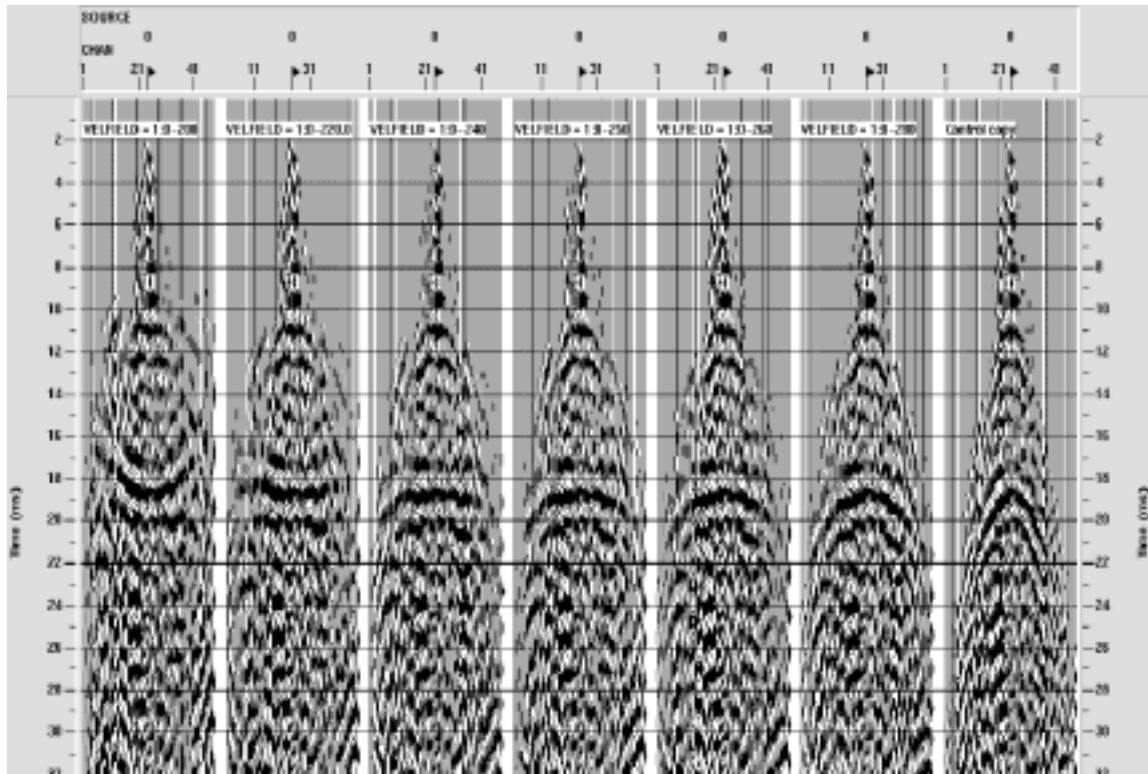
Figure 9: NMO velocity correction of the reflection from the water table at 17:30pm yields a velocity of 240m/sec, which is the velocity at depth of ~1m. These reflection are visible after severe low cut filtering (Paper 1).

4.9 REFERENCES

Bear, J., 1972, Dynamic of fluids in porous media, Elsevier Pub. Co., New York.

Dobrin, M. B. & Savit, C. H., 1988, Introduction to geophysical prospecting, New-York: McGRAW-HILL book company.

Dvorkin, Jack P., Nur, A., 1995, Elasticity of high-porosity sandstones: theory for two North Sea datasets.,SEG annual meeting expanded technical program abstracts with biographies, **65**, 890-893.

Gassmann, F., 1951, Uber die elastizitat poroser median, Vier. der natur Gesellschaft, **96,** 1-23.

Haeni, F., P., Grantham, D., G., and Ellefsen, K., 1987, Microcomputer-based version of SIPT-A program for the interpretation of seismic-refraction data, U. S. Geological Survey Open File reports: **87-103-A**.

Jakosky, J., J., 1950, Exploration geophysics, California: Trija Pub.

Jaeger, J. C. and Cook, N. G. W., 1969, Foundamentals of rock mechanics, Chapman and Hall, New York, 515P.

Mavko, G., Chan, C. and Mukerji, T, 1995, Fluid substitution; estimating change in Vp without knowing Vs, Geophysics, **60**, 1750-1755.

Mindlin, R., D., 1949, Compliance of elastic bodies in contact, J. Appl. Mech., **16**, 259-268.

Murphy, W., F., 1982, Effects of microstructure and pore fluids on the acoustic properties of granular sedimentary materials, Phd. thesis, Stanford University.

Steeples, D. ,W and Miller, R., 1998, Avoiding pitfalls in shallow reflection surveys, Geophysics, **63**, May, This issue.

Walton, K., 1987, The effective elastic moduli of a random pack of spheres. J. Mech. Phys. Sol., **35**, 213-226.

CHAPTER 5

ELASTICITY OF SHALLOW UNCONSOLIDATED SANDS: SEISMIC EXPERIMENT AND THEORETICAL MODEL

5.1   ABSTRACT

We determined P- and S-wave velocity depth profiles in shallow, unconsolidated beach sand by analyzing three-component surface seismic data. The data came from an experiment where we generated and propagated elastic waves in a high-compliance sand. P- and S-wave velocity profiles were calculated from the traveltime as measured on the vertical-component and tangential-component (SH) seismograms, respectively.

The sand is very homogeneous; therefore, we assume that velocities increase with depth only because of the increasing effective pressure. The derived velocities are proportional to the pressure to the power of 1/6, as predicted by the Hertz-Mindlin contact theory. However, the measured values of the velocities are less than half of those calculated from this theory. We attribute this disparity to the angularity of the sand grains. To model this effect, we assume that the average curvature radii at the grain contacts are smaller than the average radii of the grains, and we modify the existing theory accordingly. We estimate that for this experiment (using P-wave velocity) the ratio of the contact radius to the grain radius is about 0.086. This value represents a contact of a sharp grain edge against a flat surface.

Another disparity is between the observed Poisson's ratio (0.15) and the theoretical one (0.03 for quartz sand). We show that this discrepancy can be settled when slip at the grain contacts is accounted for. The larger the slip, the smaller the tangential stiffness between the grains and the larger the Poisson's ratio. We note that the acoustic tangential stiffness may be used to qualitatively asses the coefficient of internal friction of the sand. Therefore, by acoustically monitoring Poisson's ratio, one may estimate the sands strength characteristics.

5.2   INTRODUCTION

Relating the acoustic properties of unconsolidated granular materials to their physical characteristics (e.g., effective pressure, mineralogy, and porosity) is crucial for interpreting sonic and seismic measurements in sediments widely represented in the

Gulf of Mexico, North Sea, and other basins. Numerous measurements of elastic-wave velocities in such systems have been conducted in the lab and in situ, and theoretical models have been developed (see overviews in White, 1983; Wang and Nur, 1992).

In this study we are concerned with the acoustic properties of dry or partially-saturated unconsolidated sands at a very low effective pressure (up to 0.1 MPa or 15 psi), which corresponds to either very shallow (several feet) sediments or overpressured reservoirs. Laboratory measurements at such low pressures are hard to conduct because of transducer-sand coupling problems. The existing *insitu* measurements (White, 1983, Hunter, 1998) of shallow systems were made at depth ranges grater than those of our interest, and in more heterogeneous systems than ours.

Our approach was to conduct a three-component surface seismic experiment on a beach with closely spaced (0.3 m apart) geophones. By so doing, we were able to reconstruct the vertical velocity profile at a very shallow depth. Our next goal was to find an appropriate theoretical model to match the observations.

Most of the theoretical models that describe the elastic behavior of granular material are based on contact mechanics. The typical approach is to calculate the normal and shear contact stiffnesses of a two-grain combination and then use a statistical averaging to calculate the effective moduli of a random pack of identical particles. The classical Hertz-Mindlin model (Mindlin, 1949) relates the contact stiffnesses of two elastic spheres to confining pressure and the spheres' radii and elastic moduli. This model, used together with the statistical averaging (e.g., Walton, 1987), can accurately mimic experimental velocity results (Figure 1a).

The Hertz-Mindlin model successfully reproduced the functional form of the depth dependence (depth to the power of 1/6) of the P-wave velocity in shallow beach sand in our earlier experiments (Bachrach et al., 1998). However, in this low-pressure environment, this model overestimated the actual velocity values by a factor of two. This disparity between the experiment and the model also appears (for both V_p and V_s) in the experiments presented here.
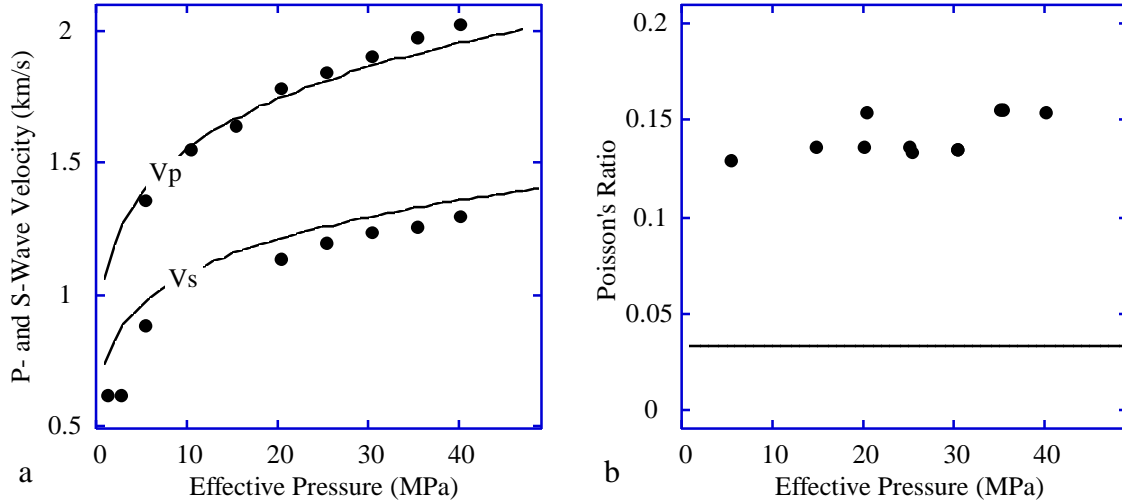
Figure 1: Compressional- and shear-wave velocities (a) and Poisson's ratio (b) in a dry, dense, random pack of identical glass beads versus confining pressure (experiments by Tutuncu, 1996). Symbols are from experiments; curves are from Hertz-Mindlin theory.

Another disparity between the Hertz-Mindlin model and experimental data, present at all pressures, is in Poisson's ratio values (Figure 1b). This observation has been supported by many experimental results (e.g., Spencer, 1994). Typical Poisson's ratio values in dry sands are between 0.1 and 0.2. Hertz-Mindlin model, on the other hand, predicts a value of about 0.01 for quartz sand. In experimental results presented here we observe the same disparity, with the experimental Poisson's ratio of 0.15.

In order to resolve these disparities between the experimental data and theoretical models, we first process our shallow seismic data to obtain vertical velocity profiles and then modify the Hertz-Mindlin model to match the data. To match the observed Poisson's ratio, we assume that in the sand, some grain contacts do not have shear stiffness. In order to match the observed velocity values, we assume that the grains are angular, and thus the average curvature radii at the grain contacts are smaller than the average radii of the grains.

5.3   THEORY

Walton (1987) shows that for a dry, dense, random pack of identical elastic spheres, the effective bulk (K_{HM}) and shear (G_{HM}) moduli are:

$$K_{HM} = \frac{n(1-f)}{12 pR_g} S_n, \quad G_{HM} = \frac{n(1-f)}{20 pR_g} (S_n + 1.5 S_t), \tag{1}$$

where n is the average number of contacts per grain; f is porosity; R_g is the grain radius; and S_n and S_t are the normal and shear stiffness of a two-grain combination, respectively. Equations (1) can be used with various contact models that produce expressions for the stiffnesses depending on the nature of the grain-to-grain contacts.

The Hertz-Mindlin model gives the following expressions for the contact stiffnesses of two elastic spheres in contact:

$$S_n = \frac{4aG}{1-n}, \quad S_t = \frac{8aG}{2-n},$$
(2)

where a is the radius of the contact area between the grains; and G and n are the grain shear modulus and Poisson's ratio, respectively. The radius of the contact area is expressed through the confining force F, and the contact curvature radius R_c as:

$$a = \left[\frac{3FR_c(1-n)}{8G} \right]^{\frac{1}{3}}.$$
(3)

The contact curvature radius depends on the local curvature radii of the two grains, R_1 and R_2, as follows:

$$R_c^{-1} = 0.5(R_1^{-1} + R_2^{-1}).$$
(4)
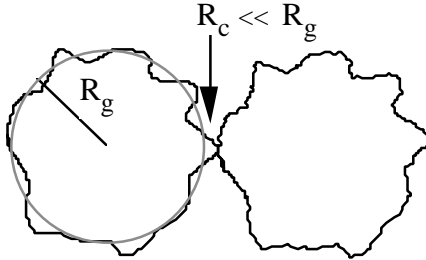
Figure 2: For angular grains, the contact radius may be much smaller that the grain radius. This effect may be pronounced at very low pressures in completely unconsolidated sand.

It is clear that for a pack of perfect spheres (glass beads), $R_c = R_g$. This assumption has been traditionally used when modeling unconsolidated sands (e.g., Dvorkin and Nur, 1996). However, for angular sand grains, this assumption is not necessarily valid. If a sharp edge contacts a flat surface, the contact radius may be

much smaller than the grain radius (Figure 2). This effect may be especially pronounced at very low pressures in completely unconsolidated sands.

The confining force F in equation (3) can be expressed through hydrostatic effective pressure P as follows (e.g., Marion, 1990):

$$F = \frac{4\boldsymbol{p}R_g^{\ 2}P}{n(1-\boldsymbol{f})}. \tag{5}$$

The above formulas can be used to relate the effective elastic moduli of a sand pack to the effective pressure, porosity, and the elastic moduli of the grains.

We can relate these moduli (in dry sand) to the depth of burial by assuming the effective pressure is related to the depth Z as follows:

$$P = \boldsymbol{r}_b gZ, \tag{6}$$

where $\boldsymbol{r}_b$ is bulk density and g is the gravitational acceleration. Generally speaking, the effective pressure is the difference between the overburden and the pore pressure. In this specific case, we explore sand at a low partial saturation with the air phase connected throughout the system. Therefore, the hydrostatic component of the effective pressure can be neglected.

The frame Poisson's ratio, $\boldsymbol{n}_{HM}$ is related to the bulk and shear moduli of the frame, the grain contact stiffnesses, and the mineral-phase Poisson's ratio as follows:

$$\boldsymbol{n}_{HM} = \frac{3K_{HM} - 2G_{HM}}{2(3K_{HM} + G_{HM})} = \frac{S_n - S_t}{4S_n + S_t} = \frac{\boldsymbol{n}}{10 - 6\boldsymbol{n}}. \tag{7}$$

Therefore, it follows from the Hertz-Mindlin model that the frame Poisson's ratio is a function of only the mineral-phase Poisson's ratio. Figure 3a shows that even for grains with high Poisson's ratio, the frame Poisson's ratio (as predicted by the Hertz-Mindlin model) remains very small. These small theoretical values significantly underestimate experimental results.

An explicit assumption in the Hertz-Mindlin model is that there is no slip between the grains except a small region at the periphery of the contact. Under acoustic excitation this region is negligibly small. This assumption results in a finite tangential stiffness, as given by equation (2).

Let us assume now that the tangential stiffness between the grains is zero. This may be the case in unconsolidated sand with water lubrication at the grain contacts. It

follows then from equation (7) that the Poisson's ratio of such material is 0.25 (Walton, 1987). Next we assume that sand is composed of a mixture of (a) material with no tangential stiffness at the grain contacts, and (b) material that obeys the Hertz-Mindlin model. For material (a), we still use the Hertz-Mindlin model to calculate the normal stiffness. Now let's use the upper and lower Hashin-Shtrikman (1963) bounds to estimate the effective elastic moduli of the mixture based on the moduli of the components and their volumetric fractions. An example of such calculations is shown in Figure 3b, where we assumed that the grains are quartz. In this case, the bounds are practically indistinguishable so we plot only one of them. It is apparent that, by allowing zero tangential stiffness in a fraction of the granular aggregate, we can match relatively high experimental Poisson's ratio values.
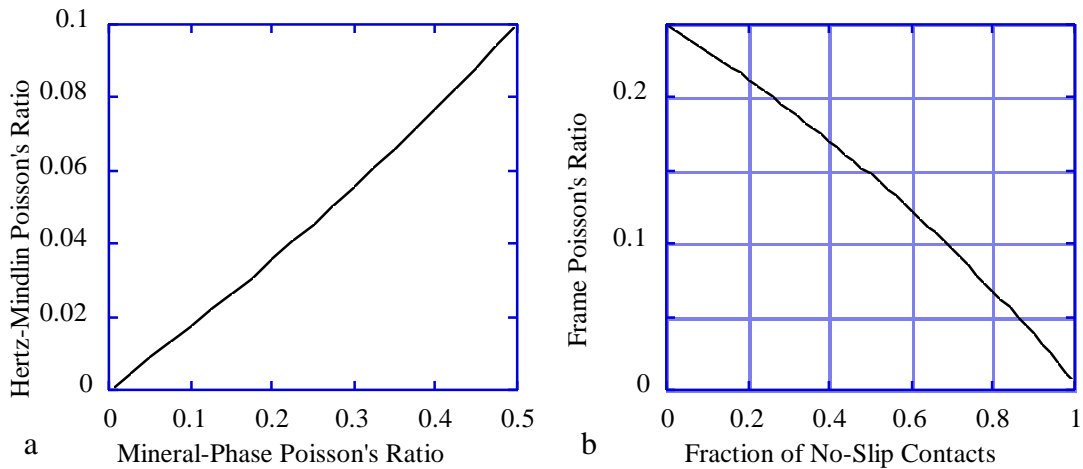
Figure 3: The Poisson's ratio of a grain pack versus (a) the grain Poisson's ratio as given by the Hertz-Mindlin theory; and (b) the volumetric fraction of the zero-tangential-stiffness material in the granular aggregate. The grains are quartz.

In this model the observed Poisson's ratio is an indicator of the amount of grains with no tangential stiffness. Furthermore, the acoustic tangential stiffness may be used to qualitatively asses the coefficient of internal friction of the sand. Then, by acoustically monitoring Poisson's ratio, one may estimate the stability of the sand. Figure 3b can be used as a diagnostic transformation between the observed Poisson's ratio and the fraction of the zero-tangential-stiffness material in the system.

At very low pressure, it is methodologically important to mention that dry sand is saturated with air. Therefore, even at zero effective pressure it has a finite compressional-wave velocity. The bulk modulus of the system with air (K_{Sat}) can be calculated from Gassmann's (1951) equation:

$$\frac{K_{Sat}}{K_g - K_{Sat}} = \frac{K_{HM}}{K_g - K_{HM}} + \frac{K_{Air}}{f(K_g - K_{Air})},$$
(8)

where K_{Air} and K_g are the bulk moduli of air and grain, respectively. The shear modulus (G_{HM}) remains unchanged. Because of the high compressibility of air this effect is negligible at depths below 1 cm. It is also important to note that in this calculation we ignored any cohesive forces between the grains. At partial-saturation the negative water pressure will increase the effective stress, and thus the shear wave velocity will not be zero(Bachrach and Nur, 1998). In our case (coarse beach sand) we assume very small value of negative pore-pressure.

Finally, the compressional- and shear-wave velocities are related to the effective moduli and bulk density as follows:

$$V_p = \sqrt{\frac{K_{Sat} + \frac{4}{3}G_{HM}}{r_b}}, \quad V_s = \sqrt{\frac{G_{HM}}{r_b}}.$$
(9)

5.4   EXPERIMENT

We collected the shear-wave data on Moss Landing beach, Monterey Bay, California. We used three component Galperin-mount 40 Hz geophones (Steeples et al, 1995) and a 60-channel acquisition system. The total line included 20 receiver locations. The station intervals were 30 cm and the seismic line was parallel to the shore. We used a very small mini-block source (Figure 4), that was made out of a metal block with two fins that could be inserted into the ground. We stacked about six shots in three directions: vertical, seaward and landward. To generate a signal, we applied vertical pressure to the source by standing on it, and than strike the side of the mini-block with the hammer.

To obtain a better signal-to-noise ratio for the shear waves, we enhanced the signal by negatively stacking the seaward and landward shot gathers. This technique is often used in land surveys with a mini-block source, since it cancels the monopole radiation pattern of the *S*-waves and enhances the dipole radiation pattern of the shear component of the source. After negatively stacking the shots, we rotated the seismogram in order to get the tangential and vertical components.

Figure 5 shows a raw shot gather, a vertical component shot gather, and a tangential component shot gather. The tangential seismogram clearly shows a curved shear-wave path and a slower, linear, high-amplitude Love wave train. The residual

energy in the tangential seismogram before the shear-wave arrival is residual P-wave energy.
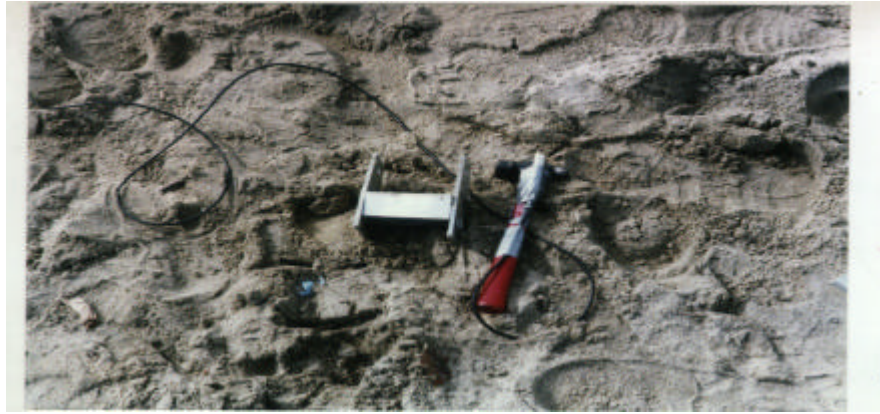
Figure 4: Shear wave source that was used to collect shear wave data. 0.25 Kg. Hammer was used for side impact on the mini-block.

We used the tangential seismogram to measure the travel time of the S-wave by picking it at the peak of the wavelet at every trace (the maximum energy criterion). To correct for first break, we subtracted the quarter-cycle travel time (6.55 ms) from the picked travel time values. For the P-wave travel time, we were able to directly use first breaks at each trace. The results are displayed in figure 6.

To calculate the velocity profiles, we assumed that both V_p and V_s depend only on depth and do not vary laterally. Furthermore, we chose the following functional forms for the dependence of these velocities on depth Z:

$$V_s(Z) = V_0 + a_s Z^{\frac{1}{6}}, \quad V_p^{Vacuum}(Z) = a_p Z^{\frac{1}{6}}, \tag{10}$$

where a_s, a_p, and V_0 are constants. V_p^{Vacuum} is the velocity in sand without any pore fluid (including air). In order to obtain the functional $V_p(Z)$ form for sand with pore fluid, we substituted equation (10) into Gassmann's equation (8). Note that since effective pressure is proportional to depth, equations (10) have the form given by the Hertz-Mindlin theory.

Next we used the ray theory by solving equation (11) to match the observed travel time (T) versus offset (X) data (Figure 6). By so doing, we found the unknown constants in Equations (10).

$$X = 2 \int_0^{H_{max}} \frac{pV(Z)dZ}{\sqrt{1 - p^2V^2(Z)}}, \quad T = 2 \int_0^{H_{max}} \frac{dZ}{V(Z)\sqrt{1 - p^2V^2(Z)}},$$

(11)

A
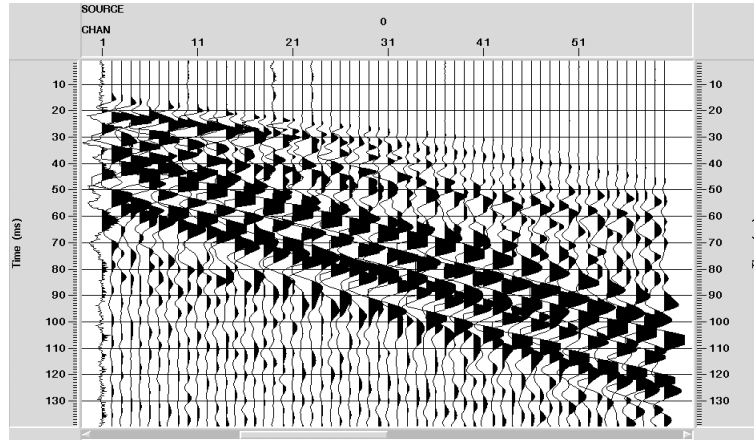
B
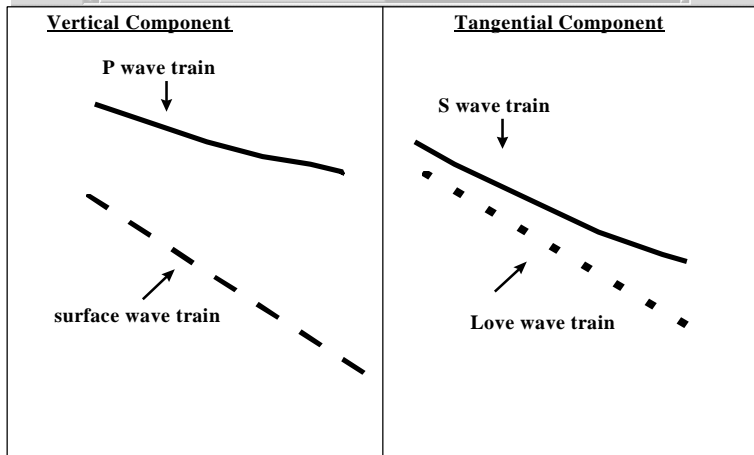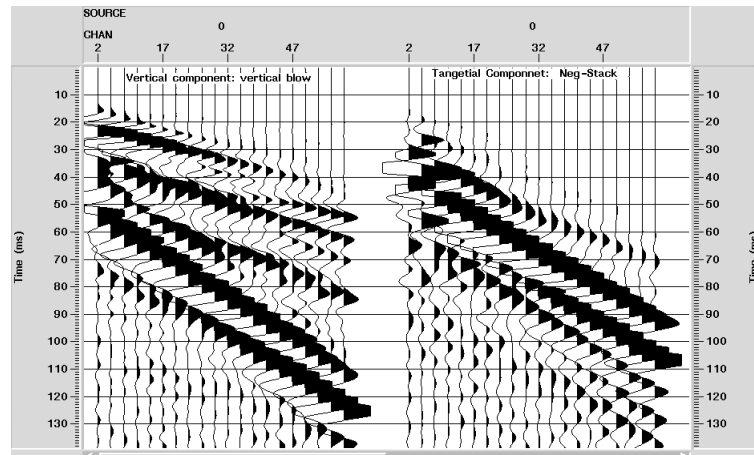
Figure 5: Seismic shot gathers from the beach. (A) 3-component 60-channel seismogram from the field. (B) Vertical and tangential components of the shot gather. (C) Seismogram interpretation. Note that the shear wave velocities on the tangential seismogram are slower then the P wave. Note also the curvature of the travel time curve, which is not visible with the constant-velocity Love waves.

A detailed description of such a procedure is given in Bachrach et al. (1998). Note that our choice of the physics-based velocity-depth functional forms allowed us to accurately match the data. because the transformation in equation (11) is unique, the solution represent the velocity function of the shallow sand.

We find that the Poisson's ratio calculated from V_p and V_s is depth-independent and equals 0.15. We estimate our error to be ± 0.03.

5.5   ANALYSIS OF THE DATA

In Figure 7 we plot V_p and V_s versus depth as measured in the experiment. The measured Poisson's ratio value (0.15) also greatly exceeds the theoretical value of 0.01, as given by equation (7).

5.5.1   Poisson Ratio

As described above, Poisson's ratio is used to diagnose the normal and tangential stiffness within the sediments grain boundaries. As shown in figure 3b, Poisson's ratio of 0.15 for a sand can be modeled as a random pack of spheres where half of its volumetric fraction has no tangential stiffness at grain contacts and half have no slip at the grain contacts. We note that theoretically, such a sand will have Poisson ratio of 0.15 at any depth/pressure, and any coordination number. This fact explain why Poisson's ratio is not pressure-dependent as observed at high confining pressure (Figure 1).

5.5.2   The Effect of Grain Angularity on Velocity

Figure 8 presents the observed velocity profiles for V_p and V_s, together with the velocity calculated from Hertz-Mindlin theory. In these calculations we assumed that the sand grains are quartz (the bulk and shear moduli are 36.6 GPa and 45 GPa, respectively), the porosity is 0.4 (as measured), and the number of contacts per grain, n, varied from 4 to 8. In these calculations we assume a binary mixture of slipping and non slipping grains to yield a Poisson ratio of 0.15 for the aggregate, as measured in the field (see previous discussion). For both P- and S- wave velocities, the theory largely overestimates the measured values. Note that if we had used the original Hertz-Mindlin formulation, we would have seen a larger disparity since the aggregate would have been stiffer.
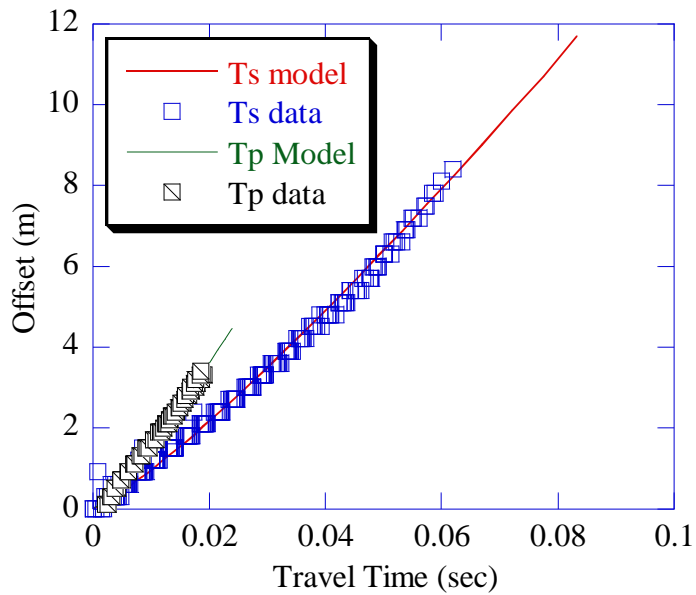
Figure 6: Travel time vs. offset for both P and S waves. The data are represented by the markers and the model uses to the best values for α_P and α_S which best fit the data.
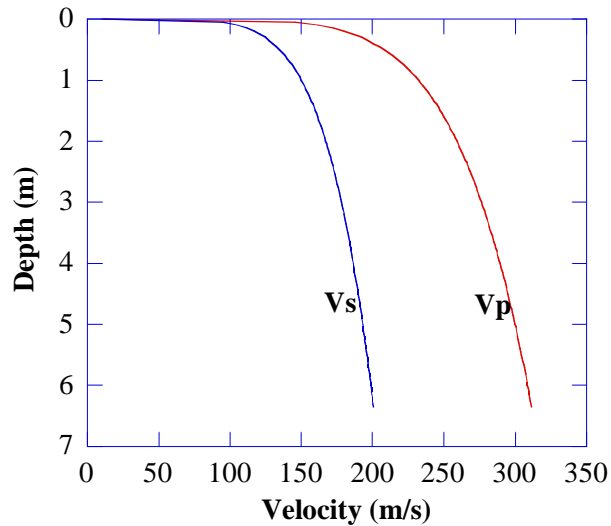
Figure 7: *Vp* and *Vs* as functions of depth from the best fit to the data (fig 6). The results yield a constant Poisson-ratio depth profile of 0.15.

We explain the disparity between the measured and theoretical V_p values by assuming that the contact curvature radius R_c is smaller (due to angularity) than the average grain radius R_g. We use equations (1), (2), (3), (5), (6), (8), and (9) to calculate the ratio of R_c to R_g. We find that for $n = 5$ (appropriate for loose sand) this ratio is 0.086. This value represents a contact of a sharp grain edge against a flat surface.
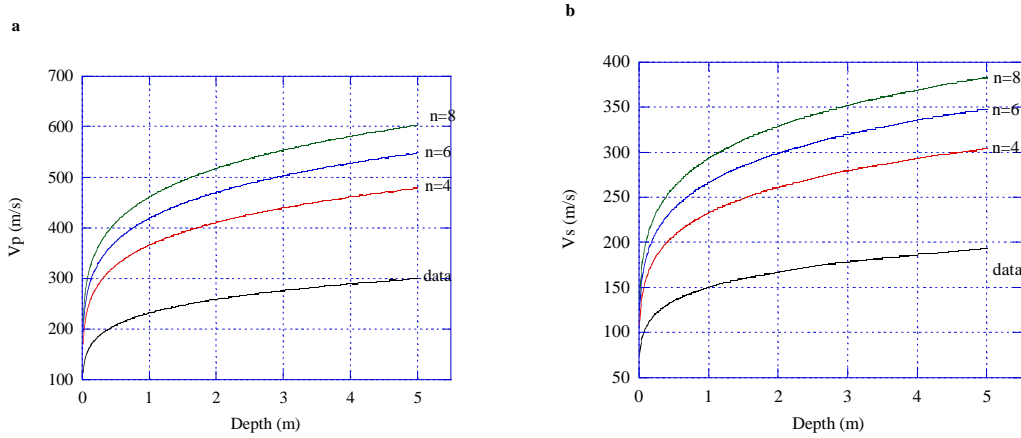
Figure 8: Depth vs. Velocity for contact model with constant grain size and different coordination number in comparison with the field data observed on the beach. a). *Vp* and b). *Vs* These values are calculated for a mixture of slipping and none slipping grains with Poisson ratio of 0.15.

Consistency of the model is checked as follows: We used the volumetric fraction of the grains with no tangential stiffness and the R_c to R_g ratio thus defined to calculate V_s directly from the Hertz-Mindlin theory (see appendix for details). The V_s values thus calculated are very close to the measured values (Figure 9).
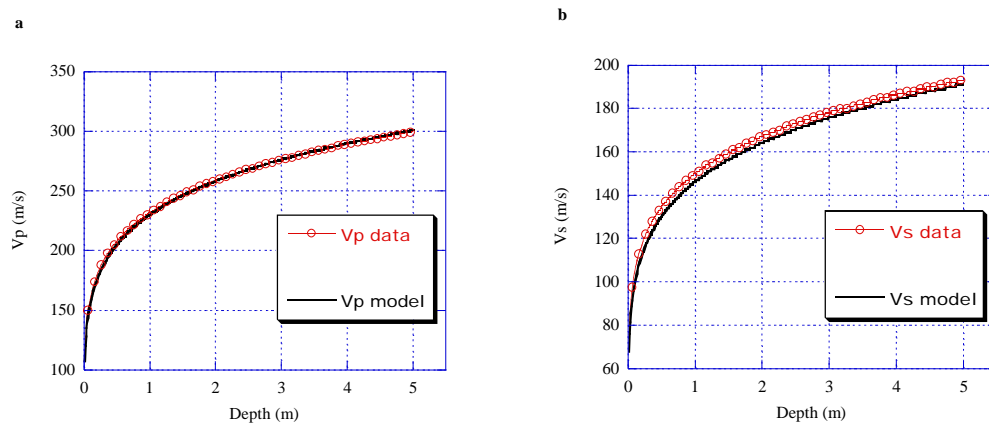
Figure 9: Vp (a) and Vs (b) as calculated from a model with *Rc*=0.086*Rg* and mixture of slipping and non slipping grains with effective Poisson ratio of 0.15.

Note that the data was calibrated by matching *Vp*. This calibration agrees with *Vs.*

5.6   DISCUSSION

We have shown that the observed Poisson ratio can be modeled by a binary mixture of grains with slipping and non-slipping boundary conditions. We also showed that the observed velocity profile can be derived from the grain elastic moduli when angularity is taken into account. It can be shown that the Poisson ratio estimation is decoupled from the angularity of the grains in the aggregate. This means that the Poisson ratio can be used to asses the grain-contact strength directly from figure 3 for any Hertzian material. The boundary condition of no tangential stiffness along the grain contact can be physically caused by liquid along the boundaries or/and by stress localization (i.e. the hydrostatic pressure is not carried by all the grains in the system, but through preferential stress-chains).   We speculate that this parameter may be important in the assessment of the angle of internal friction. We are still trying to gain better physical understanding of this behavior.
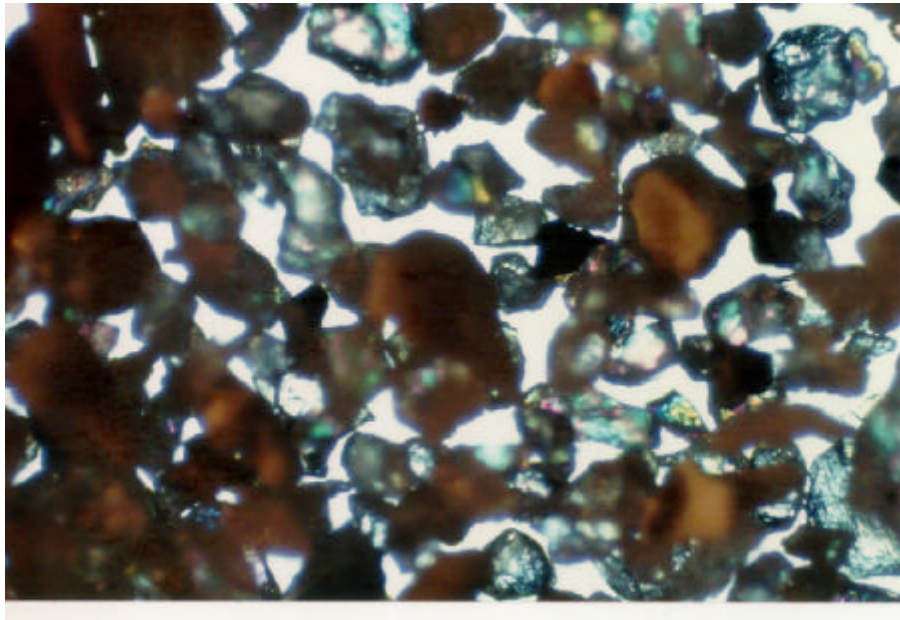
Figure 10: Microscopic image of Moss Landing beach-sand. This sand can be classified as angular, with Waddell class interval of 0.17-0.25 (Boggs, 1987).

Figure 10 shows a magnified picture of Moss-beach sand.   The beach sand angularity derived from this figure 10 using the Wadell class interval (Boggs, 1987) classification is $R_W \approx$ 0.17-0.25, where R_W is given by equation (12):

$$R_W = \frac{\sum R_c}{NR_g} \tag{12}$$

We derived an angularity parameter of 0.086 from our data. This discrepancy is expected, since angularity used in Hertz-Mindlin theory represents a mechanical property average, whereas the one derived from equation (12) is a simple mean. The smaller angularity in the mechanical model represents a more compliant structure, which is likely to be affected by the weaker part of the system (i.e. sharper grain contacts).

5.7   COMPARISION TO OTHER MEASUREMENTS:

We compare our modeling results to a shallow shear wave profile obtained in unconsolidated glacial deposits in the Fraser river delta, near Vancouver, Canada (Hunter, 1998). These shear wave measurements, from downhole log and seismic cone penetrometer measurements (SCPT) are used to compare our sand behavior with that of other unconsolidated sediments. Since the glacial sediments are saturated, we use Gassman's equation to compensate for the density effect. The results are shown in figure 11.
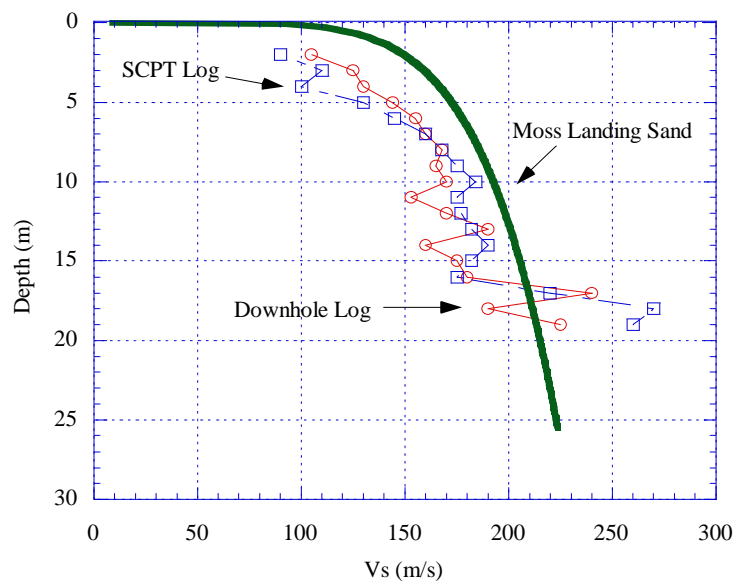
Figure 11: Comparison of shallow beach sand shear wave velocity to measured shear-wave velocities in unconsolidated glacial sediments (Hunter, 1998). Note that the general velocity profile is in good agreement with the one measured in more heterogeneous glacial sands.

5.8   CONCLUSIONS

We have shown in this paper that:

1). The Poisson ratio of moss landing beach sand is 0.15. This can be modeled by an effective aggregate of grains with no tangential contact stiffness and grains with no slip boundary conditions.

2). The sand shear-wave velocities are lower than the velocities predicted from a random pack of identical spheres. This discrepancy can be explained by the angularity of the grains. Thus, the difference between the expected velocity and the measured velocity can serve as a measure of the grain angularity. We note that this measure is a mechanical measure and is not directly related to the simple average angularity often used in sedimentology for sand classification.

3). The functional dependence of the shear wave velocity is general and is not limited to Moss Landing beach sand. This dependence is observed in other depositional environments (e.g. glacial sediments).

5.9   ACKNOWLEDGMENTS

5.10   REFERENCES

Bachrach, R. and Nur, A., 1998, High resolution seismic experiments in sands Part I- Water table, fluid flow and saturation: Geophysics, In press.

Bachrach, R. Dvorkin, J. and Nur, A., 1998, High resolution seismic experiments in sands Part II- Velocities in shallow unconsolidated sands: Geophysics, In press.

Boggs, J.S.,1987, Principles of sedimentology and stratigraphy: Merrill publishing company, Columbus OH.

Dvorkin, Jack P., Nur, A., 1996, Elasticity of high-porosity sandstones: theory for two North Sea datasets, Geophysics: Geophysics,**61**, 1363-1370.

Gassmann, F., 1951, Uber die elastizitat poroser median: Vier. der natur Gesellschaft, **96,** 1-23.

Hunter, J, 1998, Shear wave measurements for earthquake hazards studies, Faser river delta, British Colombia: Proceedings of the symposium on the application of geophysics to enviromental and engineering problems.

Hashin, S. and Shtrikman, S., 1963, A variational approach to the elastic behavior of multiphase materials: J. Mech. Phys. Solids, **11**, 127-140.

Mindlin, R., D., 1949, Compliance of elastic bodies in contact: J. Appl. Mech., **16**, 259-268.

Marion, D., 1990, Acoustical, mechanical, and transport properties of sediments and granular materials: Ph.D. Thesis, Stanford University.

Spencer, J. W., 1994, Frame moduli of unconsolidated sands and sandstones: Geophysics, **59**, 1352-1361.

Steeples, D. ,W Macy, B. and Schmeissner, C., 1995, S wave and 3-component seismology: Near-surface seismology short course, SEG.

Wang, Z. and Nur, A., 1992, Seismic and acoustic velocities in reservoir rocks; Volume 2, Theoretical and model studies: Society of Exploration Geophysicists, Tulsa, OK, 457p.

Walton, K., 1987, The effective elastic moduli of a random pack of spheres: J. Mech. Phys. Sol., **35**, 213-226.

White, J. E.,1983, Underground sound: application of seismic waves: Methods in Geochemistry and Geophysics ; **18,** 253p.

CHAPTER 6

ULTRA-SHALLOW SEISMIC REFLECTION IN UNCONSOLIDATED SEDIMENTS: ROCK PHYSICS BASIS FOR DATA ACQUISITION.

6.1   ABSTRACT

Typical high-resolution shallow seismic methods target depths of < 500m. However, obtaining high-resolution seismic reflection images at depths shallower than 5-10m is often assumed not to be possible. There is a great need for better physical understanding of the seismic response of the very shallow subsurface for evaluating the feasibility of acquisition and for optimal survey design in different conditions.

In this chapter I address the problem of ultra-shallow seismic acquisition in unconsolidated sediments. I show that the velocity profile in the upper few meters of unconsolidated sediments is pressure dependent, and that the very near-surface P and S wave velocities (in undersaturated sediments) are always very low. Then I show that, given this velocity profile, groundroll will be attenuated greatly by scattering in the presence of very mild surface roughness. This attenuation of the high frequencies of the groundroll causes a separation of the reflection energy from the groundroll energy in the frequency domain. This separation enables us to image seismic reflections in the very shallow subsurface. I present field examples from three different locations where I was able to obtain very shallow reflections (1-3m) in unconsolidated sediments. These finding shows that in <u>any</u> unconsolidated material, ultra-shallow reflection imaging is possible given sufficient bandwidth.

6.2   INTRODUCTION

Ultra-shallow seismic acquisition is an underdeveloped field (Steeples et al. 1997). Typically high-resolution shallow seismic reflection surveys target reflections in the "optimum" window range (Hunter at al, 1984), defined as the zone between the first arrivals and the groundroll (Fig. 1).   In this zone, the reflections are not

contaminated by the groundroll, and can be easily imaged. However, using the optimum window technique does not allow for very short offsets, and therefore reflections shallower than 35-50ms are difficult to image. Hence, using the optimum window concept limits the reflection profile to depth grater than 5-10m. Therfore, for ultra shallow imaging one must image the reflections inside the groundroll.

The attenuation of groundroll is typically done using geophone arrays (Dobrin, 1988) or frequency filtering (Steepples, 1995). Geophone arrays are not very useful in ultra-shallow reflection surveys because the dimensions of such arrays are typically larger than the required station spacing in ultra-shallow applications. Therefore, frequency filtering is the only effective tool for attenuating groundroll. The ability to obtain shallow reflections is dependent on the separation of groundroll and reflected energy in the frequency domain. In this chapter I show that in unconsolidated sediments, where velocities are pressure dependent, this separation is expected, and reflection profiling of the ultra-shallow subsurface is theoretically justified. The challenge of the practitioner is now to design acquisition parameters, that will take advantage of this physical fact.
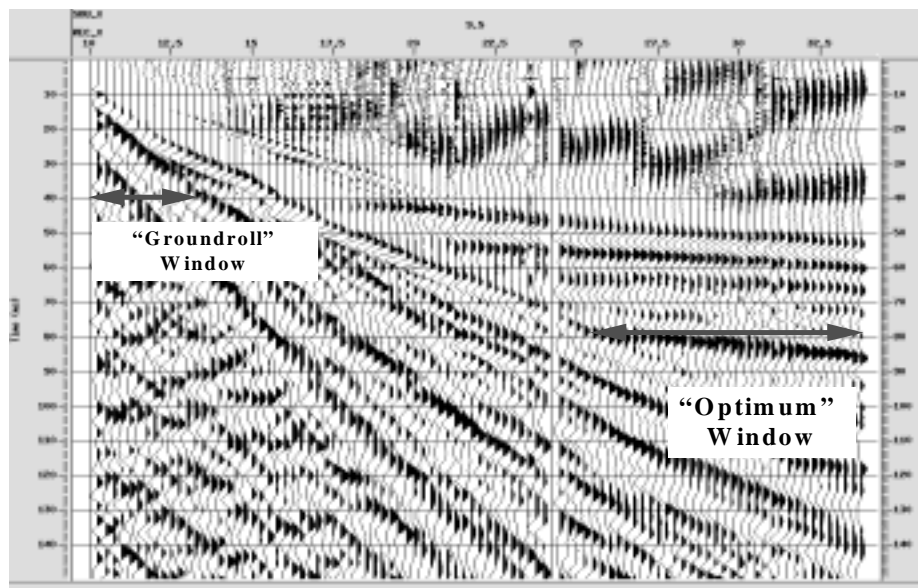
Figure 1: The optimum window and groundroll window in shallow shot gather. Data collected on a river point bar with 40Hz geophones and a small hammer source in July, 1997.

6.3   P-, S- AND RAYLEIGH-WAVE VELOCITY PROFILES IN SHALLOW UNCONSOLIDATED SEDIMENTS

6.3.1   P and S waves in unconsolidated shallow sediments

The overburden pressure governs velocities in unconsolidated sediments. In chapter 4 and 5, I showed that the pressure dependent P- and S-wave velocity profiles in sands can be successfully modeled based on contact mechanics. The functional dependence of the velocity-depth profile in general is related to the grain elastic moduli, density, shape, the porosity etc. In unconsolidated sediments, the top layer of grains are a suspension of grains in air at critical porosity (Nur, et al, 1995), and the elastic stiffness increase with depth is due to the effect of overburden pressure on contact stiffness. This dependence is given in equations (1) and (2).

$$G_C = \alpha_G Z^{\frac{1}{6}}, \quad K_C = \alpha_K Z^{\frac{1}{6}}$$

$$\frac{1}{K_U} = \frac{1}{K_U} + \phi \bigg/ \left(K_0 + \frac{K_0 K_{air}}{K_0 - K_{air}} \right), \quad G_U = G_C,$$

$$(6.1)$$

where K_U and G_U are bulk and shear moduli of the sediment, Z is depth, ϕ is porosity, K_0 is grain modulus, K_{air} is air bulk modulus α_G and α_K are constants which in general are functions of all the other sediments parameters, and can be determined experimentally. The effective bulk and shear moduli in vacuum are given by K_C and G_C respectively.

The P- and S-wave velocity are given by:

$$V_p = \sqrt{\frac{K_U + \frac{4}{3} G_U}{\rho}}, \quad V_s = \sqrt{\frac{G_U}{\rho}}$$

$$(6.2)$$

where ρ is the bulk density of the sediment.

The plot of P and S-wave velocities in unconsolidated sand (Fig. 2) show that the velocity gradient is very steep near the surface, and the P- and S-wave velocities at

the surface are very low. I will show next that this fact causes separation of groundroll energy from the reflected energy.
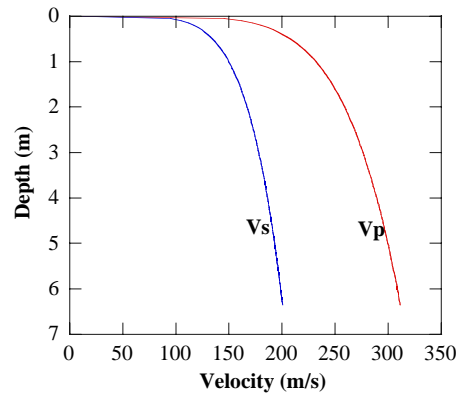
Figure 2: Velocity profiles in shallow unconsolidated sand. This profile is typical of unconsolidated sediments with pressure dependent velocity.

6.3.2   Review of Rayleigh Waves

Surface waves on vertical seismograms are primarily Rayliegh waves. I review here basic surface wave theory which is important for this discussion.

The Rayliegh-wave velocity, V_R, is given by the real-value solution to the characteristic equation:

$$\left(2-\left(\frac{V_R}{V_s}\right)^2\right)^2-\left(4-\left(\frac{V_R}{V_p}\right)^2\right)^{\frac{1}{2}}\left(1-\left(\frac{V_R}{V_p}\right)^2\right)^{\frac{1}{2}}=0 \qquad (6.3)$$

For a real solution to exist, Rayliegh-wave velocity must be lower than Vs. For all earthen materials, $0.86Vs <V_R <0.96Vs$ (White, 1983).

The derivation of this solution assumes an homogeneous, isotropic elastic halfspace. Under these conditions, Rayliegh waves are non-dispersive, as stated clearly in equation (6.3) (no frequency dependence). The amplitude of the surface waves are negligible at depths grater than two wavelengths under the surface. The dispersion of Rayliegh waves is typically studied in layered media with velocity increases with depth, and thus the longer wavelengths propagate faster than the shorter wavelength (Aki and Richards, 1981). Note that in layered media, when the wavelengths are

shorter than the thickness of the first layer (as is often the case at high frequencies) the surface waves will still preserve their high frequencies.

6.4   OPTIMUM   WINDOW   IMAGING   IN   SATURATED UNCONSOLIDATED SAND

The "optimum window" concept was developed for the optimal location of geophones while using engineering seismograms, with a limited number of channels (Hunter et al., 1984). As discussed before, the optimal window usually constrains the depth of investigation to be deeper than a few meters. It is important to note, however, that in fully-saturated unconsolidated sediments (in environments where the water table is at the surface), one can achieve very shallow reflection sections using the optimum window. This is because the velocity of fully saturated sediments is fundamentally different from dry/partially saturated sediments. As predicted by Biot-Gassman theory, the shear-wave velocity of saturated sediment is slightly lower than the dry shear velocity, due to the density effect. The P-wave velocity of fully-saturated material is significantly higher than the dry velocity. The Poisson's-ratio of fully-saturated, low-pressure, unconsolidated sediments is very close to 0.5 (Bachrach et al, 1997).   Under these conditions the velocity of the P wave is very high. However, the groundroll velocity, which is the Rayliegh-waves velocity is still slower than the shear wave velocity, (less than 1/10 of the P-wave velocity). This fact causes the "optimum window" to get very wide, even in the shallow part of the seismogram. Thus, in fully-saturated unconsolidated sediments the optimum window is often wide enough to provide very shallow reflections, as shown in figure 3.
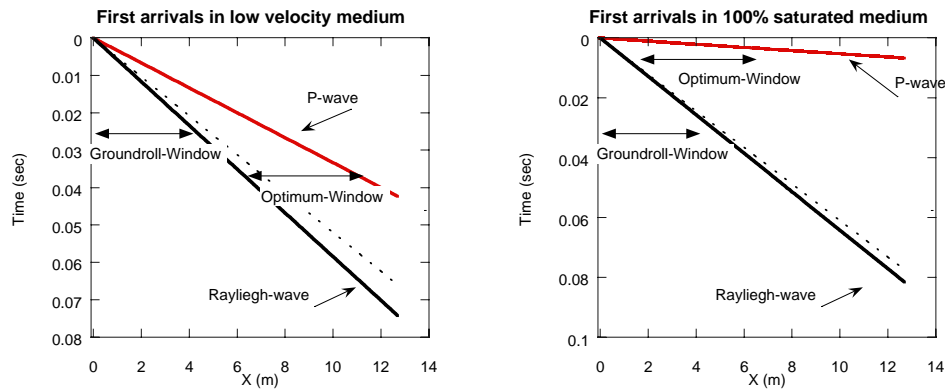
Figure 3: The optimum window in low velocity materials is very narrow (left). At 100% saturation (right) the optimum window gets very large because of the sharp increase in P-wave velocity and the decrease in S-wave velocity due to the density effect. In this example, I used dry Vp of 300m/s and Poisson's ratio of 0.15.

6.5   IMAGING INSIDE THE GROUNDROLL IN UNCONSOLIDATED SEDIMENTS: FIELD OBSERVATIONS

Figure 4a presents a shot gather collected on beach sand, together with its power spectrum. Reflections in the gather at the very top part of the seismogram are masked by the surface waves, seen here as the low velocity waves propagating at a steep angle along the seismogram. Figure 4b presents the same seismic section after frequency filtering. Note that there are clear reflections at 20 and 10ms, which were not visible before. In Figure 5 we show two more shot gathers from two different depositional environments: A river point-bar (A,B) and soil over bedrock (C,D). Note that the very shallow reflections can be seen in all shot gathers inside the groundroll window after low-cut filtering. Again, there is a good separation in the frequency domain between groundroll and reflections. Note also that the velocities in all three shot records are very low (slower than the airwave). Thus the attenuation of the groundroll in very short offsets is common in all of these cases.

It is known from theory that the Rayleigh waves are non-dispersive in a homogenous elastic medium. The question then is why is there such a separation in the frequency domain between groundroll and the shallow reflections? What is the physical reason that enables us to suppress the groundroll and yet retain the reflections?

To answer this question I will go back to the basic attenuation mechanism of groundroll.
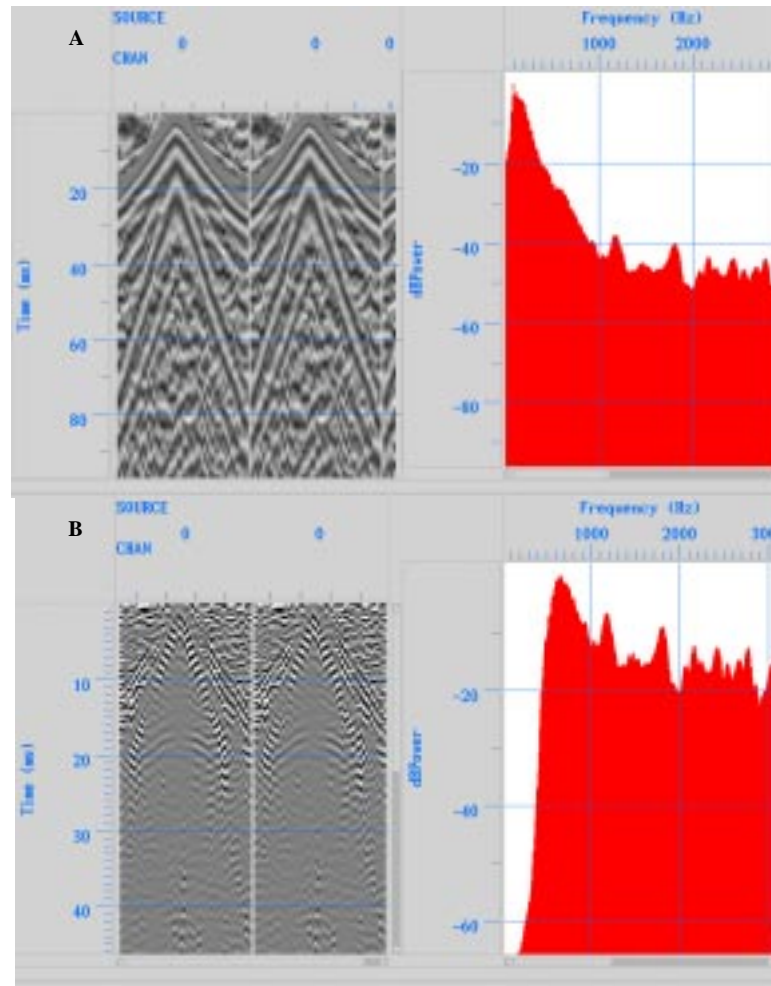
Figure 4: Power spectrum of a shot gather: A. Raw data (acquired with 40Hz Geophones) B. Same gather after low cut filtering of 700Hz. The reflections are clearly visible inside the groundroll zone due to a good separation between groundroll and reflection energy in the frequency domain.
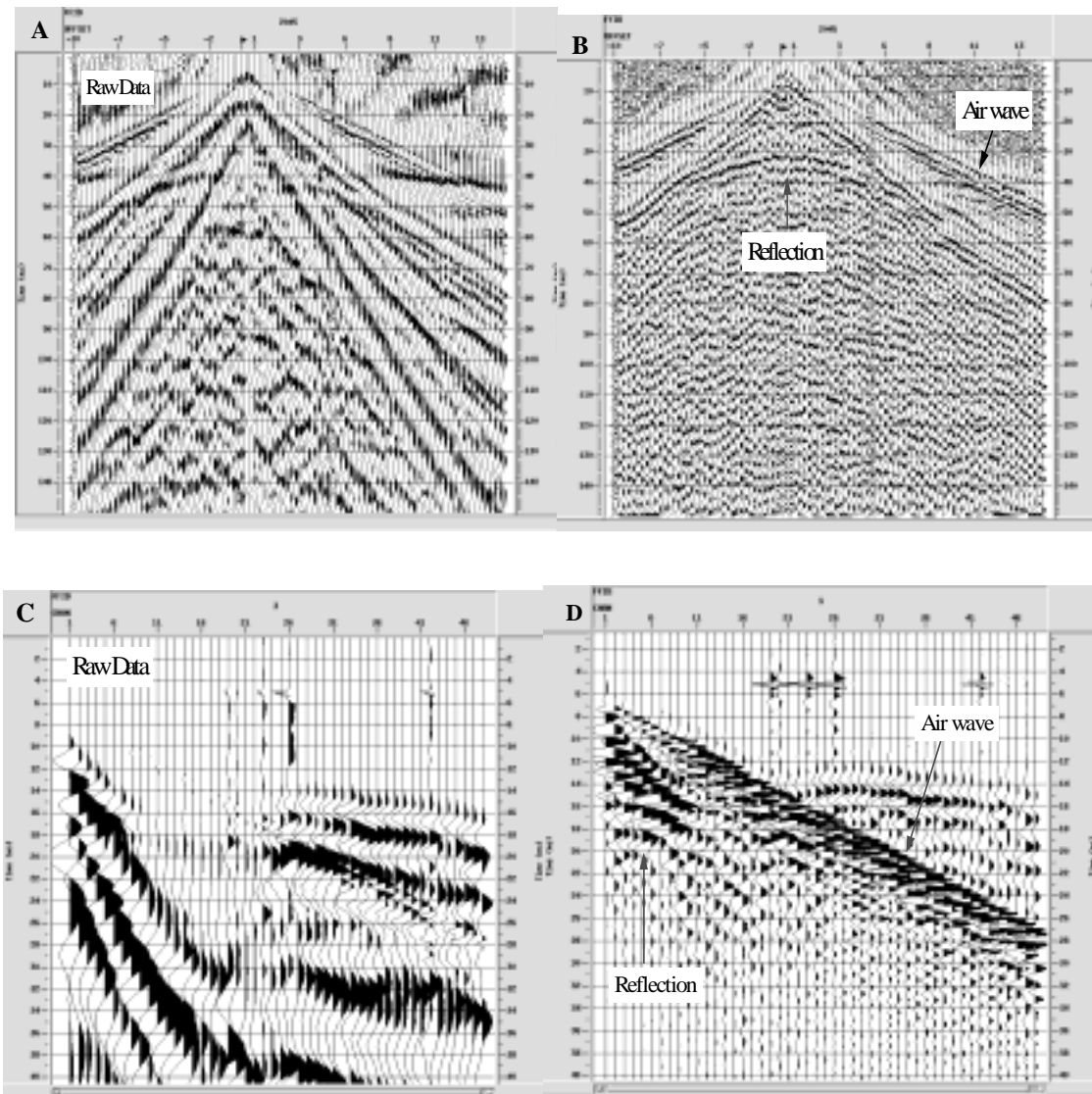
Figure 5: Data from different geological environments A. Raw data from a river sand bar. B. same as A but with 300Hz lowcut. C. Raw data from Soil over bedrock. D. same as C but with 500Hz. low cut filter.

6.6   THE ATTENUATION OF RAYLEIGH SURFACE WAVE DUE TO SURFACE ROUGHNESS IN LOW VELOCITY UNCONSOLIDATED SEDIMENTS

The attenuation of surface waves depends on two main factors: (1) energy loss per unit cycle due to viscoelastic and inelastic effects and (2) scattering attenuation. We show next that in unconsolidated sediments the separation of reflected-wave energy from the Rayleigh-wave energy in the frequency domain is expected and is mainly caused by the scattering attenuation of the surface wave from the surface roughness.

The attenuation of Rayleigh surface waves due to surface roughness was studied in detail by Maradudin and Mills, (1976). They used elastodynamic Green's function with a first order Born approximation to derive the energy loss per unit distance for a Rayleigh wave. A review of the theory of scattering attenuation due to surface roughness and the derivation of the attenuation coefficient is given in the appendix.

For a Gaussian surface roughness with a correlation length a, and RMS amplitude δ, the attenuation length of the Rayleigh wave, β (which represents the energy lost per unit distance traveled by Rayleigh wave due to scattering from the surface roughness) can be approximated by the expression:

$$\beta = \alpha_0 f(a\omega/V_R) \tag{6.3}$$

where

$$\alpha_0 = \frac{\delta^2 a^2 \omega^5}{\pi V_R^5}, \tag{6.4}$$

$$f(a\omega/V_R) \cong$$

$$\frac{\pi^2}{R^2} \frac{V_R^4}{V_S^4} (1 - \frac{1}{2}\frac{V_R^2}{V_S^2})^{-2} (1 - \frac{V_R^2}{V_P^2})^{-1} \exp(-\frac{1}{2}\frac{a^2\omega^2}{V_R^2}) \tag{6.5}$$

$$\times \left[(1 - \frac{V_S^2}{V_P^2})^2 I_0(\frac{1}{2}\frac{a^2\omega^2}{V_R^2}) - 2(1 - \frac{V_S^2}{V_P^2})\frac{V_R^2}{a^2\omega^2} I_1(\frac{1}{2}\frac{a^2\omega^2}{V_R^2}) + 3\frac{V_R^4}{a^4\omega^4} I_2(\frac{1}{2}\frac{a^2\omega^2}{V_R^2}) \right].$$

and in the limits

$$f(a\omega/V_R) \cong$$

$$\frac{\pi^2}{R^2}\frac{V_R^4}{V_S^4}(1-\frac{1}{2}\frac{V_R^2}{V_S^2})^{-2}(1-\frac{V_R^2}{V_P^2})^{-1} \tag{6.6}$$

$$\times \left[(1-\frac{V_S^2}{V_P^2})(\frac{1}{2}-\frac{V_S^2}{V_P^2})\right]+\frac{1}{32}, \qquad \frac{a\omega}{V_R} << 1$$

$$\times \left[(1-\frac{V_S^2}{V_P^2})^2\frac{V_R}{\pi^{1/2}a\omega}\right], \qquad \frac{a\omega}{V_R} >> 1$$

V_P, V_S and V_R are the *P*-, *S*- and Rayleigh-wave velocities in the sediment, respectively, I_i is the modified Bessel function of the first kind, ω is the angular frequency and *R* is a constant given by:

$$R = \frac{1}{(1-\frac{V_R^2}{V_s^2})^5}\left[\frac{V_R^4}{V_S^4}(1+2\frac{V_S^2}{V_P^2})^5 - \frac{V_R^2}{V_S^2}(9-5\frac{V_S^2}{V_P^2})+8(1-\frac{V_S^2}{V_P^2})\right] \tag{6.7}$$

For most unconsolidated sediments with Poisson ratio of 0.1-0.2, the Rayleigh-wave velocity is $V_R \cong 0.9V_S$. Note also that β is related to the amplitude of the surface roughness squared (δ^2), the correlation length squared (a^2) and the Rayleigh wavelength to the power of (-5) (λ_R^{-5}). The attenuation length β as a function of different surface roughness amplitude and different shear wave velocities is shown in Fig. 6. Fig. 7 shows a 300Hz wavelet transmitted in a medium which has 0.5m correlation length and δ of 2cm. Note that in the low-velocity material, the wavelet is almost totally attenuated. Note also that for higher velocities the attenuation coefficient is much smaller.
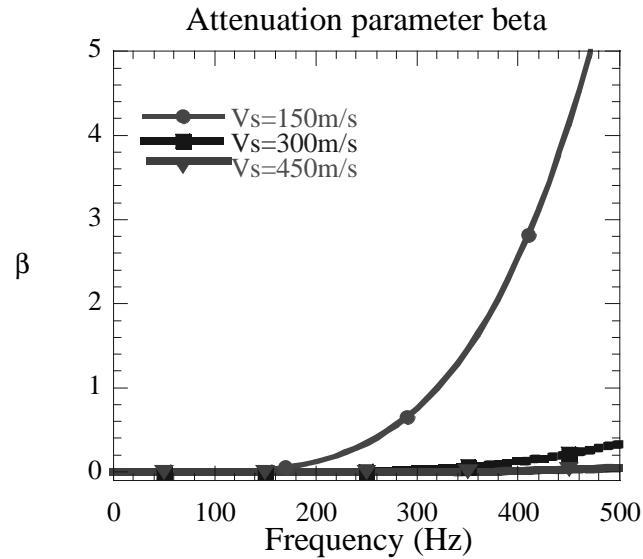
Figure 6: Attenuation parameter β for 3 different media with V_P and V_S of (A) 240m/s and 150m/s, (B) 480m/s and 300m/s, and (C) 720m/s and 450m/s.

6.7   SUMMARY AND CONCLUSIONS

We have shown that ultra-shallow seismic reflections can be obtained if they can be separated from the groundroll that masks these events in the very short offset part of the seismogram. We have also shown that the velocity profile in shallow, unconsolidated sand causes the surface-wave wavelength to be very small. Thus the effect of even mild surface roughness (say 2cm height), is significant for the attenuation of the surface wave even at very short offsets.

In my numerical example, a 300Hz wavelet was critically damped within less than 5m of propagation in a material with V_P and V_S of 240m/s and 150m/s, respectively. I note that the actual attenuation of the high-frequency surface wave is not a function of the velocity alone, but has other parameters which affect it (such as correlation length, surface roughness distribution and other attenuation mechanisms). Some of these surface parameters are difficult to estimate. However, the wavelength of the groundroll at high frequencies is small due to the near surface velocity profile; therefore the reflection energy is usually separated from the groundroll in the

frequency domain mostly by surface scattering, and imaging inside the groundroll window is feasible and theoretically justified.
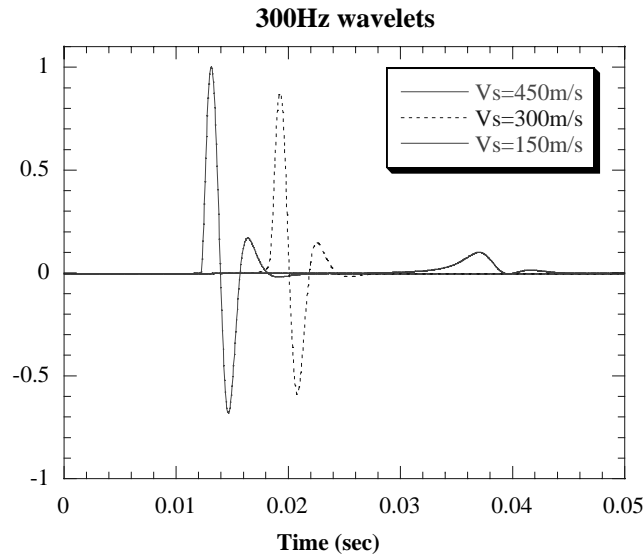
300Hz wavelets

Figure 7: 300Hz waveforms propagating 5m distance in the three different media in
Fig 5. Note that the low velocity wavelet is completely attenuated and has lost
all of its high frequencies. Thus, a good separation in the frequency domain is
expected for materials with such low velocities, e.g., unconsolidated sediments.

6.8   ACKNOWLEDGEMENTS

6.9 REFERENCES

Aki, K. and Richards, P. G., 1980, Quantitative Seismology: Theory and Methods, W. H. Freeman and Company, 932pp.

Bachrach, R. Dvorkin, J. and Nur, A. 1998, High resolution shallow seismic experiments in sand: 2). Velocities in shallow unconsolidated sands, Geophysics, In press.

Bachrach, R., Dvorkin, J. and Nur, A., 1998, Elasticity of shallow, unconsolidated sediments, In preparation.

Bachrach, R., Dvorkin, J. and Nur, A., 1997, Shear wave velocities in unconsolidated sand, SRB annual Report,.**63**.

Born, M., and Wolf, E, 1986, Principles of optics : electromagnetic theory of propagation, interference and diffraction of light, 6th ed., Pergamon Press, New York.

Dobrin, M., B, and Savit, C. H, 1988, introduction to Geophysical prospecting, McGraw-Hill Book Co., New York.

Hunter, J. A., Pullan, S. E., Burns, R. A., Gagne, R. and Good, R., 1984, Shallow reflection mapping of the overburden bedrock interface with engineering seismograph- Some simple techniques, Geophysics, 49, 1381-1385.

Maradudin, A. A., and Mills, D. L., 1976, The attenuation of Rayleigh surface waves by surface roughness, Annals of Physics, 1000, 262-309.

Nur, A., Mavko, G., Dvorkin, J and Gal, D., 1995, Critical porosity; the key to relating physical properties to porosity in rocks, SEG Annual Meeting Expanded Technical Program Abstracts with Biographies ; **65**, 878-881.

Steepls, D., W., Green, A.,G., McEvilly, T.,V., Miller, R. D., Doll, W. E. and Rector, J. W, 1997, A workshop examination of shallow seismic reflection surveying, The Leading Edge, 16, 1641-1647.

White, J. E.,1983, Underground sound: application of seismic waves: Methods in Geochemistry and Geophysics ; **18,** 253p.

APPENDIX

THE ATTENUATION OF RAYLIEGH SURFACE WAVES BY A ROUGH SURFACE:

In this appendix I review the main steps in the analytic solution obtained by A. A. Maradudin and D. L. Mills, (1976), for the attenuation of Rayliegh surface waves due to surface roughness. The complete solution is presented in their paper, here I review only the main steps in the derivation of the attenuation coefficient.

A. Problem formulation: The scattering of rayliegh waves by surface roughness.
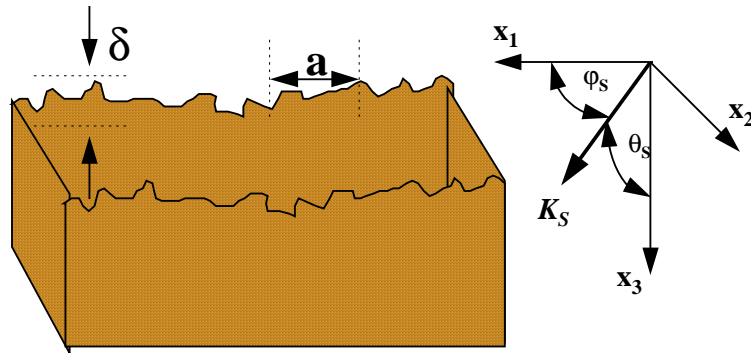
Figure 8: The geometry of a rough semi infinite solid. δ is the RMS amplitude of the surface, a is the correlation length. K_S is the scattering vector. See text for details.

Consider elastic half-space, with surface parallel to the x_1, x_2 plane, and is occupying $x_3 > 0$. The surface of the medium is rough, and the height of a point on the surface above the x_1, x_2 plane is given by the relation $x_3 = f(x_1, x_2)$. We assume that f has mean zero and mean square value which we will donate by $\delta^2 = < f(x_1, x_2)^2 >$.

Also assume that $f(x_1, x_2)$ is non zero only in a finite domain of dimensions L1 and L2. This is done for assuring finiteness of all the scattering cross-section which is consider.

The elastic moduli of a semi infinite elastic solid are position dependent, and are given explicitly by

$$C_{ijkl}(\underline{x}) = \theta\{x_3 - f(x_1, x_2)\}C_{ijkl} \tag{A.1}$$

where θ is the heviside step function and C_{ijkl} are the ordinary position independent elastic moduli of the linear elastic medium. This discussion is limited to isotropic elastic medium. In this case the elastic moduli is written in terms of the longitudinal velocity *Vp* and and transverse wave velocity *Vs*.

$$C_{ijkl} = \rho(V_p^2 - 2V_s^2)\delta_{ij}\delta_{kl} + \rho V_s^2(\delta_{ik}\delta_{jl} + \delta_{il}\delta_{kj})$$

The wave equation of elastic solid with position dependent elastic moduli is:

$$\rho\frac{\partial u_i}{\partial t^2} = \sum_{jkl}\frac{\partial C_{ijkl}}{\partial x_j}\frac{\partial u_k}{\partial x_l} + \sum_{jkl}C_{ijkl}\frac{\partial u_k}{\partial x_l x_j} \tag{A.2}$$

Where $u_i(\mathbf{x},t)$ is the i'th-Cartesian component of the elastic displacement field at point **x** and time t.

Now assume that the amplitude of the surface roughness is small, and expand the elastic moduli to first order around $f(x_1, x_2)=0$

$$C_{ijkl} \approx \theta(x_3)C_{ijkl} - f(x_1, x_2)\delta(x_3)C_{ijkl} + ... = C^{(0)}{}_{ijkl}(\underline{x}) + C^{(1)}{}_{ijkl}(\underline{x}) + ... \tag{A.3}$$

When substituting eq. (3) in eq. (2) we can rewrite eq. (2) in the form of:

$$\sum_j L^{(0)}{}_{ik}u_k(\underline{x},t) = -\sum_j L^{(1)}{}_{ik}u_k(\underline{x},t) \tag{A.4}$$

Where $L^{(0)}$ and $L^{(1)}$ are deferential operator matrix which its element are given by:

$$L^{(0)}_{ik}(\underline{x},t) = -\delta_{ij}\frac{\partial}{\partial t^2} + \frac{1}{\rho}\sum_{kl}\frac{\partial C^{(0)}_{ijkl}}{\partial x_j}\frac{\partial}{\partial x_l} + \frac{1}{\rho}\sum_{jkl}C^{(0)}_{ijkl}\frac{\partial^2}{\partial x_l x_j}$$

$$L^{(1)}_{ik}(\underline{x},t) = \frac{1}{\rho}\sum_{kl}\frac{\partial C^{(1)}_{ijkl}}{\partial x_j}\frac{\partial}{\partial x_l} + \frac{1}{\rho}\sum_{jkl}C^{(1)}_{ijkl}\frac{\partial^2}{\partial x_l x_j}$$

To solve equation (4), Green's function D_{kl} (**x,x'**;t-t') is introduce defined as the solution to equation:

$$\sum_k L^{(0)}_{ik}(\underline{x},t)D_{kl}(\underline{x},\underline{x'};t-t') = \delta_{ij}\delta(\underline{x}-\underline{x'})\delta(t-t') \qquad (A.5)$$

With decaying wave conditions at x3→∞.

We can write the equation of motion (A.4) in terms of this Green's function as an integral equation:

$$u_i(\underline{x},t) = u^{(0)}_i(\underline{x},t) - \sum_{kl}\int dx^3\int dt' D_{il}(\underline{x},\underline{x'};t-t')L^{(1)}_{ik}(\underline{x},t)u_k(\underline{x'}t') \qquad (A.6)$$

Where $u_i^{(0)}$ is the solution to the homogenous equation, and represent a Rayliegh surface wave propagating along the stress free surface defined as x_3=0.

$$\sum_k L^{(0)}_{ik}(\underline{x},t)u^{(0)}_k(\underline{x},t) = 0 \qquad (A.7)$$

Since the integral term in equation (6) is already first order in $f(x_1, x_2)$, we can use the first Born[1] approximation to give the scattered displacement field to the first order.

---

[1] Born Approximation assumes that the displacement field can be expressed as an infinite series of fields, where the nth member of the series represent the nth order back-scatteres field. See for

$$u_i^{(s)}(\underline{x},t) = u_i(\underline{x},t) - u_i^{(0)}(\underline{x},t) = -\sum_{k,l}\int dx_3' \int dt D_{il}(\underline{x},\underline{x}',t-t')L_{ik}^{(1)}(\underline{x},t)u^{(0)}{}_k(\underline{x}',t')$$

(A-8)

Assume now, with no loss of generality that the incident Rayliegh wave propagate in the positive x_1 direction. Then it can be shown[1] that the solution for equation (A-7) with free surface boundary conditions is the surface wave represented by the following equation:

$$u_1^{(0)}(k_{\parallel}^{(0)},\omega|x_3) = A(e^{-\beta_p x_3} - (1-\frac{V_R^2}{2V_s^2})e^{-\beta_s x_3})$$

$$u_3^{(0)}(k_{\parallel}^{(0)},\omega|x_3) = i(1-\frac{V_R^2}{2V_p^2})A[e^{-\beta_p x_3} - \frac{e^{-\beta_s x_3}}{(1-\frac{V_R^2}{2V_s^2})}]$$

(A.9)

where

$$\beta_p = k^{(0)}(1-\frac{V_R^2}{V_p^2})^{\frac{1}{2}}, \quad \beta_s = k^{(0)}(1-\frac{V_R^2}{V_s^2})^{\frac{1}{2}}, \quad k^{(0)} = \frac{\omega}{V_R},$$

$$u_i^{(0)}(\underline{x},t) = u_i^{(0)}(k_{\parallel}^{(0)},\omega|x_3)e^{ik_{\parallel}^{(0)}\cdot\underline{x}_{\parallel}-i\omega t}$$

and V_R is the Rayliegh wave velocity, given by the solution to the equation

$$\left(2-\left(\frac{V_R}{V_s}\right)^2\right)^2 - \left(4-\left(\frac{V_R}{V_p}\right)^2\right)^{\frac{1}{2}}\left(1-\left(\frac{V_R}{V_p}\right)^2\right)^{\frac{1}{2}} = 0$$

(A.10)

B. Evaluation of the scattered wave field

The scattered field, as given by equation(A-8) is now needed to be evaluated. The analytical approximation of the scattered wave field using the method of stationary phases shows that the scattered wave is the sum of three contributions: (a), P- wave

---

example, Born and Wolf, *Priciples of Optics* for general discussion or Aki and Richards, *Quantitative Seismology*, for elastic theory consideration.

[1] The Solution for surface waves under these conditions was obtained by Lord Rayliegh.

displacement field $\underline{u}_P^{(s)}(\underline{x},t)$; (b), S- wave displacement field $\underline{u}_S^{(s)}(\underline{x},t)$; and (c),

a Rayliegh surface wave displacement field $\underline{u}_R^{(S)}(\underline{x},t)$. The explicit expressions for

each of these scattered field take the following asymptotic form:

$$\underline{u}_P^{(s)}(\underline{x},t) \sim \frac{\underline{x}}{|x|} \frac{A}{\pi} \frac{V_S^2 V_R^2}{V_P^4} \hat{f}(\underline{k}_{\parallel}^P - \underline{k}_{\parallel}^{(0)}) \frac{e^{i(\frac{\omega}{V_P})|x|-i\omega t}}{|x|} g^{(P)}(\theta_S,\varphi_S) \tag{A11}$$

$$\underline{u}_S^{(s)}(\underline{x},t) \sim \frac{A}{2\pi} \frac{\omega^2 V_R}{V_S^3} \hat{f}(\underline{k}_{\parallel}^S - \underline{k}_{\parallel}^{(0)}) \frac{e^{i(\frac{\omega}{V_S})|x|-i\omega t}}{|x|} g^{(P)}(\theta_S,\varphi_S)\{\hat{x}_1$$
$$[g_a^{(S)}(\theta_S,\varphi_S)\cos(\theta_S)\cos(\varphi_S) + g_b^{(S)}(\theta_S,\varphi_S)\cos(\theta_S)\sin(\varphi_S)] \tag{A12}$$
$$+ \hat{x}_2[g_a^{(S)}(\theta_S,\varphi_S)\sin(\theta_S)\cos(\varphi_S) - g_b^{(S)}(\theta_S,\varphi_S)\cos(\theta_S)\cos(\varphi_S)]$$
$$+ \hat{x}_3[-g_a^{(S)}(\theta_S,\varphi_S)\sin(\theta_S)]\}$$

$$\underline{u}_R^{(S)}(\underline{x},t) \sim -A \frac{e^{-i\frac{\pi}{4}}}{i\sqrt{2\pi}} \frac{V_R^2}{2RV_S^2} (\frac{\omega}{V_R})^{\frac{5}{2}} \hat{f}(\underline{k}_R - \underline{k}_{\parallel}^{(0)}) \frac{e^{i\frac{\omega}{V_R}x_{\parallel}-i\omega t}}{\sqrt{x_{\parallel}}} \frac{[1-2\frac{V_S^2}{V_P^2}+\cos^2(\varphi_S)]}{[1-\frac{V_R^2}{2V_S^2}][1-\frac{V_R^2}{V_P^2}]^{\frac{1}{2}}}\{\hat{x}_1$$

$$[\cos(\varphi_S)][e^{-\beta_P x_3} - (1-\frac{V_R^2}{2V_S^2})e^{-\beta_S x_3}] + \hat{x}_2[\sin(\varphi_S)[e^{-\beta_P x_3} - (1-\frac{V_R^2}{2V_S^2})e^{-\beta_S x_3}] +$$

$$\hat{x}_3 i(1-\frac{V_R^2}{V_P^2})^{\frac{1}{2}}[e^{-\beta_P x_3} - e^{-\beta_S x_3} / (1-\frac{V_R^2}{2V_S^2})]\}$$

$$\tag{A13}$$

where

$$g^{(P)}(\theta_S,\varphi_S) = \frac{\cos\theta_S \sin^2\theta_S (1-\frac{V_S^2}{V_P^2}\sin^2\theta_S)^{\frac{1}{2}}(1-2\frac{V_S^2}{V_P^2}+\cos^2\theta_S)}{(1-\frac{V_S^2}{V_P^2}\sin^2\theta_S)^2 + 4\frac{V_S^3}{V_P^3}\cos\theta_S \sin^2\theta_S (1-\frac{V_S^2}{V_P^2}\sin^2\theta_S)^{\frac{1}{2}}}$$

$$g^{(S)}(\theta_S, \varphi_S) = \frac{\sin\theta_S \cos\theta_S (1 - 2\sin^2\theta_S)(1 - 2\dfrac{V_S^2}{V_P^2} + \cos^2\varphi_S)}{(1 - 2\sin^2\theta_S)^2 + 4i\cos\theta_S \sin^2\theta_S (\dfrac{V_S^2}{V_P^2} - \sin^2\theta_S)^{\frac{1}{2}}}, \qquad 0 < \sin\theta_S < \frac{V_S}{V_P}$$

$$= \frac{\sin\theta_S \cos\theta_S (1 - 2\sin^2\theta_S)(1 - 2\dfrac{V_S^2}{V_P^2} + \cos^2\varphi_S)}{(1 - 2\sin^2\theta_S)^2 + 4i\cos\theta_S \sin^2\theta_S (-\dfrac{V_S^2}{V_P^2} + \sin^2\theta_S)^{\frac{1}{2}}}, \qquad \frac{V_S}{V_P} < \sin\theta_S < 1$$

$$g_b^{(S)}(\theta_S, \varphi_S) = \tan\theta_S \cos\varphi_S \sin\varphi_S$$

C. The attenuation length of Rayliegh waves due to surface roughness.

With explicit expressions for all the components of the scattered displacement field, we can now calculate the rate at which energy is removed from the incident Rayliegh wave.

The time average of the energy in an elastic wave crossing unit area in unit time is given by the real part of the elastic Poynting vector, $\underline{\zeta}^c$, which is given by

$$\zeta_i^c = -\frac{1}{2}\sum_{jkl} C_{ijkl} \frac{du_j}{dt} * \frac{\partial u_k}{\partial x_l} \tag{A14}$$

The total energy per unit time radiated by the Rayliegh wave as it passes through a rough patch of surface of area L1L2 is:

$$\frac{dE^T}{dt} = \frac{dE^l}{dt} + \frac{dE^t}{dt} + \frac{dE^R}{dt} \tag{A15}$$

where the superscripts l, t and R reefer to the part of the energy carried away by longitudinal waves, transverse waves and Rayliegh surface waves respectively. Maradudin and Mills show that the Poynting vector defined in the end of this appendix can be decomposed into $\underline{\zeta}^l, \underline{\zeta}^t, \underline{\zeta}^R$ respectively. The energy of the wave per unit time is then defined by integrating the pointing vector along θ_s and φ_s the volumetric element $x^2 \sin^2\theta_s d\theta_s d\varphi_s$.

$$\frac{dE^{\alpha}}{dt} = \int_0^{\pi/2} d\theta_s \, \sin\theta_s \int_0^{2\pi} d\theta_s \, \sin\theta_s \zeta^{\alpha} \tag{A16}$$

The estimation of the attenuation length of the Rayliegh waves can be preformed now. The total energy stored in the incident Rayliegh wave crosing a unit area normal to the x1 direction is $\dfrac{dE_0}{dt}$, and is proportional to L2. Now the attenuation length for the Rayliegh waves is defined as the ratio of the initial energy of the wave to the radiated energy of the wave which is:

$$\frac{dE^{T}}{dt} = \frac{L1}{\ell} \frac{dE_0}{dt} \tag{A17}$$

L1 is the distance traveled by the Rayliegh wave as it passes over the rough region of the surface. The ratio of $(dE_0/dt)/L1(dE^{T}/dt)$ is the energy loss per unit distance traveled by the Rayliegh wave, and can be also be interpreted as the mean free path of the Rayliegh wave. We can now express the length as:

$\dfrac{1}{\ell} = \dfrac{1}{\ell^{\ell}} + \dfrac{1}{\ell^{t}} + \dfrac{1}{\ell^{R}}$ were each of the superscript ℓ,t and R indicate the contribution of the attenuation length for the different wave type.

The above attenuation length can be solved for a Gaussian surface roughness of the form $f(k_{\parallel}) = \pi a^2 e^{-(a^2/4)k_{\parallel}^2}$, and it is shown that for this distribution of surface roughness the attenuation length is proportional to:

$$\beta = \alpha_0 f(a\omega/V_R) \tag{A18}$$

where

$$\alpha_0 = \frac{\delta^2 a^2 \omega^5}{\pi V_R^5}, \tag{A19}$$

$f(a\omega/V_R) \cong$

$$\frac{\pi^2}{R^2} \frac{V_R^4}{V_S^4} (1 - \frac{1}{2}\frac{V_R^2}{V_S^2})^{-2} (1 - \frac{V_R^2}{V_P^2})^{-1} \exp(-\frac{1}{2}\frac{a^2\omega^2}{V_R^2})$$

$$\times \left[(1 - \frac{V_S^2}{V_P^2})^2 I_0(\frac{1}{2}\frac{a^2\omega^2}{V_R^2}) - 2(1 - \frac{V_S^2}{V_P^2})\frac{V_R^2}{a^2\omega^2} I_1(\frac{1}{2}\frac{a^2\omega^2}{V_R^2}) + 3\frac{V_R^4}{a^4\omega^4} I_2(\frac{1}{2}\frac{a^2\omega^2}{V_R^2}) \right].$$

$$\tag{A20}$$

and in the limits

$$f(a\omega/V_R) \cong$$

$$\frac{\pi^2}{R^2}\frac{V_R^4}{V_S^4}(1-\frac{1}{2}\frac{V_R^2}{V_S^2})^{-2}(1-\frac{V_R^2}{V_P^2})^{-1}$$ (A21)

$$\times\left[(1-\frac{V_S^2}{V_P^2})(\frac{1}{2}-\frac{V_S^2}{V_P^2})\right]+\frac{1}{32}, \qquad \frac{a\omega}{V_R} << 1$$

$$\times\left[(1-\frac{V_S^2}{V_P^2})^2\frac{V_R}{\pi^{1/2}a\omega}\right], \qquad \frac{a\omega}{V_R} >> 1$$

V_P, V_S and V_R are the P, S and Rayleigh wave velocities in the sediment, respectively, I_i is the modified bessel function of the first kind, ω is the angular frequency and R is a constant given by:

$$R = \frac{1}{(1-\frac{V_R^2}{V_S^2})^5}\left[\frac{V_R^4}{V_S^4}(1+2\frac{V_S^2}{V_P^2})^5 - \frac{V_R^2}{V_S^2}(9-5\frac{V_S^2}{V_P^2})+8(1-\frac{V_S^2}{V_P^2})\right]$$ (A22)

D. Poynting Vector for an Elastic Solid:

Electrodynamic Review:

Poynting Theorem:

The work done on the charges by the electromagnetic force is equal to the decrease of energy stored in the field, less the energy which flowed out through the surface.

The *energy per unit time, per unit area,* transported by the fields is called the

Poynting Vector.

$$\frac{dW}{dt} = -\frac{d}{dt}\int_V \frac{1}{2}(\varepsilon_0 E^2 + \frac{1}{\mu_0}B^2)dv - \frac{1}{\mu_0}\oint_S (E\times B)\cdot da$$

$$\frac{dW}{dt} = -\frac{d}{dt}\int_V \frac{1}{2}(\varepsilon_0 E^2 + \frac{1}{\mu_0}B^2)dv - \frac{1}{\mu_0}\oint_S (E\times B)\cdot da$$ (A23)

$$\frac{dW}{dt} = -\frac{d}{dt}\int_V \frac{1}{2}(\varepsilon_0 E^2 + \frac{1}{\mu_0}B^2)dv - \frac{1}{\mu_0}\oint_S (E \times B)\cdot da$$

$S = \frac{1}{\mu_0}E \times B$ is the Poynting Vector

Differential Form:

$$\nabla \cdot S = -\frac{\bar{o}}{\bar{o}t}(U_{mech} + U_{EB})$$

note: very similar to conservation Equation:

$$\nabla \cdot J = -\frac{\bar{o}}{\bar{o}t}\rho$$

Elastic Solid:

$$U_{kin.} = T = \frac{1}{2}\rho\sum_i \dot{u}_i^2 \qquad U_{pot.} = V = \frac{1}{2}\sum_{ijkl} C_{ijkl}\varepsilon_{ij}\varepsilon_{kl} = \frac{1}{2}\sum_{ij}\sigma_{ij}\varepsilon_{ij}$$

$$U_{total} = T + V$$

$$\frac{\bar{o}}{\bar{o}t}(U_{total}) = \rho\sum_i \ddot{u}_i\dot{u}_i + \sum_{ij}\sigma_{ij}\dot{\varepsilon}_{ij}, \quad \dot{\varepsilon}_{ij} = \frac{\bar{o}\dot{u}_i}{\partial x_j}$$

use the identity: $\sigma_{ij}\frac{\partial \dot{u}_i}{\partial x_j} = \frac{\partial}{\partial x_j}(\sigma_{ij}\dot{u}_i) - \frac{\partial \sigma_{ij}}{\partial x_j}\dot{u}_i$ define $\varsigma_i = \sum_j \dot{u}_j\sigma_{ij}$

we get

$$\frac{\partial}{\partial t}(U_{total}) + \nabla \cdot \varsigma = \sum_i \{-\sum_j \frac{\partial \sigma_{ij}}{\partial x_j} + \rho\dot{u}_i\} = 0$$ Therefore the elastic equivalent for

Poynting Vector is ς. This quantity is : The *energy per unit time, per unit area,*

transported by the Elastic field.

CHAPTER 7

**HIGH RESOLUTION WATER-TABLE IMAGING FOR SUBSURFACE
HYDROLOGICAL CHARACTERIZATION: INTEGRATION OF SEISMIC
AND GROUND PENETRATING RADAR.**

7.1   INTRODUCTION

The ability to image the same subsurface with more than one geophysical methods reduces part of the uncertainty in the interpretation of most geophysical data. However, in most cases the scale difference of the various geophysical measurements is large; hence, the integration of more than one method is difficult.

Ground penetrating radar (GPR) and seismic reflection surveys are similar, in that both methods image the subsurface using reflected wave fields. However, the earth's response to electromagnetic waves can differ from the earth's response to the seismic waves. The ability to compare two such surveys, which image the subsurface with comparable wavelength, improves identification and verification of events in the subsurface image, and results in better understanding of the different attributes of the sediments.

Specifically, the saturation distribution in an unconfined aquifer is an attractive geophysical target.   In unconfined aquifers, the water table and the saturation distribution vary in space and time. Their distribution is governed by the physics of fluid flow in a porous medium. Understanding the physics enables us to relate GPR water table and saturation images to the seismic saturation and water table images. The different signatures of a fluid obtained using these two methods provide a better understanding the hydrological properties of the subsurface. In this paper we will demonstrate that the ability to image the spatial and temporal fluid distribution can serve as an important tool for hydrological site characterization. We first present the theoretical basis for relating electromagnetic and seismic velocities to pore fluids and saturation. Next, we present a study which uses same wave-length GPR and seismic images, with subsurface resolution of about 10cm. We show the heterogeneity in a static watertable and relate it to grain-size distribution. Finally we present a method for combining seismic/GPR images with flow simulations for the estimation of spatially variable permeability field.

7.2   WATER TABLE: SEISMIC AND GPR RESPONSES

7.2.1   Velocity-Saturation Transformation

Seismic velocity

The compressional seismic velocity is a function of the elastic constants of a solid, and is expressed by the following equation:

$$V_p = \sqrt{\frac{\overline{K} + \frac{4}{3}\overline{G}}{\rho}}, \tag{1}$$

where $\overline{K}$ and $\overline{G}$ are the effective material bulk and shear moduli, respectively, and ρ is the density. Theory, laboratory data, and field data (Gassmann, 1951, Biot, 1962, Nur and Simmons, 1969; Murphy, 1984, Bachrach and Nur, 1998) have shown that the relation between velocity and saturation for seismic frequencies can be given by Gassmann's (1951) equation:

$$\frac{K_{sat}}{K_0 - K_{sat}} = \frac{K_{dry}}{K_0 - K_{dry}} + \frac{K_{fl}}{\phi(K_0 - K_{fl})}, \qquad G_{sat} = G_{dry}, \tag{2}$$

where ϕ is the porosity, G_{dry} and K_{dry} are the dry material shear and bulk modulus, K_0 is the mineral bulk moduli, K_{fl} is the pore fluid bulk modulus, and G_{sat} and K_{sat} are the saturated effective bulk modulus. For partially saturated rocks at low frequencies, one can express the effective modulus of the pore fluid as an iso-stress average of the air bulk modulus K_{gas} and the water bulk modulus K_w:

$$\frac{1}{K_{fl}} = \frac{S_w}{K_w} + \frac{1 - S_w}{K_{gas}}, \tag{3}$$

where S_w is liquid saturation of the pore space.

The density of the material is:

$$\rho = \phi\left(S_w \rho_{liquid} + (1 - S)\rho_{gas}\right) + (1 - \phi)\rho_0, \tag{4}$$

where ρ_{gas} and ρ_{liquid} are the gas and the liquid densities, and ρ_0 is the density of the mineral. These relations provides the basis for mapping seismic velocity into saturation, given the dry properties of the formation (Figure 1).

Velocity Saturation relations (Gassman)
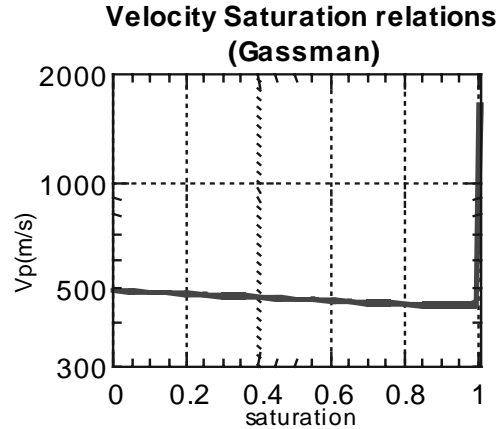
Figure 1:   Vp as a function of saturation for sand with porosity of 38% and dry velocity of 500m/sec. Note that the velocity decreases at partial saturation and increases only at full saturation.

Electromagnetic Velocities and Dielectric Constant

The electromagnetic (EM) velocity V_{GPR} can be expressed as a function of the cyclic-frequency ω, conductivity σ, dielectric constant ε, and magnetic permeability μ as follows:

$$V_{GPR} = \sqrt{\frac{2}{\mu\varepsilon}} \left[\sqrt{1+(\frac{\sigma}{\varepsilon\omega})^2} +1 \right]^{-\frac{1}{2}}. \tag{5}$$

The dielectric constant is defined as C_0/C, where C_0 is the velocity of light in vacuum and C is the velocity in the medium.

EM wave will propagate in conductive medium if ($\sigma<<\omega\varepsilon$).[1] In this region, $V_{GPR} \propto 1/\sqrt{\mu\varepsilon}$. Since the magnetic permeability is nearly constant in most materials the velocity change with saturation will be due to changes in the dielectric constant.

---

[1] This is a basic resolt from classical electromagnetic theory where we assume Maxwell's equation are these who governs the EM propagation. Most introduction to electrodynamics text books discuss in details these assumptions. (e.g. Grifiths, 1989).

The dielectric constant of water is 80, and the dielectric constant of most dry sediments is between 3 and 6.

If we wish to predict theoretically the effective dielectric permittivity of multi-phase material, the best upper and lower bound (of two phase materials) are the Hashin Shtrikman bounds (Hashin, Z. and Shtrikman, S., 1962):

$$\varepsilon^{\pm} = \varepsilon_1 + \frac{f_2}{\left(\varepsilon_2 - \varepsilon_1\right)^{-1} + \dfrac{f_1}{3\varepsilon_1}}, \tag{6}$$

where ε_1, ε_2 are the dielectric permittivity of the individual phases, and f_2, f_1 are the volume fractions of the individual phases. These bounds constrain any isotropic distribution of water and sediment.[1] Any path which will not violate these bounds is physically feasible.

Topp et al. (1980) showed that at sufficiently high frequencies the dielectric constant of sands and soils depends mostly on their volumetric water content. This dependence was expressed by the following empirical regression:

$$\theta = -5.3 \times 10^{-2} + 2.92 \times 10^{-2} \varepsilon - 5.5 \times 10^{-4} \varepsilon^2 + 4.3 \times 10^{-6} \varepsilon^3, \tag{7}$$

where θ is the volumetric water content and ε is the dielectric constant of the material. This equation is accurate to within a few percent, and is routinely used for water content measurement by time domain reflectometry (TDR) (Figure 2). Note that this relation is physically sound in the sense that it does not violate the Hashin-Shtrickman bounds for materials with dry dielectric constants of about 3.7. Thus, I will use Topp's regression as a unique transformation between the dielectric constant and the saturation. Note that the uniqueness of this transformation is always subject to adjustment and verification.

---

[1] We assume here that the sediment is an individual phase and is being mixed with water volumetrically, and we ignore the effect of an air and sediment mixture. Hashin-Shtrikman bounds can be expanded to account for more than two phases in a mixture (e.g. Berryman, 1995). Since air has a dielectric constant of 1, the sediment 4–6 and water 80, the representation of the system as two-phase system introduces very small error.
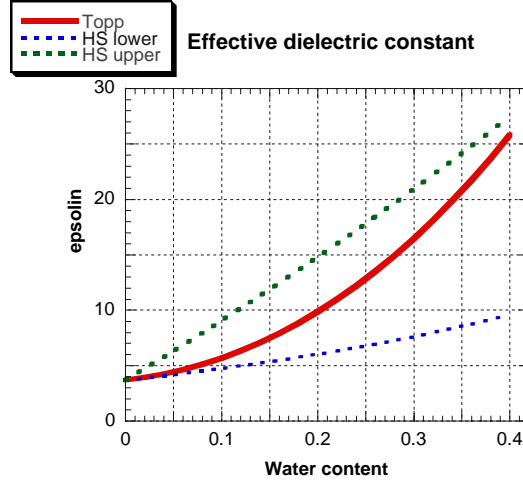
Figure 2: Dielectric Constant as a function of saturation as predicted by Topp's regression. Note that the relation does not violate the Hashin-Shtrickman bounds.

7.2.2 Hydrological Properties of an Unconfined Aquifer.

The equation that governs the distribution and flow of water in an unconfined aquifer can be written as follows:

$$\nabla(K(\underline{x},\psi)\nabla h) = \frac{\partial \theta}{\partial t}, \tag{8}$$

where θ is the volumetric water content, $K(\underline{x},\psi)$ is the hydraulic conductivity, ψ is the pressure head $h = \psi + z$ is the total head, and z is the elevation. The relation between the saturation and the pressure head can be approximated by different functional relations (e.g. Gardner, 1970; Van Gnuchten, 1978). The relations of Brooks and Corey (1964) are particularly convenient for this study:

$$\text{for } \psi \leq \psi_a \qquad S_{eff} = \frac{\theta - \theta_r}{\phi - \theta_r} = \left(\frac{\psi_a}{\psi}\right)^{\lambda}, \quad K_r = \left(\frac{\psi_a}{\psi}\right)^{\eta} \tag{9}$$

$$\text{for } \psi \geq \psi_a \qquad S_{eff} = 1, \qquad\qquad K_r = 1,$$

where S_{eff} is the effective water saturation, θ_r is the residual water saturation (after drainage), ψ_a is the air entry value, λ and η are empirical parameters, K_r is the relative hydraulic conductivity K_{sat} is the saturated hydraulic conductivity and $K(\psi) = K_{sat}K_r(\psi)$. Figure 3 presents the distribution of saturation as a function of ψ. We note here that in order to fully characterize the unsaturated flow properties we need *six parameters*: $K_{sat}, \lambda, \eta, \psi_a \theta_r$ and ϕ.
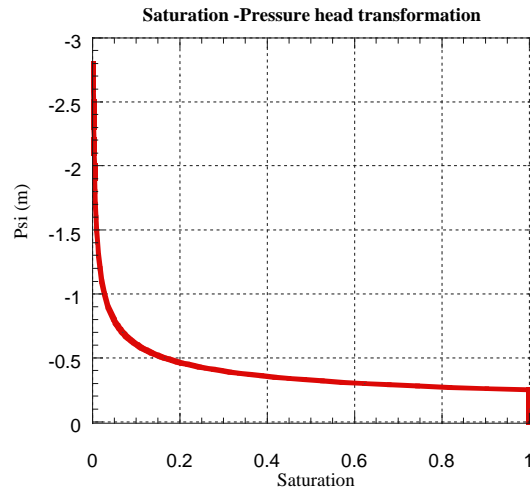
Figure 3: Effective saturation vs pressure head as defined by Brooks and Coorey's relations. In this example, λ is 2.6 , ψ_a is -0.25.

7.2.3 Water Table detection and Resolution Consideration

Equations (2),(4),(7) and (9) provide us the transformations from seismic/GPR space to the hydrological space which governs the fluid flow in porous medium. We will not address the uncertainty associated with these transformations, but we will address the resolution of the seismic/GPR survey.
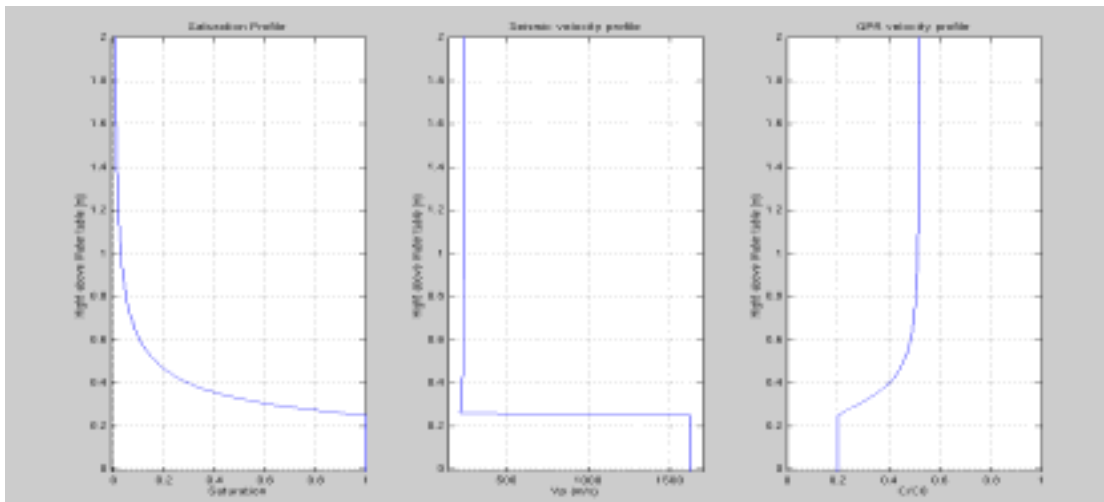
Figure 4: Saturation profile, seismic and GPR velocity for typical sand. The seismically defined water table in steady state is the top of the 100% saturated zone. The GPR velocity profile will decay gradually, and the location of the reflection and its width and strength will depend in general on the transition zone width. The saturation depth profile is grain-size dependent and can vary in space.

Figure 4 presents a saturation profile and the corresponding GPR and seismic velocity profiles. The seismic and GPR velocity responses of a partially saturated phreatic aquifer are different, but in principle they both will give us information about saturation. The GPR velocity can give us an estimate of the saturation without prior information. To get saturation from seismic velocity we will need prior information of the dry formation velocities. It is important to note that there is a difference between the way the water table is defined hydrologically, and the way it is detected geophysically. The hydrologic water table is defined by the equipotential surface (where the water pressure is equal to the atmospheric pressure), whereas the geophysical reflection from the water table will be somewhere in the transition between the partially saturated zone and the fully saturated zone. If we take, for example, the Brooks and Coorey relations between the saturation and the pressure head, the water table reflection will be always at ψ_a and not where $\psi = 0$. Since reflections arise from sharp discontinuities in the impedance (either acoustic or electromagnetic), it is clear that in an unconfined aquifer, as was pointed out by Annan et al (1991), the water table reflection will be better detected by the GPR when the transition width between the fully saturated and the under-saturated zone is small. When the transition zone is wide the monotonic-increasing relation between the dielectric constant and the saturation will cause a gradual velocity transition, smearing the water table reflection and making it difficult to resolve . In contrast, the seismic reflection from the water table should be sharp; the velocity decreases as the saturation increases (since the pore fluid compressibility does not change much at partial saturation, but the density does) and the pore fluid is stiff enough only at full saturation to cause a big velocity change. On the other hand, the saturation resolution will be better with GPR than seismic. The above discussion suggests that the combination of GPR and seismic will better serve the purpose of imaging saturated-unsaturated regions.

7.3   SAME-WAVELENGTH GPR AND SEISMIC EXPERIMENTS

I compare ultra-shallow seismic reflection images of depths less than 4m to shallow, 100MHz GPR sections, with approximately the same wavelength. As discussed in the previous section, the GPR and the seismic sections are not directly comparable since GPR reflective boundaries do not always coincide with the seismic boundaries. These images will demonstrate the potential for same-wavelength dual-method subsurface characterization, as will be discussed in the following sections.
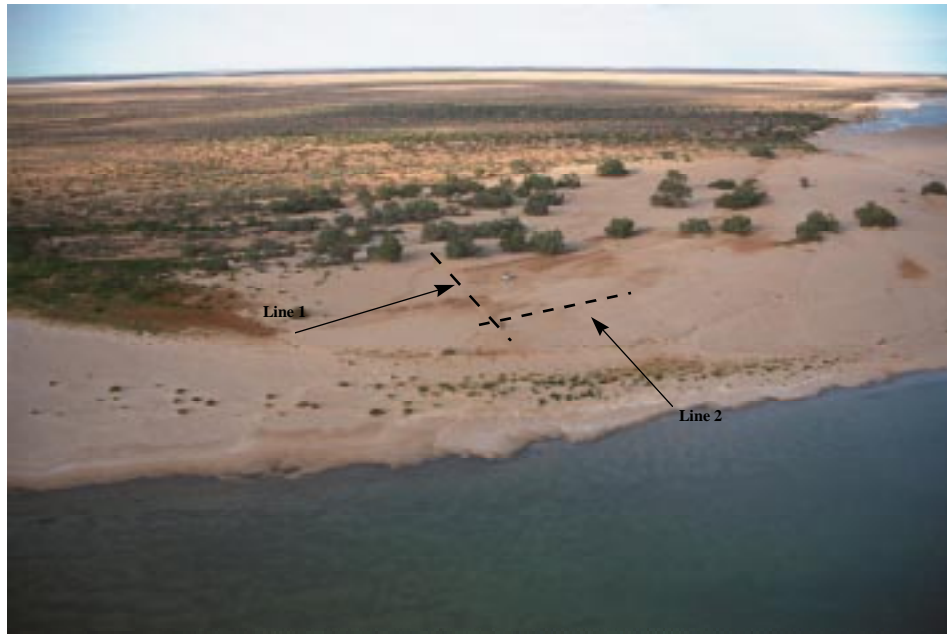
Figure 5: Point bar acquisition map. Line 1 is oriented normal to the river; Line 2 is parallel to the river bank.

7.3.1   Data Acquisition and Processing

Figure 5 shows a river point bar on which the data was acquired. The GPR and seismic sections we present are Line 1 and Line 2 and were collected perpendicular and parallel to the river, respectively. The water in the river is still and saline.

The GPR section was collected with 100MHz antennas which correspond to a wavelength of about 1m in dry sand, and shorter wavelengths in partially saturated sand. The seismic data were collected with a broad-band source, and processed to maintain central frequency of 300Hz, which corresponds to a wavelength of about 0.8m in a medium with velocity of 240m/s. In general, the wavelength scales with velocity, which is not constant. We ignore these variation (which are small), and define the GPR and seismic wavelength to be the same (within ±0.2m in the zone of interest). Our vertical resolution can be estimated by the quarter wavelength criterion (Yilmaz, 1987) and is 0.2m. Figure 6 presents raw shot gathers from the seismic experiment, where the prominent reflection at 36ms is the water table reflection. Note that the refraction from the water table at large offsets is at a very high velocity of about 1700m/s, which is a typical velocity for saturated sands. Thus the water table reflection is the one at about 30–36ms. The intersection of the two lines was augured, and the water table was found to be at depth of 3.35m. The top of the water

table reflection at the intersection is 31ms (figure 7), which corresponds to a depth of 3.41m. Thus we determined the depth of the water table with accuracy of about 6cm.

The source used was a small hammer. The acquisition system had 96 channels and the geophone spacing was 0.25m. We used a very simple data processing scheme for the reflection data which included first arrival mutes, filtering, NMO corrections, and stacking. The unmigrated stacked section is compared to the GPR unmigrated common-offset section. Both sections are displayed with AGC.

7.3.2   GPR-Seismic Comparison and Grain-Size Estimation

Figure 7 presents the four unmigrated time sections of the GPR and the seismic data. The GPR and the seismic sections are aligned to the same location within 1m (which is approximately the uncertainty in location during the GPR acquisition).

We first note that the GPR signal is strongly attenuated below the water table. This is due to the high salinity of the water which increases the electrical conductivity and thus causes energy losses and critical dumping. The seismic image continues below the water table. The signal-to-noise ratio in the GPR image is much higher than in the seismic image in both lines. This is due to the complexity of the ultra-shallow reflection acquisition, in comparison to the GPR. The dominant reflection in the seismic section is the water table.

We choose to compare 5 events from the two sections which are labeled (a), (b) and (c) in line 1, and (d) and (e) in line 2.
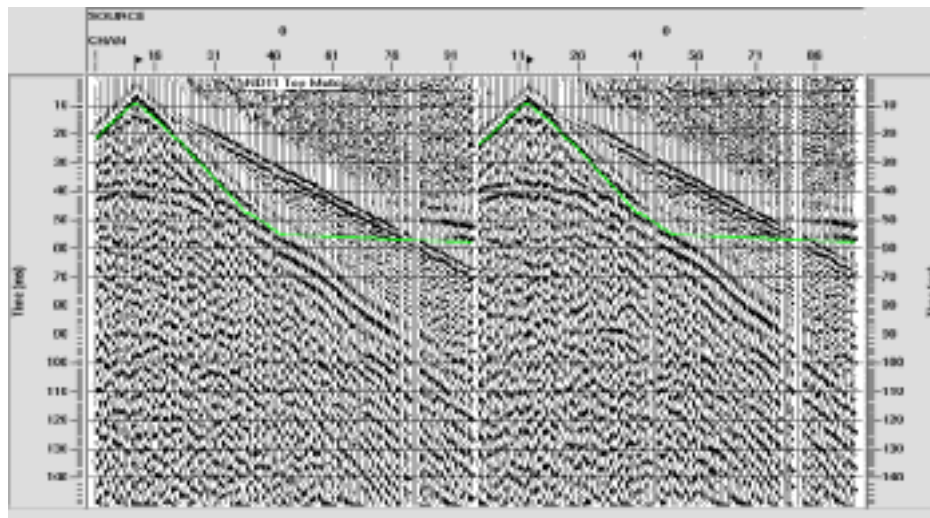

Figure 6: Raw shot gathers from line 1 with a 300Hz low-cut filter, AGC gain. The prominent reflection at 36ms is from the water table. Note a less coherent reflection at 12ms. There is 5ms delay in triggering . Refraction from the water table and the direct air wave are clearly seen.

Event (b) is a dipping layer reflection, which is visible in both sections. Note that in the time section, the dip of an event is not the true dip, but is velocity dependent. The diffraction pattern (a) in line 1 is totally attenuated in the GPR section. The diffraction pattern (c) is visible in both seismic and GPR sections. In line 2, we note that event (d), is attenuated in the seismic section.

While GPR images discontinuities in the dielectric properties of the subsurface, the seismic method images elastic boundaries, which are defined by density and velocity contrasts. Note that geologically, the sand bar is composed of different sand units which correspond to different flooding events. Each stratum within the bar is characterized by its own grain size-distribution and shape, which is a function of the depositional history (i.e. flow speed and distance from the origin). In general, the different mineralogy, size and sorting affects porosity and seismic velocity, as well as the dielectric constant. However, the effect is not the same; i.e., a GPR reflection does not necessarily correspond to a seismic reflection. This fact is most evident when considering the water-table reflection, as will be discussed later.

Event (e) in line 2 (Fig. 3), which is parallel to the river, shows a drop in the water-table reflection surface of 6.5 ms in two-way travel-time (TWT), which is about 0.7m in depth. This drop is present both in the seismic and the GPR images. Note that while the GPR reflection shows a gradual decline in the water table depth, the seismic image shows a sharp discontinuity. This sharp discontinuity can only be explained as grain-size spatial boundary, which causes the threshold pressure ψ_a to be different parallel to the river . A drop of 0.7m in ψ_a can be used to estimate the effective grain diameter using Laplace equation for capillary tubes (Bear, 1972):

$$p_c = \frac{\sigma_w}{r^*}\cos\theta \tag{10}$$

where here $p_c = \rho_w g \psi_a$ σ_w and ρ_w are the water surface-tension and density respectively, and r^* is the effective grain diameter. Given an estimated capillary-rise of 30±10 cm in the coarse sand, we can estimate that the ratio of effective grain diameter between the different sides of the sand bar is between 2.75 to 4.5.

It is clear from the GPR and seismic sections that the water table is not a regular, continuous surface. The water table surface appears to be very complex both seismically and in GPR. Note that the GPR water-table reflection does not correspond spatially to the seismic water table reflection. It would be difficult to separate the apparent complexity of the water table from the complexity of the

medium above it using either the GPR or the seismic separately. No static[1] effects would show up on both seismic and GPR in the same way. However, from both the seismic and GPR images we can analyze the water table reflection and characterize the different units which causes this complexity.

7.3.3   Summary

The following conclusions can be drawn from the joint analyses of the GPR and seismic sections:

- Same-scale GPR and seismic section are feasible
- GPR and the seismic techniques produce different images of the same environment.
- Water table is an attractive target for joint imaging, since the physical behavior of the reflection is well understood. Thus in principle, by combining the two techniques, we can better characterize heterogeneous subsurface units.
- Given hydrological understanding of the subsurface, we can estimate grain size distribution from the water table image.

---

[1] Static is a term in reflection seismology used for defining the deviation of a reflector from flatness. Due to near surface velocity changes, flat reflectors appear complex, and there are many ways to compensate for this deviation.
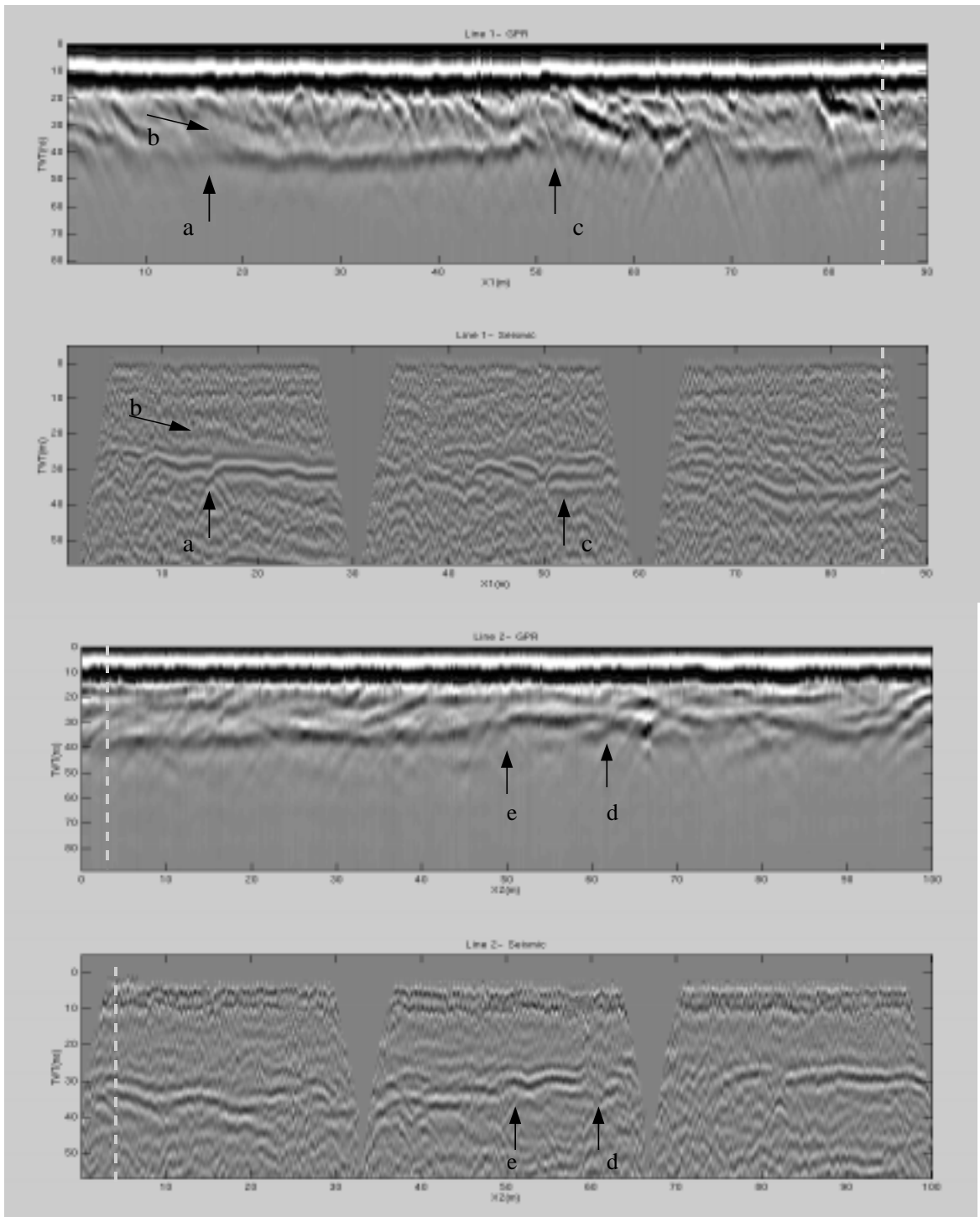
Figure 7: Comparison between the GPR and the seismic section for line 1 and 2. The events a,b,c,d and e are approximately the same event as appears on the seismic and GPR section. Refer to the text for more details. The dashed line is the intersection of the two section, as shown in figure 5.

7.4 IMAGING TRANSIENT WATER TABLE DURING PUMPING TEST

We showed that elastic and electromagnetic wave velocities in porous media are sensitive to the presence of fluids in the pore space. Consequently, monitoring velocity changes in porous systems can serve to image time variations of saturation in the subsurface, and to extract hydraulic transport properties. To investigate the feasibility of monitoring, we model the response of an unconfined aquifer to shallow seismic and GPR surveys during pumping. We use a 3D radial flow model to compute partial saturation profiles in a heterogeneous, unconfined aquifer at different times of the pumping. We then compute the corresponding, time-varying seismic and GPR images of the subsurface for these saturation profiles. We use the theory to extract the seismic velocity field of the subsurface from the saturation. The electromagnetic response of the subsurface is computed using an empirical regression between the saturation and the dielectric constant of the medium. This method is widely supported by laboratory and field observations. The simulated results show that velocity analysis of both the seismic and the GPR sections can be used for estimating the saturation variations in an unconfined aquifer during pumping tests; high-permeability zones result in sharper images of the water table with both GPR and seismic sections. Low-permeability zones are detectable because of the relatively high partial saturation values left behind by the down-drawn water table.

7.4.1 Site Characterization: Forward Modeling

To demonstrate the potential use of transient flow imaging in an unconfined aquifer, we combined flow simulation and forward modeling of the seismic and GPR response in a partially saturated aquifer during a pumping test. We generated a synthetic, heterogeneous aquifer with an initial water table depth of 2 meters, and we simulated the saturation distribution after 2.2 days of pumping. The grid and the permeability field used for the simulation are shown in figure 8. The well is located at radial distance R=0.

We used 3D radially-symmetric, variably-saturated flow simulation (VS2DT flow model, Healy, 1990) to calculate the saturation distribution, and from it the seismic velocity and dielectric constant map of the aquifer. We used a log-normal distribution of the saturated hydraulic conductivity and, for simplificity, assumed that the other hydraulic parameters were constant. The saturation distribution and the seismic and GPR velocities are presented in figure 9 (a),(b), and (c).

From figure 9, it is clear that the saturation is better resolved by the GPR. On the other hand, the water table location is better resolved by seismics. We also note that the discretization of the flow domain was done with a vertical cell dimension of 20cm, which is a conservative estimate of our vertical resolution for high-resolution GPR and seismic surveys. Figure 11 shows synthetic, normal-incident, zero-offset seismic and GPR sections of the velocity field presented in figure 10. The GPR velocity in the saturated zone is lower than in the unsaturated zone, whereas the seismic velocity is lower in the unsaturated zone. This causes the scale difference in these time sections. Overall, the seismic reflection is much sharper than the GPR water-table reflection, as expected and observed in the field.

7.4.2   Permeability Estimation using Geophysical Data: Biased Estimation

A common practice in hydrology is to identify the conductivity field from the hydraulic head measurement. Information about the pressure head is usually obtained from point measurements such as piezometers and monitoring wells. Furthermore, the permeability field is estimated to be a constant effective permeability. Obtaining such an estimate from head measurements in unconfined aquifer is described by Boulton, 1963, Neuman, 1972, and Menoch, 1995.

From Figures 5 and 6 it is clear that heterogeneity in the conductivity governs the lateral gradient of the water-table. The ability to continuously image the water table will provide us important information about the conductivity. Furthermore, the vertical saturation distribution is broader in low permeability zones, where the vertical drainage is slow than in high permeability zones. This information can be utilized for the qualitative identification of low and high permeability zones. To get a more quantitative estimate of conductivity values from our geophysically-based velocity-depth map, we must apply inversion techniques, as will be described next.
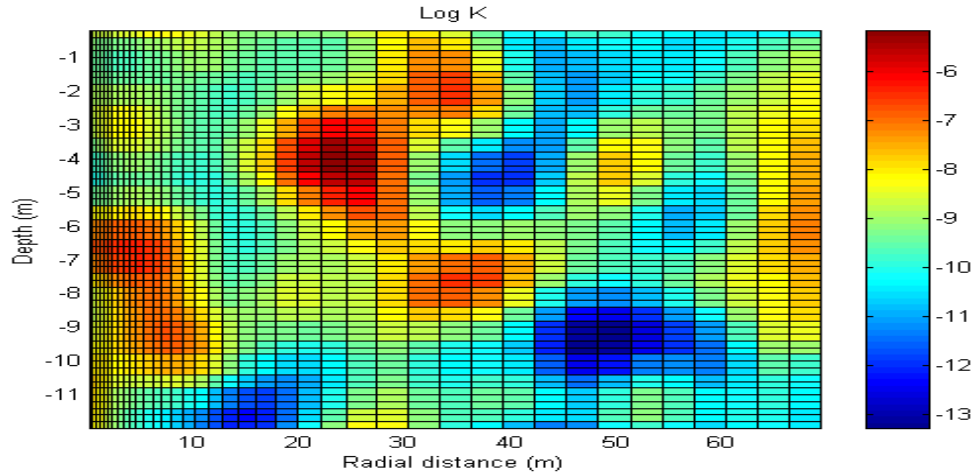
Figure 8: The hetrogenous conductivity distribution used for the simulation of pumping test in the unconfined aquifer.

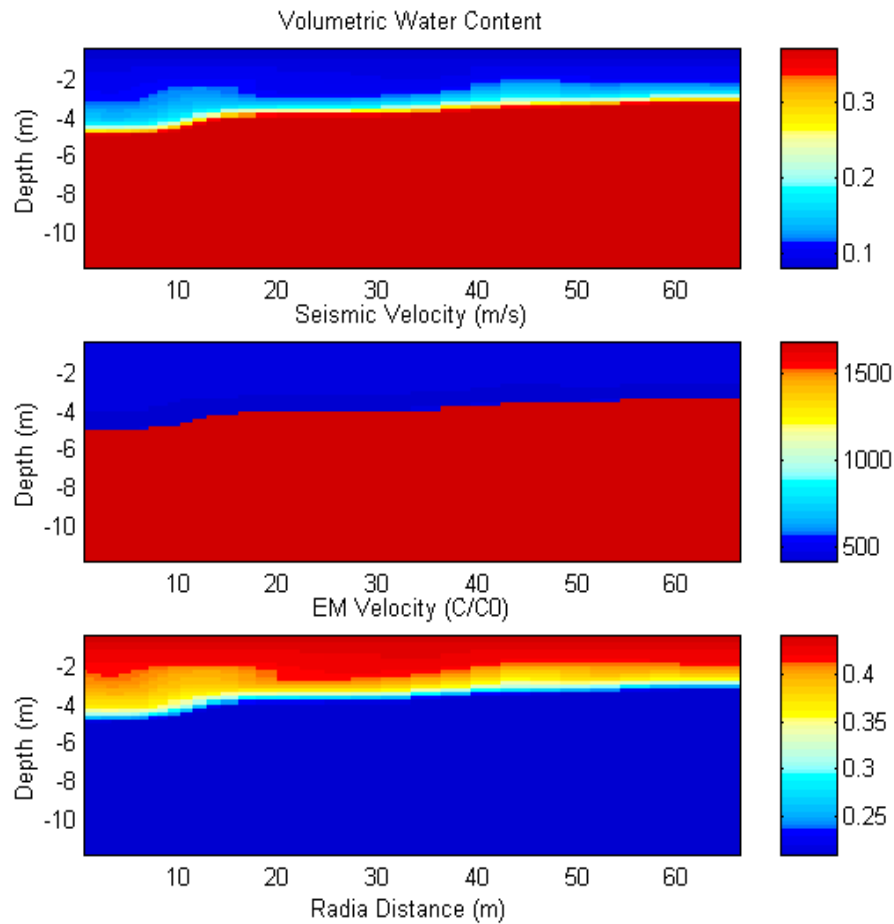Figure 9: Forward modeling of the geophysical response of an unconfined aquifer to pumping. Top- The volumetric water content distribution after 2.2 days of pumping. Middle- The seismic compressional velocity distribution as calculated from the saturation distribution by Gassmana's relations. Bottom- The EM velocity distribution as derived from Topp's relations (fraction of the speed of light in vacuum)
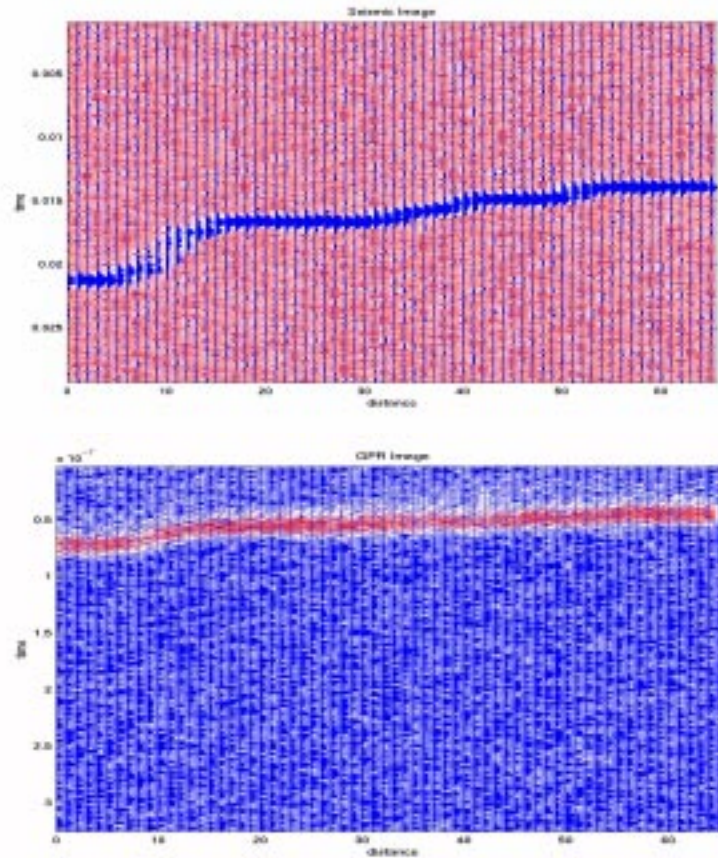
figure 10: Synthetic seismic and GPR zero-offset sections of the simulated velocity field in figure 9. Top 300Hz Seismic image, Bottom- 100MHz GPR image. Both synthetic section were generated with random noise.

Spatial Variability and Regularized Estimation

There are many possible inversion schemes. Our approach is to use the spatially continuos geophysical data, together with conventional pumping-test analysis, to identify heterogeneity in the subsurface. We do that by using the conventional analysis as *a priori* information toward which we will bias our solution.

Let the seismic location of the water table be our measurement vector, defined as $\underline{z}$. We model the measurement error vector $\underline{V}$ as a Gaussian random vector with zero mean and covaraince matrix R. We are looking for the log-permeability field $\underline{s}$ which will minimize the least-square error between measured water-table $\underline{z}$ and the estimated water table $h(\underline{s})$ derived from our numerical model. Even with spatially continuos geophysical measurements, this problem is under-determined, since the water-table measurements give only one dimension in a 2- or 3-dimensional problem. Thus, we need to regularize the problem. This can be done by using our effective

permeability estimate, which we obtained from the regular estimation of pumping test results (e.g. type curve matching for a Neuman-type solution). Thus, we are looking for a solution which will be biased toward a constant known value $\underline{\mu}$. $\underline{\mu}$ is also known as the Tikhanov regularization term (Meju, 1994). Q is a weighting function, which will determine how close the estimate will be to $\underline{\mu}$.

$$L = [\underline{z} - h(\underline{s})]^T R^{-1}[\underline{z} - h(\underline{s})] + [\underline{s} - \underline{\mu}]^T Q^{-1}[\underline{s} - \underline{\mu}]. \tag{11}$$

Note that minimizing L can be interpreted as the "maximum *a posteriori*" (MAP) of $\underline{s}$ (Kitanidis, 1995, 1997), where now Q is the model covariance function. This MAP is also biased toward $\underline{\mu}$. We prefer to treat Q as a weighting function, since we do not claim to know the spatial moments of $\underline{s}$; furthermore, we would suggest that this estimation procedure should be done interactively where Q can be changed to better fit the data or the effective mean.[1]

We linearize the problem by expanding $h(\underline{s})$ around the current estimate $\hat{\underline{s}}_i$

$$h(\underline{s}) \approx h(\hat{\underline{s}}_i) + H\Delta\underline{s} \tag{12}$$

$$H = \left.\frac{\partial h(\underline{s})}{\partial \underline{s}}\right|_{\underline{s}=\hat{\underline{s}}_i} \quad \text{and} \quad \underline{s} = \hat{\underline{s}}_i + \Delta\underline{s}.$$

Minimizing L with respect to $\underline{s}$ yields the following normal equation:

$$\frac{\partial L}{\partial \underline{s}} = 0 \Leftrightarrow -[\underline{y} - H\Delta\underline{s}]^T R^{-1} + [\hat{\underline{s}}_i + \Delta\underline{s} - \underline{\mu}]^T Q^{-1} = 0, \tag{13}$$

were $\underline{y} = \underline{z} - h(\hat{\underline{s}}_i)$

We now solve for $\Delta\underline{s}$ and obtain the solution:

$$\Delta\underline{s}^T = [\underline{y}^T R^{-1} H + (\hat{\underline{s}}_i - \underline{\mu})^T Q^{-1}][H^T R^{-1} H + Q^{-1}]^{-1}. \tag{14}$$

Finally, we deal with the non-linearity with using the iterative formula

$$\hat{\underline{s}}_{i+1} = \hat{\underline{s}}_i + \Delta\underline{s}. \tag{15}$$

---

[1] In non-uniform grid as in our case, Q is not a simple diagonal function. Since each grid-cell have its own spatial dimension, one must address the spatial continuity of $\underline{s}$ and to make sure that there is spatial-continuity between the small grid-cells. This continuity can be modeled by correlation length of the size of the larger grid-cell, or by any *a-priori* estimate.

Numerical procedure and Inversion Results

The grid we used was a 60x40 flow cell, which yields 2400 nonuniformly-spaced permeability cells. The Jacobian matrix H was calculated numerically using finite difference. The computation of the Jacobian matrix took about 5 hours on a new Sun workstation. There are other, more economical methods to calculate the sensativity matrix H (Yeh, 1986). However, given fact that we know already the mean $\underline{\mu}$, the number of iteration is not large. The non-linear nature of the problem makes finite difference a reasonable choice.

Figure 11 presents our inversion results as well as the true permeability. We can see that the heterogeneous conductivity field was recovered close to the well (~30 m lateral distance). This is because the drawdown is more significant closer to the well. The two main features of the aquifer (the high conductivity zone next to the pumping well and the low conductivity zone around it) are recovered adequately by the inversion. Figure 12 shows the initial residual $\underline{y} = \underline{z} - h(\underline{\mu})$ and $\underline{y} = \underline{z} - h(\underline{\hat{s}}_3)$ the residual after three iteration. Note that the estimated permeability field reproduce the observed water-table measurements within the error. The criterion for convergence in this case is getting the residual within the accuracy of the geophysical measurement (0.2m in this case). Note also that the Jacobian matrix H is biased, i.e. it will identify permeability field close to the pumping well than farther from it due to the radial symmetry of the 3D code and the pumping boundary conditions.
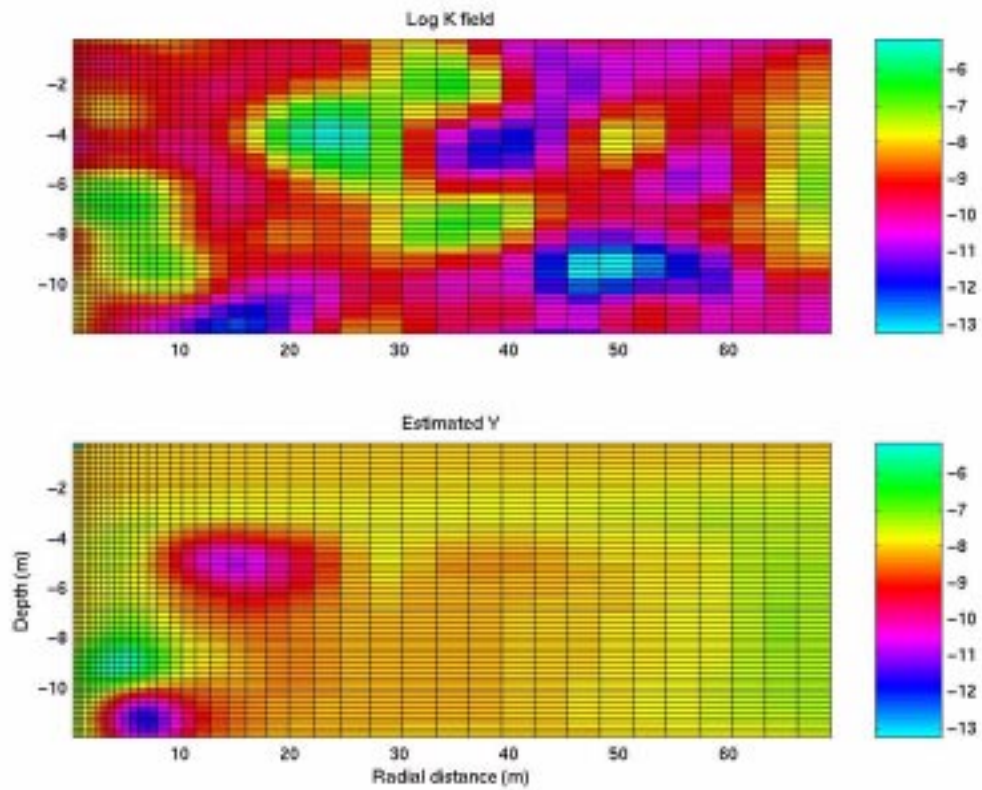
Figure 11: Inversion results using linearized biased inversion techniques. Top: True log conductivity field. Bottom: estimated log conductivity field.

Water-Table Residuals: Initial values

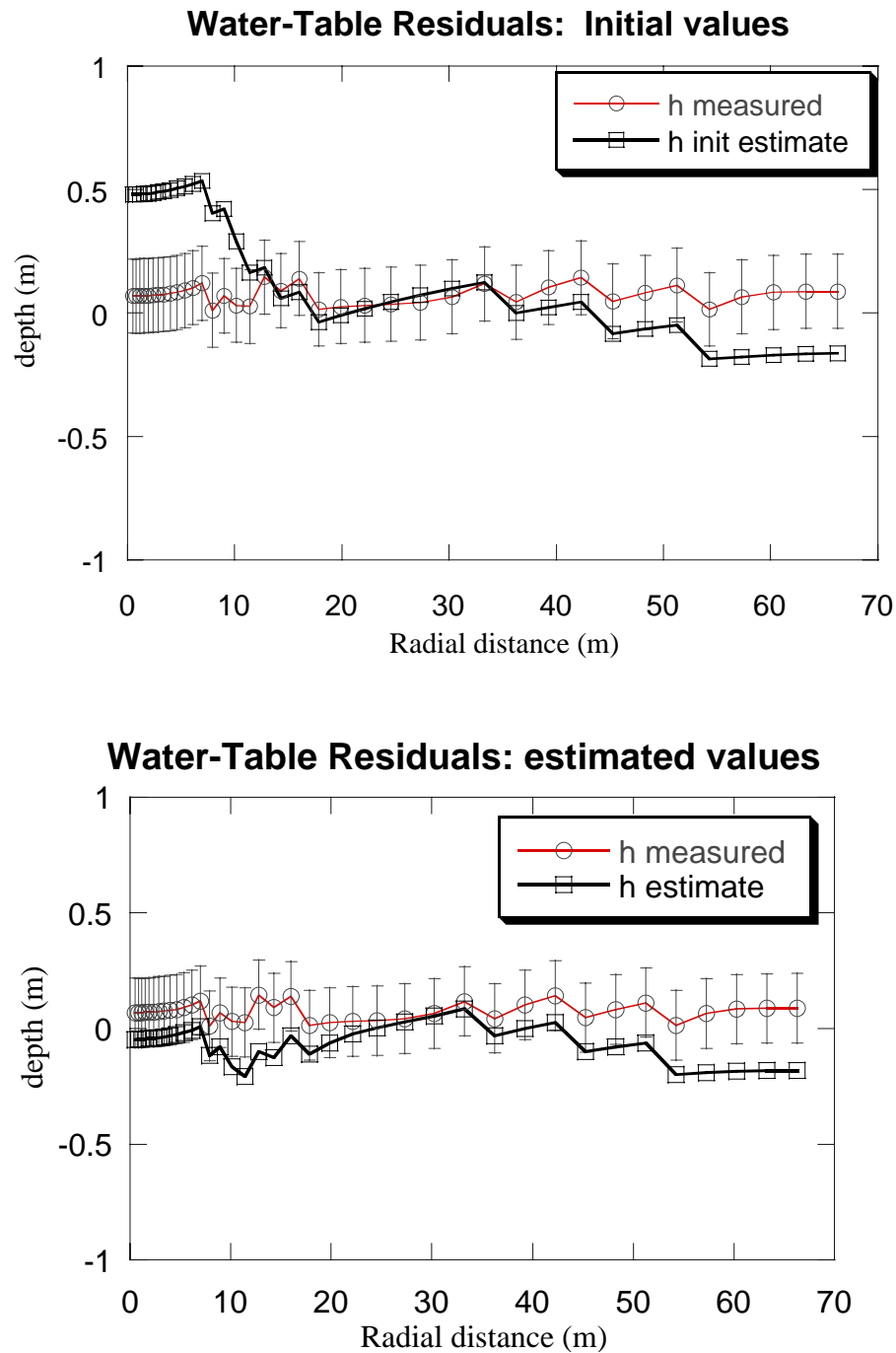## Water-Table Residuals: estimated values

Figure 12:   Initial and inverted residual.   The measurements are the difference between water table depth defined from seismic data and the flow simulation. Error bars present the uncertainty. Top: Constant permeability model. Bottom: Converged residuals (after three iterations), most measurements are within the error bar.

7.5   SUMMARY AND CONCLUSION

Seismic and GPR can monitor fluid flow in an unconfined aquifer by imaging the saturation distribution in space and time. The key for imaging saturation is the correct analysis of the relations between velocity and saturation. Since the responses of the GPR and the seismic methods to saturation variations are different, the combination of the two techniques will maximize information about the water table and the saturation distribution. The hydrological process must be accounted for when imaging saturation.

Once a saturation image (more specifically, water table image) is obtained, fluid flow simulation can be used to link the geophysical image to the hydraulic properties of the site. We show that incorporating the fluid flow and the seismic image can yield an estimate of the spatial conductivity field of the subsurface. Geophysical data is incorporated in the regular conductivity estimation by using the conventional estimate as prior information, then updating it using the geophysical data with its uncertainty. Resolution of 0.2m (which is poor in comparison to well data) with _continues_ spatial coverage can better determine the subsurface transport properties, and specifically locate the heterogeneity.

7.6   ACKNOWLEDGMENT

7.7   REFERENCES:

Annan, A. P., Cosway, S. W. & Redman, J. D., 1991, Water Table Detaction with Ground-Penetrating Radar, S.E.G extendent abstract, 494-496.

Bachrach, R., and Nur, A., 1998, High resolution shallow seismic experiments in sand: 1). Water table, Fluid flow and Saturation, Geophysics, **63**, 1225-1233.

Bear, J., 1972, Dynamic of fluids in porous media, American Elsevier Pub. Co., New York, 764 pp.

Berryman, J. G., 1995, Mixture theories for rock properties in: A handbook of physical constants, Thomaas J. Ahrens ed., American Geophysical Union, Washington, 236 pp.

Biot, M. A., 1962, Mechanicss of deformation and acoustic propagation in porous media, j. apll. Phys.**, 33**, 1482-1498.

Boulton, N. S., 1963, Analysis of data from non-equilibrium pumping tests allowing for delyed yield from storage: Proc. Ins. Of Civil Engineers, **26**, 469-482.

Brooks, R. H. and Corey, A. T., 1964, Hydraulic properties of porous media, Hydrology paper no. 3, Colorado State Univ., Ft. Collins, Colorado.

Gardner, W. R., 1970, Field measurements of soil water diffusivity, Soil Science Society of America Proc., **34**, 832.

Gassmann, F., 1951, Uber die elastizitat poroser median, Vier. der natur Gesellschaft, **96,** 1-23.

Griffiths, D. J., 1989, Introduction to electrodynamics, Prentice Hall, Englewood Cliff, New Jersy, 532 pp.

Hashin, Z. and Shtrikman, S., 1962, A variational approach to the theory of effective magnetic permeability of multiphase materials, J. of applied physics, 33, 3125-3131.

Healy, R. W., 1990, Simulation of solute transport in variabaly saturated porous media with supplemental information on modification to the usgs computer program vs2d, USGS open file report 90-4025.

Kitanidis, P. K, 1995, Quasi-linear geostatistical theory for inversing: Water resource reaserch, **31**, 2411-2419.

Kitanidis, P. K., 1997, The minimum structure solution to the inverse problem: Water resource reaserch, **33**, 2263-2272.

Meju, M. A., 1994, Biased estimation; a simple framework for inversion and uncertainty analysis with prior information: Geophysical Journal International, **119**, 521-528.

Moenech, S. P., 1995, Combining the Neuman and Boulton models for flow to a well in an unconfined aquifer: Ground Water, **33**, 378-384.

Murphy,W. F., III., 1984, Acoustic measures of partial gas saturation in tight sandstones. J.G.R, **89**, (13), 549-559.

Neuman, S. P., 1972, Theory of flow in unconfined aquifers considering delayed response of the water table: Water Resource Research, **8**, 1031-1044.

Nur, A. and Simmons, G., 1969, The effect of saturation on velocity in low porosity rocks, Earth Plan. Sci. Lett., **7**, 183-193.

Topp, G. C., Davis, J. L., and Annan, A.P., 1980, Electromagnetic determination of soil water content: Measurements in coaxial transmition lines, Water Resource Research, 16, p. 574-582.

Van Genuchten, R., 1978, Calculating the unsaturated hyraulic conductivity with a new closed form analytical model, Publication of the Water Resour. Prog. Dept. Civ. Eng., Princeton University, Princeton New Jersey.

Yeh, W. W-G, 1986., Review of parameter identification procedures in grounwater hydrology: The inverse problem, Water resour. Res., 22(1), 95-108.

Yilmaz, O., 1987, Seismic data processing, Society of Exploration Geophysics, Tulsa Oklahoma, 526 pp.